Engineering Journal

Third Quarter 2026 | Volume 63, No. 3

Smarter. Stronger. Steel.

Engineering Journal

American Institute of Steel Construction

Dedicated to the development and improvement of steel construction, through the interchange of ideas, experiences, and data.

 Engineering Journal (ISSN 0013-8029) is published quarterly. Published by the American Institute of Steel Construction at 130 E Randolph Street, Suite 2000, Chicago, IL 60601.

Design of Steel Headed Stud Anchors in Concrete-Filled Steel Composite Deck

ROBERT BAILEY BOND, SHUN LEI YEE, BENJAMIN W. SCHAFER, MATTHEW R. EATHERTON, W. SAMUEL EASTERLING, and JEROME F. HAJJAR

ABSTRACT

This paper reports common failure mechanisms of steel headed stud anchors (shear studs) in concrete-filled steel composite decks found in the literature comprised through an extensive database of push-out tests representing multiple shear stud configurations used in composite construction around the world. Monotonically and cyclically loaded push-out test specimens perpendicular or parallel steel deck, or in solid slabs, are included in the evaluation. Comparisons to experimental strengths are made with the steel headed stud anchor strength prediction methods from various international codes and standards along with other mechanics-based design provisions proposed in the literature. Results indicate that shear stud strength predictions for concrete failure modes are often overestimated, meaning the predicted shear stud strength is higher compared to the experimental shear stud strength based on push-out tests, especially for deck perpendicular configurations. To better address concrete-related failures, two alternative design equations are presented within the context of the AISC *Specification* framework and are validated through comparisons with both push-out tests and composite beam tests documented in the literature.

Keywords: composite construction, composite beam, composite diaphragm, steel headed stud anchor, shear connector, steel deck.

INTRODUCTION

Background

Concrete-filled steel composite decks are one of the most prevalent diaphragm assemblies used in building construction (Ahmed and Tsavdaridis, 2019). Composite action allows the assembly to act as one, thereby increasing the flexural stiffness of the entire deck system and allowing for a reduction in steel beam depth and weight. Steel headed stud anchors (shear studs) are the most widely used shear connectors to induce composite action between the steel members and concrete slab. A channeled steel deck, commonly oriented perpendicular or parallel to the span of the steel beam, is used as permanent formwork for the concrete-fill and stiffens the entire assembly with the steel headed stud anchors located in the troughs of the deck.

The push-out test, developed in Switzerland in the 1930s for spiral shear connectors (Davies, 1967), has become the prevailing method to estimate the shear strength of shear connectors. Steel headed stud anchors first appeared as shear connectors in the 1950s, initially studied without the influence of a steel deck (Ollgaard et al., 1971; Slutter and Driscoll, 1963; Viest, 1956). The total assemblage is weakened due to edge-like conditions introduced by a trapezoidal troughs when placed transverse to the span of the beam (Easterling et al., 1993). Several researchers have proposed strength reduction factors to account for this reduced strength (Fisher, 1970; Grant et al., 1977; Lawson, 1992; Mottram and Johnson, 1990). The 1978 AISC *Specification* (AISC, 1978) adopted the strength reduction factor of Grant et al. (1977), which has since been removed.

Baseline limitations to the composite assembly have been set through extensive testing in the literature. Work from Goble (1968) found that flange pull-out failure occurs when the diameter-to-flange thickness ratio is above 2.7. The 2022 AISC *Specification for Structural Steel Buildings* (2022b), hereafter referred to as the 2022 AISC *Specification*, proposes a ratio of 2.5, unless the steel headed stud anchor is located directly over the web of the beam. Slutter and Driscoll (1963) proposed that the total height-to-diameter ratio for shear studs embedded in normal-weight concrete should be equal to or larger than 4.2 to achieve full shear transfer. Fisher (1970) found smaller diameter studs to be more efficient shear connectors compared to larger diameter studs and recommended the stud diameter to be

Robert Bailey Bond, Department of Civil and Environmental Engineering, Northeastern University, Boston, Mass. Email: Bond.Rob@northeastern.edu

Shun Lei Yee, Department of Civil and Environmental Engineering, Northeastern University, Boston, Mass. Email: Yee.Sh@northeastern.edu

Benjamin W. Schafer, Department of Civil and Systems Engineering, Johns Hopkins University, Baltimore, Md. Email: Schafer@jhu.edu

Matthew R. Eatherton, Department of Civil and Environmental Engineering, Virginia Tech, Blacksburg, Va. Email: MEather@vt.edu

Samuel Easterling, College of Engineering, Iowa State University, Ames, Ia. Email: WSE@iastate.edu

Jerome F. Hajjar, Department of Civil and Environmental Engineering, Northeastern University, Boston, Mass. Email: JF.Hajjar@northeastern.edu (corresponding)

Paper No. 2024-10R

limited to 0.75 in. (19 mm) or less. The 2022 AISC *Specification* requires 0.75 in. (19 mm) or less diameter studs for slabs with steel deck ribs and 1 in. (25.4 mm) or less diameter studs for solid slabs. Fisher also concluded that the number of studs per rib does not increase the shear strength of the rib by the same proportion. Smith and Couchman (2010) found that the perpendicular spacing of the studs has little effect on the resistance and groups of more than two offer little additional strength. The 2022 AISC *Specification* applies an R_g factor to account for stud grouping and will be discussed in detail in the following sections. Ollgaard et al. (1971) observed a reduction in stud strength as the longitudinal stud spacing decreased and approached 6 times the stud diameter for studs in lightweight concrete slabs. The 2022 AISC *Specification* requires a minimum center-to-center stud spacing of 4 times the stud diameter in any direction. Additionally, Fisher (1970) noted a loss of strength in concrete-filled steel composite deck with lightweight (LW) concrete.

The majority of steel decks used today possess a stiffener that is located in the middle of the deck rib to increase the strength of the deck. Due to the geometric interference, studs must be welded on one side of the stiffener. The stud can be placed on either side that offers more or less concrete cover in the direction of loading, known as the strong and weak positions, respectively. Lawson (1992) was the first to account for stud position due to stiffeners with a strength reduction factor. Shear stud behavior is heavily dependent on their location in the deck rib (Easterling et al., 1993; Lyons et al., 1994; Sublett et al., 1992).

A small number of prior studies have been dedicated to investigating cyclic loading on steel headed stud anchors in composite deck construction (Pallarés and Hajjar, 2010; Zhai et al., 2018). The 2022 AISC *Seismic Provisions* (2022a) specify a 25% reduction to the 2022 AISC *Specification* stud strength equation with a limitation to 0.75 in. diameter studs. Recent research shows this reduction to be adequate and conservative (Pallarés and Hajjar, 2010).

Objectives

This work reevaluates the design procedures for the calculation of shear strength of steel headed stud anchors in concrete-filled steel composite deck, specifically addressing concrete-related failures. Although many researchers have studied the effects of concrete limit states, previously proposed strength prediction models for steel headed stud anchors have either not been fully implemented or have been adopted with modifications that do not adequately account for all failure mechanisms, potentially leading to an unconservative strength prediction model.

An extensive database of push-out tests from the literature has been compiled, focusing on common shear stud configurations, particularly those with 0.75 in. (19 mm) or less diameter studs in perpendicular concrete-filled steel composite deck under monotonic loading. The study also includes push-out tests with parallel deck, solid slabs, and cyclic loading. Experimental results are compared with strength prediction models from the following: 2022 AISC *Specification*, Canadian Standards Association S16:19 (CSA, 2019), Eurocode 4 (CEN, 2004), and Rambo-Roddenberry et al. (2002a, 2002b) with additional validation from composite beam tests.

This paper primarily focuses on strength limit-state design, specifically evaluating the shear strength of steel headed stud anchors in concrete-filled steel composite decks used in building construction, where partial composite action is assumed. Partial composite action is typical in buildings due to shorter spans, lower live-to-dead load ratios, and the use of fewer shear connectors to simplify construction and reduce costs. The study excludes fatigue limit states, which are more relevant in bridge applications.

Two new strength prediction models are presented, specifically to address the limit state of concrete failure, including concrete-pull out and rib shear failure described herein. These models, developed with push-out tests and validated with composite beam tests, modify the 2022 AISC *Specification*, utilizing common factors that are familiar to the specification.

EXPERIMENTAL DATABASES AND STRENGTH MODELS

A significant amount of prior research has been dedicated to understanding the behavior of steel headed stud anchors, especially subjected to monotonic loading. Push-out tests and composite beam test results were gathered from the literature to comprehensively cover numerous configurations of shear studs in concrete-filled steel composite deck. Test specimens from the literature were not considered if failure resulted from experimental test procedures. Both lightweight (LW) and normal weight (NW) concrete test specimens were included. When measured material properties were unavailable, nominal properties were used as noted (see asterisk in Table 1 and Table 4). Concrete strengths originally reported as cube strength (Johnson and Yuan, 1998b; Lloyd and Wright, 1990; Smith and Couchman, 2010) were converted to equivalent cylinder strength; a conversion factor of 0.80 was applied where a cylinder strength was not reported directly. Specific testing details for each test specimen are presented in Bond et al. (2022).

Push-Out Test Database

Specimens with Perpendicular Steel Deck, Monotonically Loaded

A total of 240 push-out test specimens with a steel deck oriented perpendicular to the support beam have been

gathered from 18 studies (Briggs et al., 2022; Cashell and Baddoo, 2014; Ernst, 2006; Hawkins and Mitchell, 1984; Hicks, 2009; Jayas and Hosain, 1988; Johnson and Yuan, 1998b; Lawson et al., 2017; Lim et al., 2020; Lloyd and Wright, 1990; Lyons et al., 1994; Nellinger, 2015; Rambo-Roddenberry et al., 2002a, 2002b; Robinson, 1988; Russell et al., 2021; Smith and Couchman, 2010; Sublett et al., 1992; Vigneri et al., 2022). All tests utilize 0.75 in. (19 mm) studs with deck heights ranging from 1.5 in. (38 mm) to 3 in. (76 mm). All specimens have a steel headed stud anchor diameter-to-flange thickness ratio of greater than 2.5 corresponding to the limit set in the 2022 AISC *Specification*. For consistency in the data analysis, only specimens with through-deck welding were considered. Possible steel headed stud anchor configurations included in the database, shown in Figure 1, include strong (S), weak (W), middle (M) or two strong (2S); two weak (2W), two middle (2M); along with staggered (STAG); and two in line (2L) or alternating (Alt.). A "strong stud" is welded on the side of the deck rib with the most concrete available for shear transfer, typically near the end of the span. A "weak stud" is placed on the side with less concrete, usually near the point of maximum bending moment, resulting in lower shear resistance due to potential concrete-related failure. The "middle" designation refers to studs placed at the center of the deck rib without a raised stiffener. Other stud configurations in Figure 1 include various groupings of strong and weak studs. For these configurations, the distance (e_{mid}) from the center of the stud anchor to the steel deck web, measured at the mid-height of the deck rib, is used to classify the stud position as either strong or weak for further calculations.

Additional testing features are varied between authors in the database and should be considered in the evaluation of the results. For example, features like the weld collar dimension, applied normal force, and use of welded wire mesh and its placement have been found to have varying influence on the ultimate strength of a push-out test specimen (Oehlers and Johnson, 1981; Rambo-Roddenberry et al., 2002b; Smith and Couchman, 2010). These features are not always reported for each study and could contribute to the scatter in the test-to-predicted plots.

Specimens with Parallel Steel Deck, Monotonically Loaded

A total of 30 push-out test specimen with steel deck oriented parallel to the support beam have been gathered from four studies (Briggs et al., 2022; Johnson and Yuan, 1997; Lloyd and Wright, 1990; Zandonini and Bursi, 2000). Each test consists of 0.75 in. (19 mm) or less studs with deck heights ranging from 1.5 in. (38 mm) to 3 in. (76 mm). Only specimens with through-deck welding were considered, and all specimens have a steel headed stud anchor diameter-to-flange thickness ratio of greater than 2.5. Failure modes were noted as either a concrete failure, steel failure, or a combination of the two.

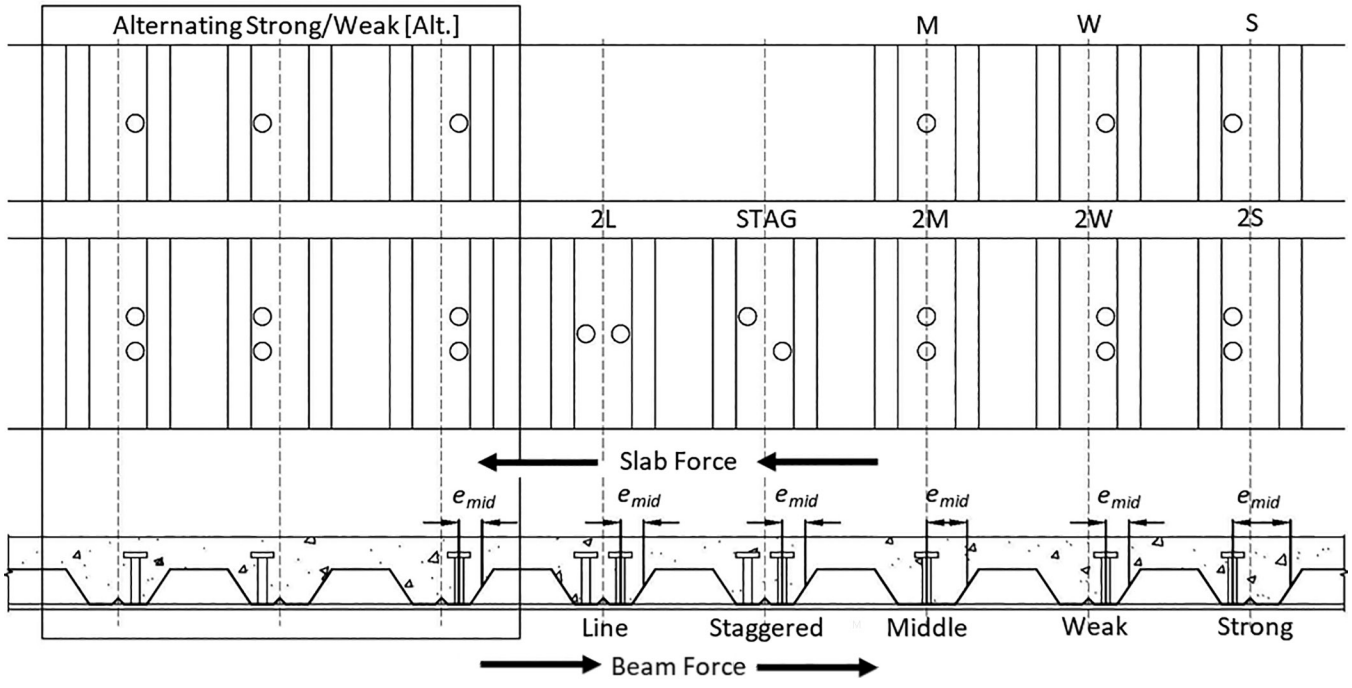

Fig. 1. Stud configurations in deck perpendicular push-out test database.

Cyclically Loaded Specimens

Few studies have been dedicated to the cyclic behavior of steel headed stud anchors in push-out tests. For cyclically loaded specimens, a total of 33 push-out test specimens with steel deck oriented perpendicular or parallel to the support beam have been gathered from three studies (Briggs et al., 2022; Bursi and Gramola, 1999; Hawkins and Mitchell, 1984). All tests utilize 0.75 in. (19 mm) studs with deck heights ranging from 1.5 in. (38 mm) to 3 in. (76 mm). Only specimens with through deck welding were considered and all specimens have a steel headed stud anchor diameter-to-flange thickness ratio of greater than 2.5. Failure modes were noted as either a concrete failure, steel failure, or a combination of the two.

Solid Slab Specimens

Push-out tests with solid slabs were also considered for comparison of the strength prediction models presented in this work; solid slabs refer to cast-in-place concrete slabs without profiled steel decking. The solid slab database is comprised of 165 monotonic test specimens from 15 different studies (An and Cederwall, 1996; Baldwin et al., 1965; Buttry, 1965; Chapman and Balakrishnan, 1964; Chinn, 1965; Dallam, 1968; Hawkins, 1971; Jayas and Hosain, 1988; Mainstone and Menzies, 1967; Menzies, 1971; Ollgaard et al., 1971; Shim et al., 2004; Shoup and Singleton, 1963; Steele, 1967; Viest, 1956), expanding on work by Pallarés and Hajjar (2010). All tests utilize steel headed stud anchor diameters ranging from 0.625 in. (15.9 mm) to 1 in. (25.4 mm) and stud heights ranging from 2 in. (50.8 mm) to 9 in. (227 mm). All specimens have a steel headed stud anchor diameter-to-flange thickness ratio of greater than 2.5. Failure modes have been specified by Pallarés and Hajjar as either stud failure, concrete failure, mixed failure, or not reported (NR).

Composite Beam Tests

A database of composite beam tests from the literature has been compiled and used for analysis from work done by Rambo-Roddenberry et al. (2002b, 2002a). Composite beam tests involve full-scale specimens composed of a steel beam and a concrete slab connected with shear studs and are used to evaluate the integrated behavior and strength of the composite system. The tests used from this database comprise 47 composite beams tests from 12 different sources (Rambo-Roddenberry et al., 2002b, 2002a). All tests utilize 0.75 in. (19 mm) studs with deck heights ranging from 1.5 in. (38 mm) to 3 in. (76 mm) with perpendicular decking and monotonic loading. Steel headed stud anchor heights ranged from 3 in. (76 mm) to 7 in. (177.8 mm). Composite beam tests are used to validate the presented design equations.

REVIEW OF EXISTING STUD STRENGTH MODELS AND FAILURE MODES

Steel Headed Stud Anchor Failure Modes

The ultimate behavior of steel headed stud anchors in perpendicular concrete-filled steel composite deck can be divided up into four failure modes, largely dependent on the location of the stud in the deck rib. Common failure modes are described in this section.

Stud shearing (SS), sometimes referred to as shank shearing, is common for strong-position steel headed stud anchors in perpendicular steel deck. This failure mode consists of a plastic zone directly above the weld collar, followed by fracture of the steel headed stud anchor shank. A shear type failure occurs in the plastic zone in the shank, with minor cracking to the surrounding concrete (Johnson and Yuan, 1998a). This limit state is associated with the upper bound, or cap, of the 2022 AISC *Specification* strength prediction equation.

Rib punching (RP) occurs in weak-position steel headed stud anchors as a localized ductile failure in perpendicular steel deck and is characterized by the crushing of a small portion of concrete in front of the stud, causing the steel deck to bulge and tear (Johnson and Yuan, 1998a). Specimens failing in RP with weak position studs generally exhibit a quick decrease in initial stiffness compared to other failure modes (Briggs et al., 2022). After ultimate strength is reached, a slow decline in strength is shown correlating to the crushing of concrete and tearing of the deck (Briggs et al., 2022). The ultimate strength of weak-position studs is lower compared to strong-position studs, but they exhibit greater ductility.

Rib shear (RS) is a concrete shear failure on the plane on the top of the deck rib, normally seen close to the edge of a specimen. Descriptions of RS and prevention methods for this failure mode are discussed by Ernst (2006). Due to a lack of test data, RS is not discussed further in this paper but is an important topic for future research.

Concrete pull-out (CP) failure is of specific consideration in this paper due to the nature of the representation of this limit state in design strength prediction models. Anchors cast in concrete subject to tension form a concrete failure cone (Shaikh and Yi, 1985). The failure cone develops as the steel headed stud anchor is put into tension due to pry-out action in shear (ACI, 2019). In composite construction, the most likely concrete failure mode is pry-out failure, rather than breakout failure (ACI, 2019; Pallarés and Hajjar, 2010). In perpendicular deck configurations, the failure cone is interrupted by the influence of the deck ribs, with a similar effect of a free edge. CP is most common in strong-position studs, where a larger concrete failure cone can be developed compared to weak-position studs, which fail prematurely due to RP typically at lower

strengths. Experiments show steel headed stud anchors to maintain high initial stiffness for CP, until ultimate strength is reached. Strength drops significantly thereafter when a cone of concrete is torn away from the deck (Briggs et al., 2022).

Many strength prediction models utilize an approach based on prediction of failure modes for assessing the strength of steel headed stud anchors (Pallarés and Hajjar, 2010; Zhai et al., 2018; CSA, 2019). The evolution of the CP failure mode specifically is notable. Shaikh and Yi (1985) observed the influence of edge effects and groups of studs on the concrete failure cone formed for tensile loaded steel headed stud anchors cast in concrete. Hawkins and Mitchell (1984) created equations to model the failure surface area of the failure cone when influenced by steel deck. These failure surface areas were utilized in the strength prediction model of Jayas and Hosain (1988), which have since been adopted by CSA S16:19 (CSA, 2019). Revisions to the prior assumptions of a symmetric failure surface area were made in the work of Lloyd and Wright (1990), which derived wedge-like failure surfaces. Furthermore, Johnson and Yuan (1997) utilize equations for CP based on the torsional strength of the concrete rib.

Some researchers found failures relating to weld quality (Ernst, 2006; Lyons et al., 1994; Rambo-Roddenberry et al., 2002b; Sublett et al., 1992). Additionally, a "rib cracking" failure mode was noted by Lyons et al. and Rambo-Roddenberry et al., consisting of disfigurement of the rib accompanied by deck debonding and a "bowing" of the slab away from the loading beam. These failure modes were considered a result of construction or test configurations, and the specimen associated with these failure modes were excluded from the present work.

Strength Prediction Models

Rambo-Roddenberry et al. (2002a, 2002b)

The strength prediction model of Rambo-Roddenberry et al. (2002b) was derived on the basis of 202 push-out tests conducted by Rambo-Roddenberry and colleagues, combined with push-out tests from Lyons et al. (1994), Sublett et al. (1992), and Diaz et al. (Rambo-Roddenberry et al., 2002b). A grouping factor (R_{g_rod}), placement factor (R_{p_rod}), and deck thickness factor (R_{d_rod}) were empirically derived from the stated tests and validated with push-out tests from various authors (Jayas and Hosain, 1989; Johnson and Yuan, 1997; Lloyd and Wright, 1990; Mottram and Johnson, 1990; Robinson, 1988). The strength prediction model of Rambo-Roddenberry et al. (2002b) is summarized in Equation 1.

For studs in 2 in. and 3 in. decks where $d/t \le 2.7$:

$$Q_{ROD} = 0.5A_s\sqrt{f_c'E_c} \le R_{p\_rod}R_{g\_rod}R_{d\_rod}A_sF_u \qquad (1)$$

R_{p_rod} = 0.68 for $e_{mid} \ge 2.2$ in. (strong position studs)
= 0.48 for $e_{mid} < 2.2$ in. (weak position studs)
= 0.52 for staggered position studs

R_{g_rod} = 1.00 for one stud per rib or staggered position studs
= 0.85 for two studs per rib

R_{d_rod} = 1.00 for all strong position studs
= 0.88 for 22-gauge deck (weak studs)
= 1.00 for 20-gauge deck (weak studs)
= 1.05 for 18-gauge deck (weak studs)
= 1.11 for 16-gauge deck (weak studs)

where d is the diameter of the steel headed stud anchor, t is the thickness of the base metal, A_s is the nominal area of the shear stud, f_c' is the compressive strength of the concrete in ksi, E_c is the Young's modulus of elasticity for concrete in ksi, and F_u is the tensile strength of the shear stud.

CSA S16:19

The 2019 CSA *Design of Steel Structures* (CSA, 2019) strength equation for studs in solid slabs is similar to the 2022 AISC *Specification* strength shown in Equation 1 without the R_p or R_g factors. Perpendicular and parallel deck are accounted for with additional equations. The concrete pull-out area, A_p, is described in work by Jayas and Hosain (Jayas and Hosain, 1988) as a square pyramidal concrete failure cone that radiates down from the top center of the stud head. Equations for this area are based on assumptions from Al-Majhdowi (1975), which only consider a stud placed in the middle of the deck rib. Equations for the concrete pull-out area for varied stud positions are not provided. For studs in solid slabs:

$$Q_{CSA\_SS} = 0.5\phi_{sc}A_s\sqrt{f_c'E_c} \le A_sF_u \qquad (2)$$

where the resistance factor, ϕ_{sc}, is 0.80. For comparison to other models, the test-to-predicted ratios are presented without the 0.80 resistance factor. For studs in slabs with steel deck with ribs perpendicular to the beam:

$$Q_{CSA} = C_dA_p\rho\sqrt{f_c'} \le Q_{CSA\_SS} \qquad (3)$$

where $C_d = 0.35$ for a 3 in. (75 mm) high deck, $C_d = 0.61$ for a 1.5 in. (38 mm) high deck, and ρ is the concrete density. For deck heights between 3 in. and 1.5 in., a linear interpolation was taken for the coefficient C_d. For example, C_d = 0.52 for a 2 in. high deck.

Eurocode 4

The strength equation presented in *Design of Composite Steel and Concrete Structures* (CEN, 2004) is similar to the 2022 AISC *Specification* strength with lower coefficients

and the inclusion of a partial safety factor, γ_v. An additional factor, k_t, accounts for reduction in strength due to the presence and orientation of the deck.

$$Q_{EN4} = \min\left(\frac{k_t 0.8 F_u \pi d^2}{4\gamma_v}, \frac{k_t 0.29 \alpha d^2 \sqrt{f'_c E_c}}{\gamma_v}\right) \quad (4)$$

where $\alpha = 0.2\left(\frac{H}{d}+1\right)$ for $3 \le \frac{H}{d} \le 4$ or $\alpha = 1$ for $\frac{H}{d} > 4$. For parallel decking:

$$k_t = 0.6\frac{w_r}{h_r}\left(\frac{H}{H-h_r}-1\right) \le 1.0 \quad (5)$$

where w_r is the average rib width, h_r is the height of the rib, and H is the height of the stud. For perpendicular decking:

$$k_t = \frac{0.7}{\sqrt{n_r}}\frac{w_r}{(H-h_r)}\left(\frac{H}{H-h_r}-1\right) \quad (6)$$

where n_r is the number of studs per rib. See EN 1994-1-1, Table 6.2, for restrictions on k_t (CEN, 2004).

AISC Specification

The steel headed stud anchor strength equation presented in the 2022 AISC *Specification* originated from work by Ollgaard et al. (1971). Empirical equations were adopted to predict the shear strength of a single stud embedded in LW or NW concrete (e.g., Equation 7). The original upper bound (e.g., cap), A_sF_u, proposed by Ollgaard et al. has since been adjusted to include considerations of stud position in the trough and the number or grouping of studs. The grouping factor, R_{g_rod}, and placement factor, R_{p_rod}, were empirically derived from research done by Rambo-Roddenberry et al. (2002b). AISC adopted the R_p factor, modifying R_{p_rod} (e.g., an increase from 0.68 to 0.75 for strong position studs and 0.48 to 0.60 for weak position studs) and the deck gauge reduction, R_{d_rod}, was left out.

$$Q_{AISC} = 0.5A_s\sqrt{f'_c E_c} \le R_g R_p A_s F_u \quad (7)$$

where Q_{AISC} is in psi units.

RESULTS AND DISCUSSION

Perpendicular Deck Database Comparison to Rambo-Roddenberry et al., CSA S16:19, Eurocode 4, and the 2022 AISC *Specification*

Figure 2 compares the experimental strength of each push-out test, Q_E, described in the Methods section, to the predicted strength of four models for the shear resistance of steel headed stud anchors [Rambo-Roddenberry et al. (2002b) (Q_{ROD}); CSA S16:19 (CSA, 2019) (Q_{CSA}); Eurocode 4 (CEN, 2004) (Q_{EN4}); and the 2022 AISC *Specification* (Q_{AISC}) predicted strength]. To balance comparisons, the partial safety factor and resistance factor (safety factor) of the Eurocode 4 and CSA S16:19 strength prediction models, respectively, were both set to 1.00. The red x above or below for each specimen in Figure 2(d) signifies the controlling side of the strength prediction equation. For example, if the cap strength (i.e., $R_pR_gA_sF_u$) controlled, a red x would appear above the marker at the top of the graph, otherwise the lower bound of the strength prediction controlled and the red x appears below the marker, Equation 7. LW and NW concrete are delineated with a hollow or shaded symbol, respectively. Table 1 includes the test series number, identifying which tests belong to which study and if the nominal steel headed stud anchor strength, F_u, was used in calculations.

Table 2 shows a summary of the test-to-predicted ratios for the considered strength prediction model's average, minimum, maximum, standard deviation (StDev), and coefficient of variance (CoV). Rambo-Rodenberry's (2002b) model was found to accurately predict steel headed stud anchor strength and was partially adopted by AISC with modifications to the coefficients. In the CSA S16:19 model, the concrete pull-out area is calculated with an assumption the stud lies in the center of the deck trough, even for studs in the strong and weak positions. For these reasons, the model was found to be somewhat unconservative for studs in perpendicular concrete-filled steel composite deck.

In the 2022 AISC *Specification* equation, all but thirteen of the tests are controlled by the cap. The lower bound of Equation 7, $0.5A_s\sqrt{f'_c E_c}$, is applied to all studs, including those in a perpendicular deck, but was developed using only studs in solid slabs (Ollgaard et al., 1971). Specimens with perpendicular steel deck have been observed to have lower strengths compared to similar specimens with a solid slab (Hawkins and Mitchell, 1984; Jayas and Hosain, 1988; Rambo-Roddenberry et al., 2002b; Sublett et al., 1992). Therefore, an alteration to the lower bound of the strength prediction equation, for a stud in perpendicular deck, is desired to account for the decrease in available strength.

Reassessment of Steel Headed Stud Anchors in the 2022 AISC *Specification*

Perpendicular Deck

Two new strength prediction models adapted from the 2022 AISC *Specification* are presented herein. The first design strength formula is termed the R_pR_g adjusted AISC strength prediction model and is shown in Equation 8. The R_p and R_g factors account for the reduction in strength due to the position in the trough and the grouping of the steel headed stud anchors. Similarly, this approach adjusts the predicted

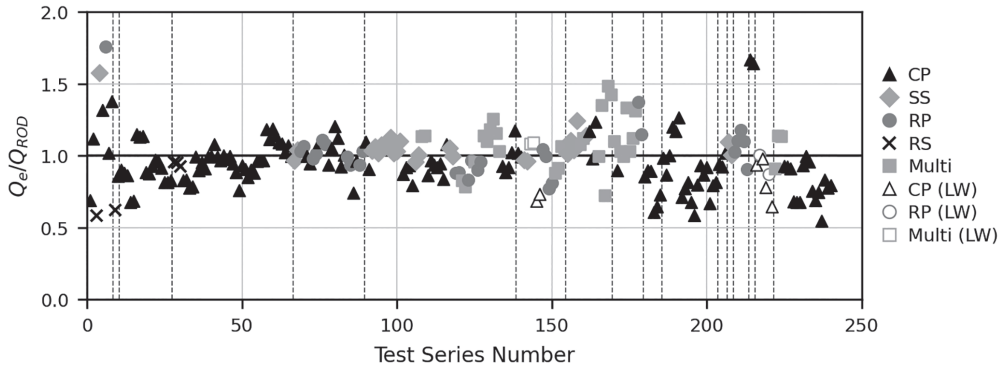

(a) Rambo-Roddenberry et al. (2002)

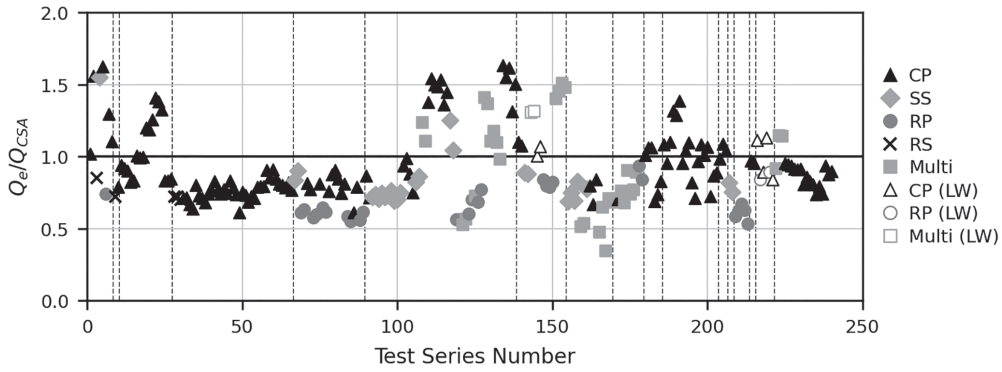

(b) CSA S16:19 (2019)

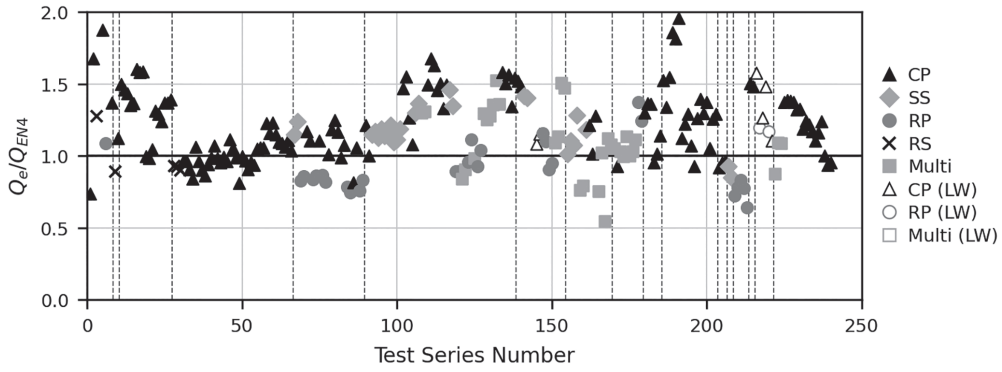

(c) Eurocode 4 (CEN, 2004)

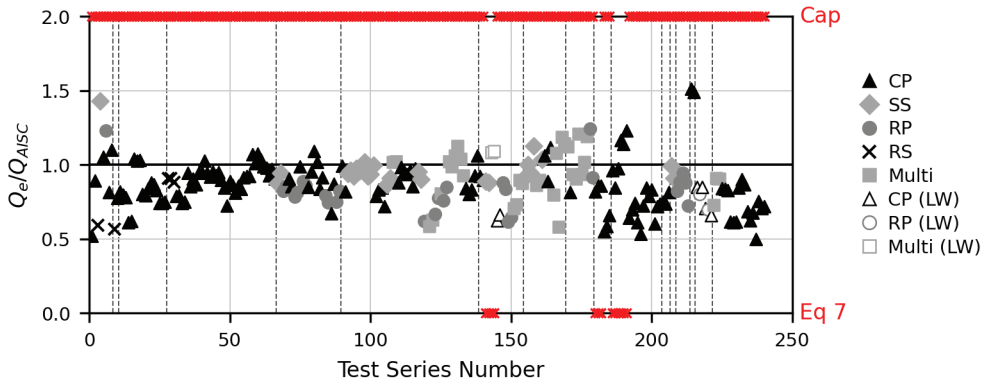

(d) 2022 AISC Specification

Fig. 2. Test-to-predicted ratios for shear strength of steel headed stud anchors.

Table 1. Reference and Test Series Number—Perpendicular Decking		
Reference	**First Test Series Number**	**Last Test Series Number**
Hawkins and Mitchell (1984)	1	8
Jayas and Hosain (1988)*	9	10
Robinson (1988)	11	27
Lloyd and Wright (1990)*	28	66
Sublett et al. (1992)*	67	89
Lyons et al. (1994)	90	138
Johnson and Yuan (1998b)	139	154
Rambo-Roddenberry et al. (2002a)	155	169
Ernst (2006)	170	179
Hicks (2009)	180	185
Smith and Couchman (2010)	186	203
Cashell and Baddoo (2014)	204	206
Nellinger (2015)	207	208
Lawson et al. (2017)	209	213
Lim et al. (2020)	214	215
Briggs et al. (2022)	216	221
Vigneri (2021)	222	224
Russell et al. (2021)	225	240
* Nominal steel headed stud anchor strength, F_u, used in calculations		

Table 2. Test-to-Predicted Ratio per Each Strength Prediction Model				
	Q_E/Q_{AISC}	Q_E/Q_{ROD}	Q_E/Q_{CSA}	Q_E/Q_{EN4}
Average	0.873	0.978	0.901	1.175
Max	1.513	1.760	1.634	2.197
Min	0.497	0.548	0.347	0.547
StDev	0.162	0.183	0.258	0.274
CoV	0.185	0.187	0.286	0.233

strength to address concrete failures in steel deck by applying the 2022 AISC *Specification* R_p and R_g factors to the lower bound of the stud strength equation, $0.5A_s\sqrt{f'_cE_c}$. The R_pR_g adjusted AISC strength prediction model is:

$$Q_{R_pR_g} = R_pR_g(0.5A_s\sqrt{f'_cE_c}) \le R_pR_gA_sF_u \quad (8)$$

The second strength prediction method is the result of a regression analysis performed on specimens that failed in concrete pull-out, similar to the derivation of the original R_p and R_g values (Rambo-Roddenberry et al., 2002b, 2002a). The linear regression compared the existing lower bound of the stud strength equation, $0.5A_s\sqrt{f'_cE_c}$, with the experimental specimen strengths from the perpendicular deck database. The slope of the regression line with a y-intercept of zero is then taken as the concrete failure regression coefficient, R_r, to adjust the lower bound of the AISC strength prediction model. The development of the R_r coefficient is presented for all deck configurations in the following sections and summarized in Equation 9. This method is labeled as the LB-regression adjusted AISC strength prediction model and is shown in Equation 9. The regression analysis for perpendicular deck is shown in Figure 3. The LB-regression adjusted AISC strength prediction is:

$$Q_{LB} = R_r(0.5A_s\sqrt{f'_cE_c}) \le R_pR_gA_sF_u \quad (9)$$

For ¾-in.-diameter studs:

$R_r = 0.65$ (for perpendicular deck)

$R_r = 0.75$ (for parallel deck)

For studs with diameters between ¾ in. and 1.0 in.:

$R_r = 0.80$ (for solid slabs)

Test-to-predicted graphs for each method are presented in Figure 4 for tests with deck perpendicular. Test series numbers are provided in Table 1 for perpendicular decking along with an indication of nominal vs. measured stud strength property usage for different studies. Similar to Figure 2, the red x above or below the symbol for each specimen signifies which portion of the respective strength prediction equation controlled.

Descriptive statistics of the test-to-predicted ratios are shown in Table 3 for the two proposed strength models. The R_pR_g adjusted AISC strength prediction model, Equation 7, uses factors that are already familiar to the designer and does not require a prediction of the limit state in design. The LB-regression adjusted AISC strength prediction model has been found to adequately predict stud strength for the perpendicular push-out test specimen. Both methods account for the metal deck in the lower bound of the strength prediction equation and result in a test-to-predicted ratio closer to 1.0.

While the proposed equations improve the accuracy of the test-to-predicted ratios, the CoV for the LB-regression adjusted AISC model increases slightly compared to the existing model, whereas the R_pR_g adjusted AISC model achieves a marginally lower CoV. The increase in variability for the LB-regression model may be attributed to the more complex adjustments introduced by that equation. Despite this, both proposed models offer more accurate predictions in terms of the test-to-predicted ratios. Further experimental data and refinements are recommended to address this variability and to improve the consistency of the predictions.

Parallel Deck

The new strength prediction models were also considered for monotonically loaded push-out tests with parallel deck. Details from the parallel deck push-out test database were

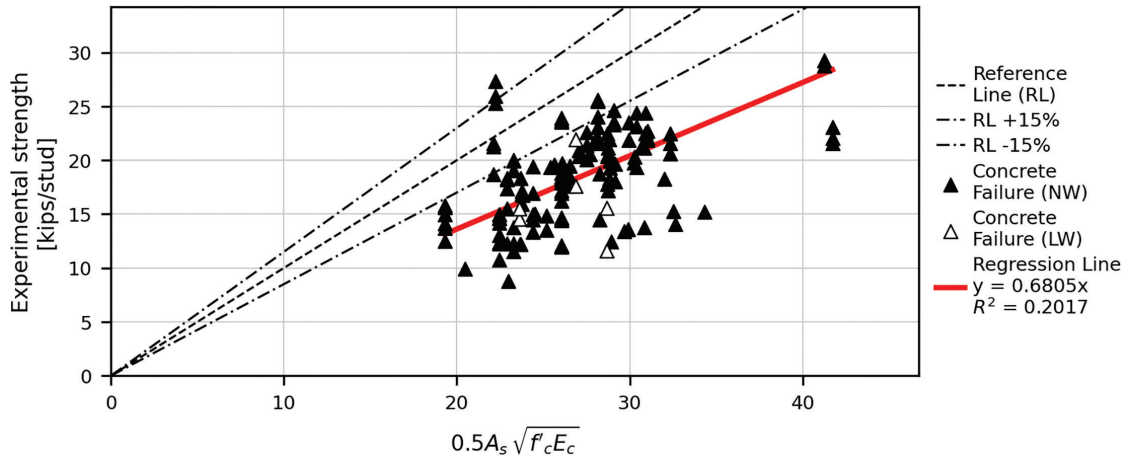

(a) Experimental versus predicted stud strength

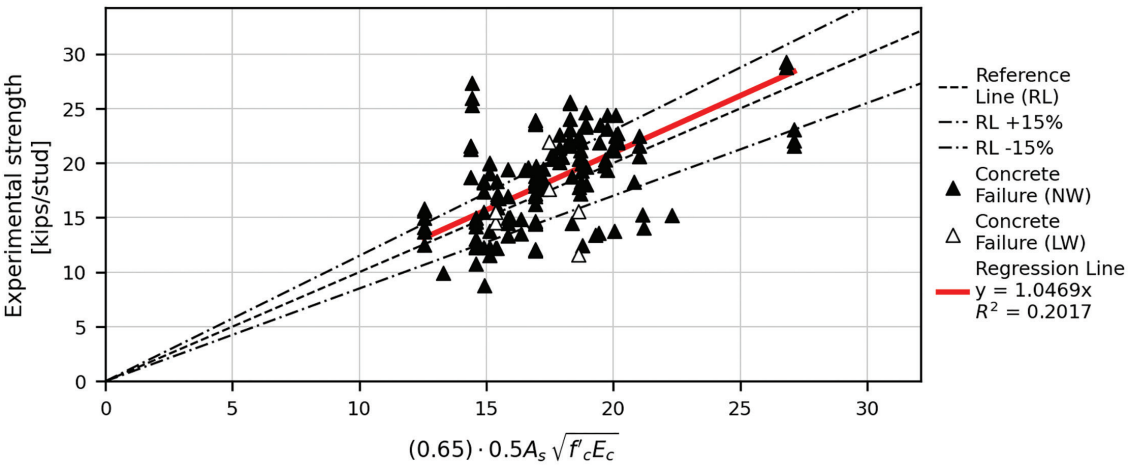

(b) Regression line defining the LB-regression coefficient

Fig. 3. Linear regression analysis for perpendicular deck specimens with concrete pull-out failure.

Table 3. Perpendicular Test-to-Predicted Ratio per Each Presented Strength Prediction Model for Perpendicular Steel Deck			
	Q_E/Q_{AISC}	Q_E/Q_{RpRg}	Q_E/Q_{LB}
Average	0.873	1.009	1.050
Max	1.513	1.639	1.892
Min	0.497	0.579	0.579
Stdev	0.162	0.184	0.216
CoV	0.185	0.183	0.206
Note: R_r = 0.65 for perpendicular deck remains unchanged in Equation 9.			

presented earlier. Figure 5 shows the results from the linear regression comparing the existing lower bound of the stud strength equation, $0.5A_s\sqrt{f'_cE_c}$, with the experimental strength of concrete failures in the parallel deck database. From the slope of the regression line, the LB regression coefficient is taken as $R_r = 0.75$ for the parallel deck case.

The R_pR_g adjusted AISC strength prediction model and LB-regression adjusted AISC strength prediction model are analyzed using the experimental strengths of the parallel deck database and compared with the 2022 AISC *Specification* strength prediction in Figure 6. Table 4 matches the test series number with its corresponding reference. Descriptive statistics of the test-to-predicted ratios for each strength prediction model are shown in Table 5. The two new strength prediction models increase the average test-to-predicted ratio by about 0.05. Thus, the 2022 AISC *Specification* equations give adequate predictions of the strengths of steel headed stud anchors in parallel deck.

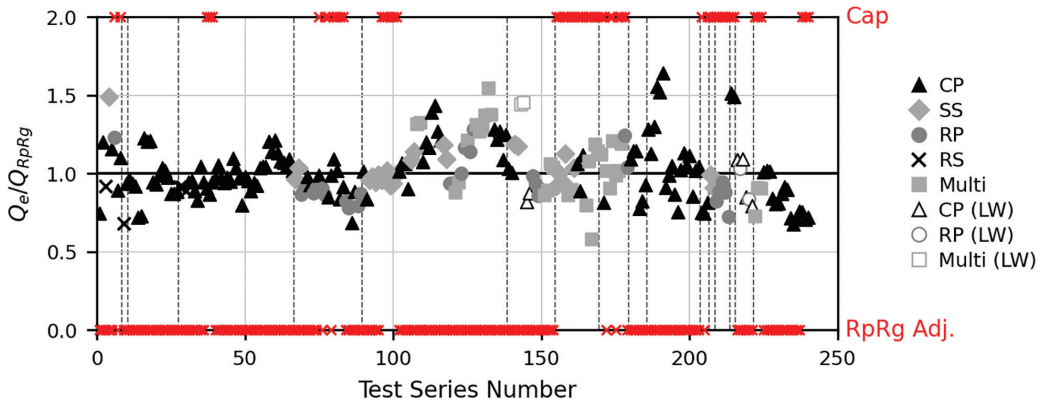

(a) R_pR_g adjusted AISC

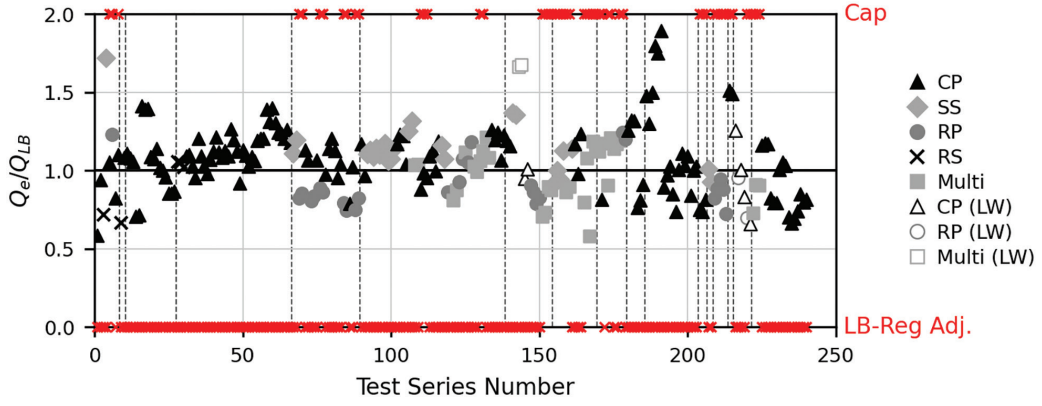

(b) LB-regression adjusted AISC

Fig. 4. Perpendicular deck test-to-predicted strengths for steel headed stud anchors.

Table 4. Reference and Test Series Number—Parallel Deck		
Reference	**First Test Series Number**	**Last Test Series Number**
Lloyd and Wright (1990)*	1	3
Johnson and Yuan (1997)	4	21
Bursi and Gramola (1999)	22	27
Briggs et al. (2022)	28	30
* Nominal steel headed stud anchor strength (F_u) used in calculations		

Table 5. Parallel Deck Test-to-Predicted Ratio per Each Presented Strength Prediction Model			
	Q_E/Q_{AISC}	Q_E/Q_{RpRg}	Q_E/Q_{LB}
Average	1.011	1.061	1.057
Max	1.391	1.432	1.432
Min	0.677	0.700	0.700
StDev	0.180	0.183	0.183
CoV	0.178	0.172	0.173

Cyclic Loading

The cyclically loaded push-out test database with perpendicular and parallel deck configurations is presented in the Methods section. The LB regression coefficient, R_r, is adopted from the monotonically loaded perpendicular and parallel specimens for each case.

The R_pR_g adjusted AISC strength prediction model and LB-regression adjusted AISC strength prediction model are evaluated against the experimental strengths of the cyclic push-out test database and their results are compared with the existing AISC strength prediction in Figure 7. Table 6 provides the test series number with its corresponding reference, while Table 7 shows the descriptive statistics for these comparisons. Consistent with the findings of Pallarés and Hajjar (2010) for solid slabs, the 2022 AISC *Specification* stud strength prediction is generally conservative for cyclically loaded specimens with parallel deck orientation. However, for cyclically loaded specimens with perpendicular decking, the 2022 AISC *Specification* stud strength prediction tends to be unconservative, even when applying the 0.75 strength reduction factor for cyclically loaded steel headed stud anchors. This unconservativeness is partly due to the baseline monotonic strengths also being underestimated.

To further understand this relationship, the ratio of the experimental cyclic strength, Q_{E_C}, to monotonic strength,

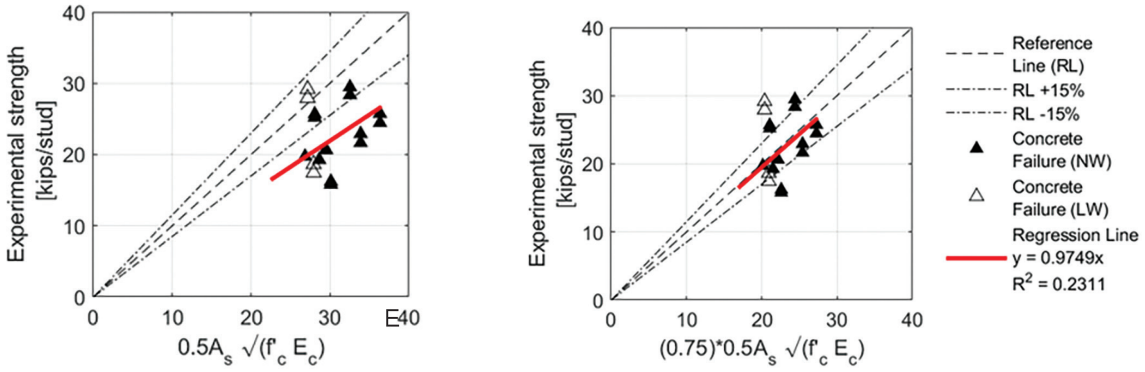

(a) Without LB-regression coefficient *(b) With LB-regression coefficient*

Fig. 5. Linear regression analysis for parallel deck specimen with concrete failure.

Q_{E_M}, was calculated for identical perpendicular deck push-out test specimens from (Briggs et al., 2022). This dataset, although limited to four specimens, shows an average cyclic-to-monotonic strength ratio of 0.901 with a standard deviation of 0.101, as shown in Table 7. These findings suggest that if the monotonic strength prediction is adjusted, the cyclic strength prediction may also become more accurate. Additional cyclic test data, especially for composite steel decks with perpendicular decking, would help refine these predictions.

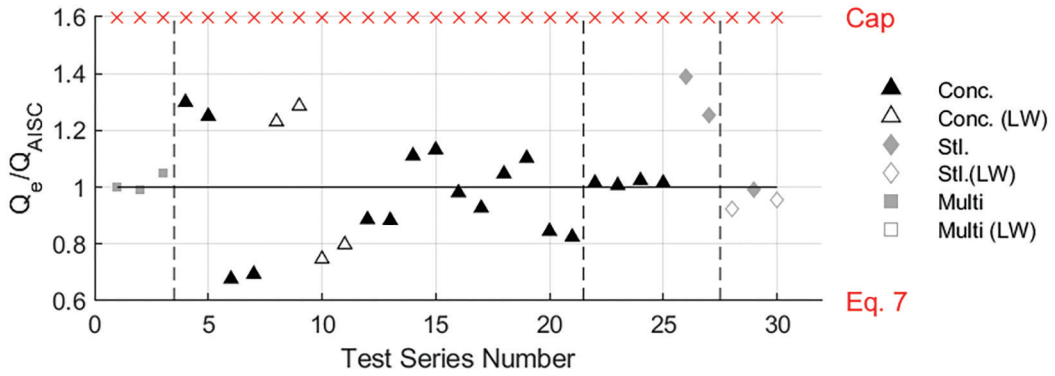

(a) 2022 AISC Specification

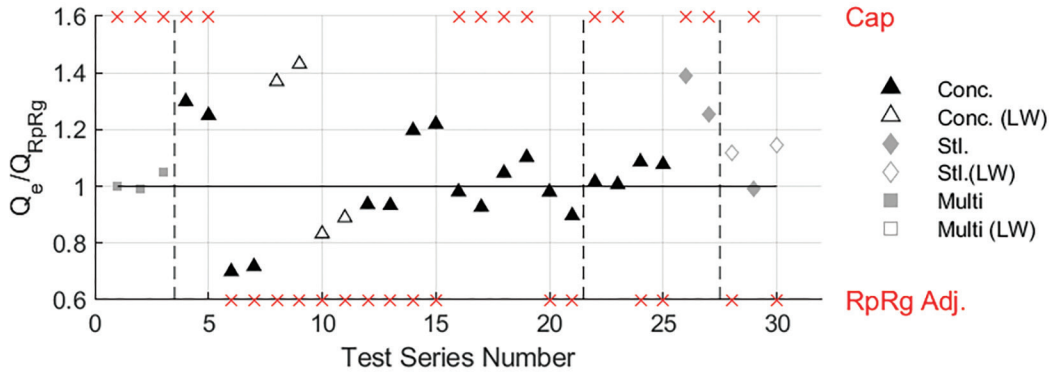

(b) R_pR_g *adjusted AISC*

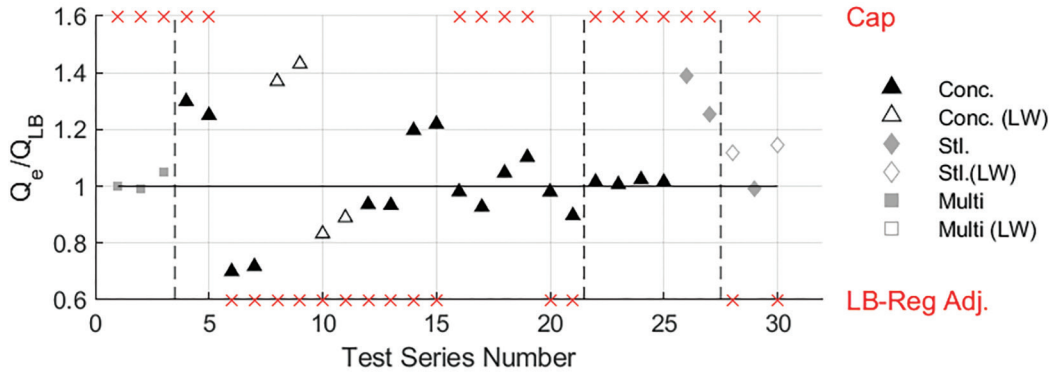

(c) LB-regression adjusted AISC

Fig. 6. Parallel deck test-to-predicted graphs for steel headed stud anchors.

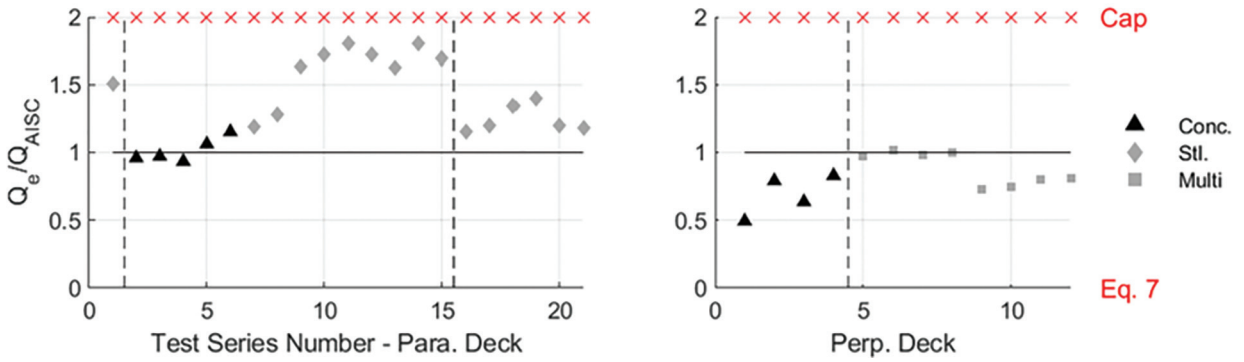

(a) 2022 AISC Specification

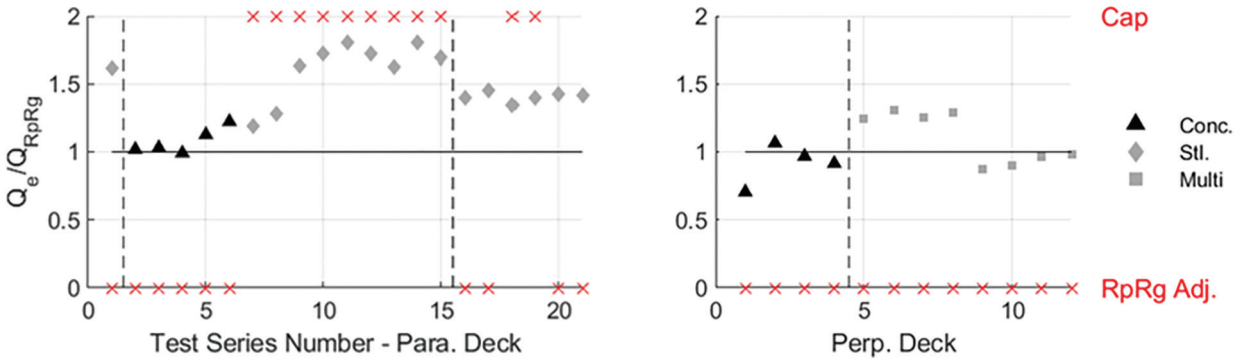

(b) R_pR_g *adjusted AISC*

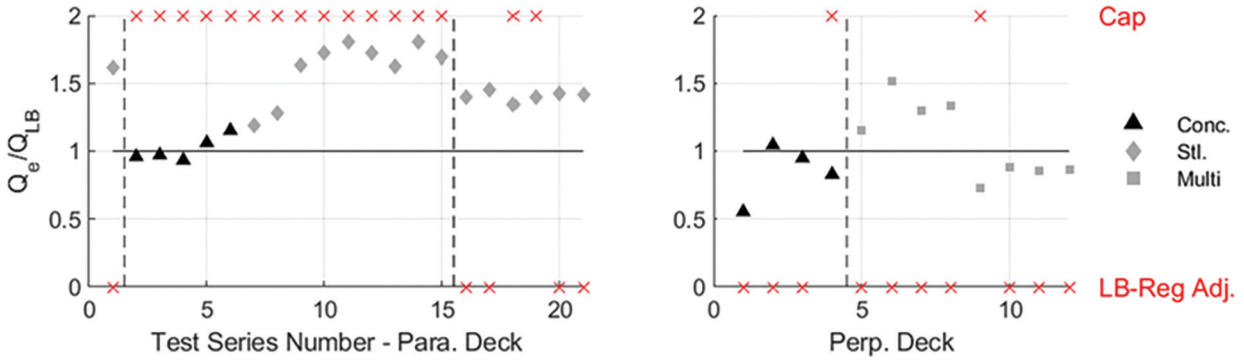

(c) LB-regression adjusted AISC

Fig. 7. Cyclically loaded test-to-predicted graphs for steel headed stud anchors.

Table 6. Reference and Test Series Number—Cyclically Loaded					
Perpendicular Decking			Parallel Decking		
Reference	First Test Series Number	Last Test Series Number	Reference	First Test Series Number	Last Test Series Number
Hawkins and Mitchell (1984)	1	4	Hawkins and Mitchell (1984)	1	1
Briggs et al. (2022)	5	12	Bursi and Gramola (1999)	2	15
			Briggs et al. (2022)	15	21

Table 7. Cyclically Loaded Test-to-Predicted Ratio per Each Presented Strength Prediction Model							
	Perpendicular Decking			Parallel Decking			
	Q_E/Q_{AISC}	Q_E/Q_{RpRg}	Q_E/Q_{LB}	Q_E/Q_{AISC}	Q_E/Q_{RpRg}	Q_E/Q_{LB}	Q_{E_C}/Q_{E_M}
Average	0.818	1.039	1.000	1.359	1.424	1.410	0.901
Max	1.021	1.311	1.512	1.806	1.806	1.806	1.037
Min	0.493	0.705	0.553	0.934	0.991	0.934	0.781
StDev	0.159	0.194	0.278	0.293	0.263	0.283	0.101
CoV	0.194	0.186	0.278	0.216	0.184	0.201	0.112

Solid Slabs

Details of the solid slab push-out test database are presented in the Methods section. From work by Pallarés and Hajjar (2010), a reduction factor of 0.65 was presented for solid slabs applied to A_sF_u. The 2022 AISC *Specification* adopted a 0.75 reduction factor for solid slabs, in the form of the R_p factor. However, both of these methods rely on an adjustment of the steel cap. The presented strength prediction models present an adjustment to the lower bound to account for concrete related failures in solid slabs.

Solid slab push-out tests with concrete failures exhibit different behavior and properties compared to comparable members with steel deck. Thus, a linear regression coefficient, R_r = 0.80, for the LB-regression adjusted AISC strength prediction model with solid slabs was developed utilizing push-out specimen from the solid slab database failing with concrete related failures, as shown in Figure 8.

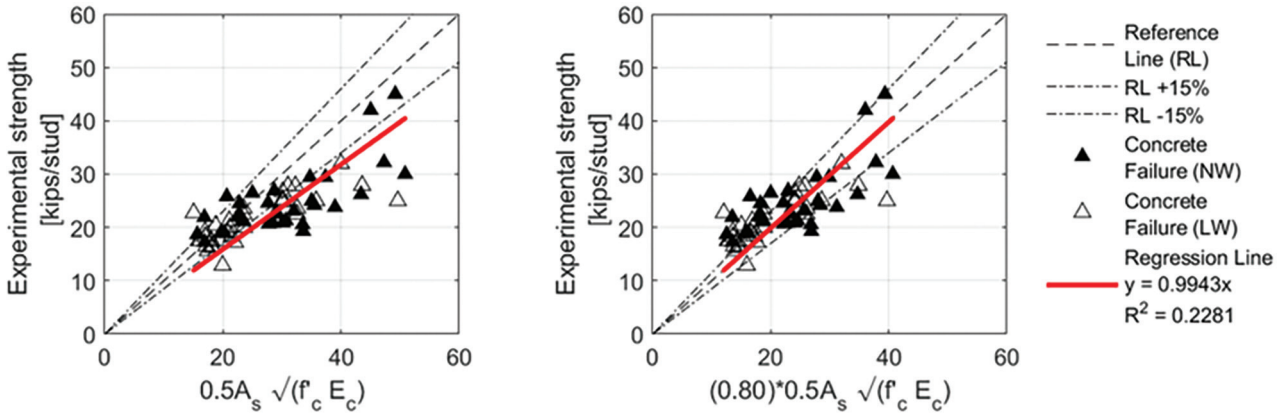

(a) Without LB-regression coefficient *(b) With LB-regression coefficient*

Fig. 8. Linear regression analysis for solid slab specimen with concrete failure.

The R_pR_g adjusted and LB-regression adjusted models are analyzed using the experimental strengths of the solid slab database and compared with the existing 2022 AISC *Specification* strength prediction in Figure 9. Table 8 matches the test series number with its corresponding reference. A summary of the average, minimum, maximum, StDev, and CoV of the test-to-predicted ratios for each strength prediction model is shown in Table 9.

Lightweight vs. Normal Weight Concrete

Descriptive statistics of the test-to-predicted ratios, disaggregated by LW and NW concrete specimen, for push-out tests with a perpendicular deck and a parallel deck are shown in Tables 10 and 11, respectively. For a perpendicular deck, the LW concrete specimen (10 total specimens) generally failed with a more unconservative ratio compared

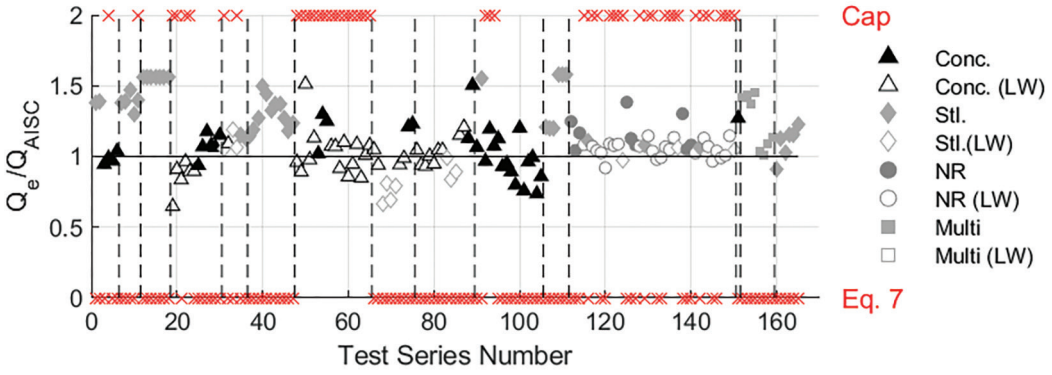

(a) 2022 AISC Specification

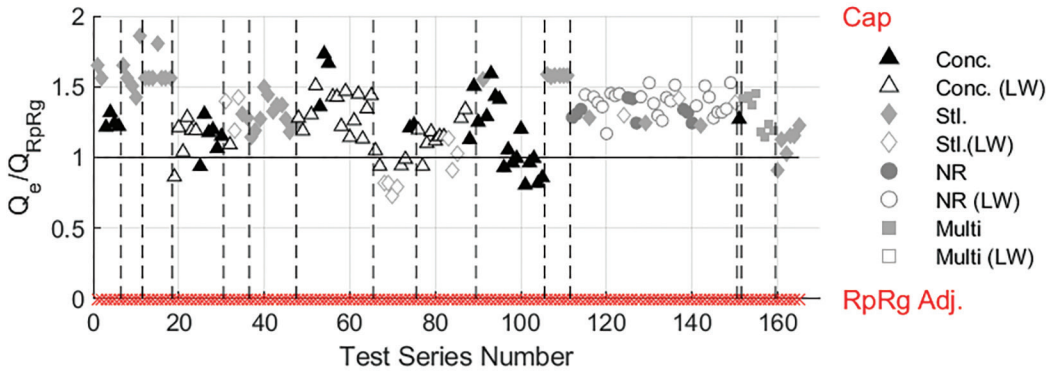

(b) R_pR_g *adjusted AISC*

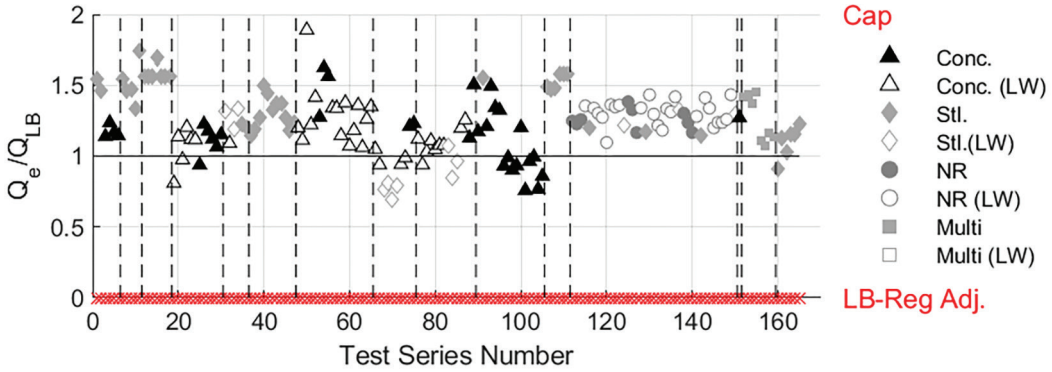

(c) LB-regression adjusted AISC

Fig. 9. Solid slab test-to-predicted graphs.

Table 8. Reference and Test Series Number—Solid Slab		
Reference	**First Test Series Number**	**Last Test Series Number**
Viest (1956)	1	6
Shoup and Singleton (1963)	7	11
Chapman and Balakrishnan (1964)	12	18
Buttry (1965)	19	30
Chinn (1965)	31	36
Mainstone & Menzies (1967)	37	47
Steele (1967)	48	65
Dallam (1968)	66	75
Baldwin et al. (1965)	76	89
Hawkins (1971)	90	105
Menzies (1971)	106	111
Ollgaard et al. (1971)	112	150
Jayas and Hosain (1989)	151	151
An and Cederwall (1996)	152	159
Shim et al. (2004)	160	165

Table 9. Solid Slab Test-to-Predicted Ratio per Each Presented Strength Prediction Model			
	Q_E/Q_{AISC}	Q_E/Q_{RpRg}	Q_E/Q_{LB}
Average	1.118	1.291	1.237
Max	1.575	2.016	1.890
Min	0.647	0.728	0.691
StDev	0.206	0.223	0.211
CoV	0.184	0.172	0.170

Table 10. Perpendicular Deck Test-to-Predicted Ratio Disaggregated by LW and NW Concrete						
	NW Concrete (230 Specimens)			LW Concrete (10 Specimens)		
	Q_E/Q_{AISC}	Q_E/Q_{RpRg}	Q_E/Q_{LB}	Q_E/Q_{AISC}	Q_E/Q_{RpRg}	Q_E/Q_{LB}
Average	0.876	1.008	1.049	0.802	1.028	1.070
Max	1.513	1.639	1.892	1.090	1.454	1.677
Min	0.497	0.579	0.579	0.623	0.791	0.658
StDev	0.161	0.182	0.209	0.161	0.235	0.340
CoV	0.184	0.180	0.199	0.200	0.228	0.318

Table 11. Parallel Deck Test-to-Predicted Ratio Disaggregated by LW and NW Concrete						
	NW Concrete (24 Specimens)			LW Concrete (6 Specimens)		
	Q_E/Q_{AISC}	Q_E/Q_{RpRg}	Q_E/Q_{LB}	Q_E/Q_{AISC}	Q_E/Q_{RpRg}	Q_E/Q_{LB}
Average	1.02	1.04	1.04	0.99	1.13	1.13
Max	1.39	1.39	1.39	1.29	1.43	1.43
Min	0.68	0.70	0.70	0.75	0.83	0.83
StDev	0.17	0.17	0.17	0.22	0.24	0.24
CoV	0.17	0.16	0.16	0.22	0.21	0.21

to the NW concrete specimen (230 total specimens). The parallel deck specimens exhibited a similar result for the 2022 AISC *Specification* prediction with a much smaller margin between LW and NW specimens. However, in general, more data is preferred to determine the effects of LW vs. NW concrete in push-out tests.

Composite Beam Test

Two new strength prediction methods were developed in the Results and Discussion section from a database of push-out tests with steel deck and solid slabs. Full-scale beam tests can offer insight to steel headed stud anchor behavior in composite beams subject to flexure. This section will validate the proposed strength prediction models with experimental composite beams tests with perpendicular slabs from the literature. Partially composite beam tests were compiled from work done by Rambo-Roddenberry et al. (2002b, 2002a), which include tests summarized by Grant et al. (1977), Robinson (1988), Jayas and Hosain (1989), and others. All calculations utilized measured properties. The AISC predicted percent composite and experimental percent composite for each test is shown in Bond et al. (2022).

The maximum experimental moment, M_e, is compared to strengths calculated using the AISC flexural strength for composite beams, M_{AISC}, and the flexural strengths utilizing the proposed stud strengths, M_{RpRg} and M_{LB}, shown in Figure 10. Table 12 matches the test series number with its corresponding reference. A summary of the statistical parameters for the test-to-predicted ratios for each strength prediction model is shown in Table 13. These ratios demonstrate that the 2022 AISC *Specification* is slightly unconservative for predicting flexural strength and the proposed equations bring the average test-to-predicted ratio closer to 1.0 without increasing the CoV.

Future Work

Future work could explore a simplified approach to stud strength prediction based on failure modes. For example, this study shows that the current 2022 AISC *Specification* formula effectively addresses the SS failure mode. For the RP failure mode, existing prediction equations are accurate but complex, highlighting a need for simplification (Johnson and Yuan, 1997). Additional experimental data is required to better understand the RS failure, particularly regarding edge effects and detailing, such as pour stops. Finally, the CP failure mode is the primary focus in this work. A failure mode-based strength prediction model could estimate shear connection strength for each failure mode (e.g., Q_{CP}, Q_{ss}, Q_{DP}, Q_{RS}), with the minimum value determining the expected failure mode and design shear strength.

Variability in the test-to-predicted results stems from differences in traditional push-out test setups, material properties, and uneven resistance distribution among multiple studs. To address this, new push-out test setups have been introduced to better assess shear stud strength (Briggs et al., 2022; Sanden, 1996). Updating previous databases with

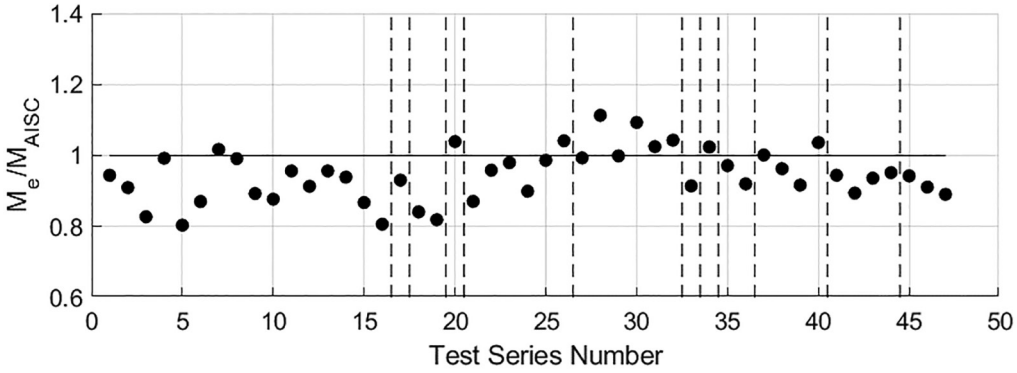

(a) 2022 AISC Specification

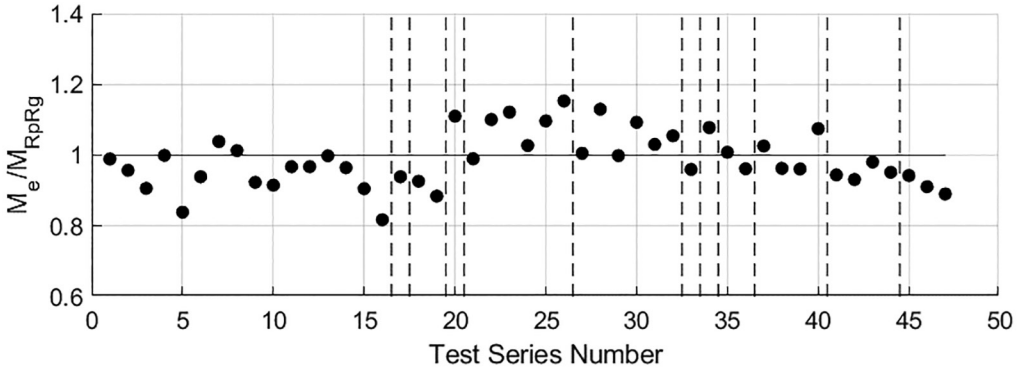

(b) R_pR_g *adjusted AISC*

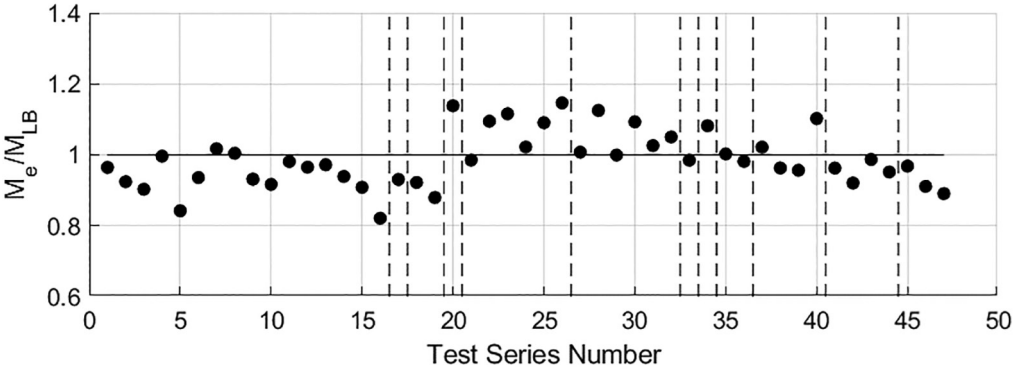

(c) LB-regression adjusted AISC

Fig. 10. Composite beam test, test-to-predicted graphs.

Table 12. Reference and Test Series Number—Composite Beam Tests		
Reference	**First Test Series Number**	**Last Test Series Number**
Grant et al. (1977)	1	16
Robinson and Wallace (1971)	17	17
Fisher et al. (1967)	18	19
Seek et al. (1970)	20	20
Furlong and Henderson (1975)	21	26
Allan et al. (1976)	27	32
Jones (1975)	33	33
Lacap (1975)	34	34
Robinson (1988)	35	36
Jayas and Hosain (1989)	37	40
Gibbings et al. (1993)	41	44
Rambo-Roddenberry et al. (2002a)	45	47

Table 13. Test-to-Predicted Ratio Composite Beam Tests per Each Strength Prediction Model			
	M_E/M_{AISC}	M_E/M_{RpRg}	M_E/M_{LB}
Avg.	0.95	0.99	0.99
Max	1.11	1.15	1.15
Min	0.80	0.82	0.82
StDev	0.07	0.08	0.08
CoV	0.08	0.08	0.08

recent test data would help validate current methods and improve understanding of shear stud behavior.

It is recommended that future work include design strength formulas that address rib shear and rib punching failure. Additionally, steel headed stud anchors in perpendicular deck near the edge of slab may result in a rib shear failure mode and should be examined further with more tests and research (Hawkins and Mitchell, 1984). Specifically, the effect of pour stops and other unique detailing near the edge of slab should be considered where there is a large gap in the literature addressing these conditions.

CONCLUSION

In this work, failure modes in the shear strength prediction of steel-headed studs in concrete-filled steel composite deck and solid slabs is assessed with 468 push-out tests from the literature. The experimental stud strengths have been compared to the stud strength prediction models from Rambo-Roddenberry et al. (2002b, 2002a), CSA S16:19 (2019), Eurocode 4 (CEN, 2004), and the 2022 AISC *Specification*. Test-to-predicted plots of the push-out tests are disaggregated failure mode to demonstrate somewhat unconservative strength predictions for concrete-related failures.

This research highlights potential adjustments to the 2022 AISC *Specification* stud strength equation that will enable a more accurate assessment of strength while retaining the general form of the equation. Test-to-predicted ratios are presented for each test specimen for two new proposed strength prediction methods. The following conclusions are made from this research:

1. Failure modes for steel headed stud anchors in concrete filled steel composite deck can be described as stud shearing, concrete pull-out, rib punching, and rib shear, or a combination of these failure modes. The 2022 AISC *Specification* formula for predicting stud strength is adequate for steel stud failures but produces somewhat unconservative estimates for the concrete pull-out and rib punching failure modes.

2. The stud strength prediction equations from work by Rambo-Roddenberry et al. (2002b) was found to have an acceptable correlation for stud strength. However, the 2022 AISC *Specification* and earlier editions of the *Specification* adopted moderately increased R_p and R_g factors, leading to the somewhat unconservative strength prediction for concrete related failures. For instance, the average test-to-predicted stud strength ratio for the AISC *Specification* is 0.873, compared to 0.978 for the equations by Rambo-Roddenberry et al.

3. To improve the prediction of the concrete pull-out failure mode, new equations are presented for the shear strength prediction of steel headed stud anchors with steel deck. The new models increase the accuracy for the test-to-predicted ratios for a perpendicular deck specimen from 0.87 for the 2022 AISC *Specification* equation to 1.01 for the R_pR_g adjusted strength prediction and 1.05 for the LB regression strength prediction model. Similarly, the models slightly increase the accuracy for the test-to-predicted ratios of flexural strengths for deck perpendicular composite beam tests from 0.95 for the 2022 AISC *Specification* to 0.99 for both the R_pR_g adjusted strength prediction and for the LB regression strength prediction. The authors suggest adopting these models for design applications involving perpendicular decks, as they provide more accurate predictions of stud strength, particularly for concrete-related failure modes.

4. The presented equations (R_pR_g adjusted and LB-regression adjusted strength predictions) were also applied to concrete failure modes for parallel deck and solid slab configurations. Although more data is preferred for parallel deck push-out tests, results here show parallel deck and solid slab configurations to be sufficiently represented by the existing 2022 AISC *Specification* stud strength equation.

5. For the data available, the experimental cyclic strength and monotonic strength of corresponding tests indicates that if the monotonic strength prediction is adjusted, the existing 25% reduction for steel headed stud anchors subjected to cyclic loads is likely to be adequate. In addition, more data is desirable for cyclically loaded concrete-filled steel composite deck with deck perpendicular.

In addition, adapting the proposed approach for calculating the nominal design strength of headed stud steel anchors is primarily justified by its improved ability to predict stud failure modes and its more conservative prediction of the strength for configurations with perpendicular steel decking.

SYMBOLS

A_p	Concrete pull-out area defined in CSA S16:19, in.^{2} (mm^2)
A_s	Area of the steel headed stud anchor shank, in.^{2} (mm^2)
C_d	Deck height coefficient for CSA S16:19 strength prediction method
E_c	Young's modulus of elasticity for concrete, ksi (MPa)
F_u	Tensile strength of steel headed stud anchor, ksi (MPa)
H	Steel headed stud anchor height, in. (mm)
Q_{AISC}	2022 AISC *Specification* predicted strength of a single steel headed stud anchor, kips (kN)
Q_{ROD}	Rambo-Roddenberry predicted strength of a single steel headed stud anchor, kips (kN)
Q_{CSA}	CSA S16:19 predicted strength of a single steel headed stud anchor, kips (kN)
Q_{RpRg}	R_pR_g predicted strength of a single steel headed stud anchor, kips (kN)
Q_{LB}	Lower-bound predicted strength of a single steel headed stud anchor, kips (kN)
R_{d_rod}	Deck gauge factor for Rambo-Roddenberry et al. strength prediction model
R_{g_rod}	Grouping factor for Rambo-Roddenberry et al. strength prediction model
R_{p_rod}	Placement factor for Rambo-Roddenberry et al. strength prediction model
R_g	Grouping factor for 2022 AISC *Specification* strength prediction model
R_p	Placement factor for 2022 AISC *Specification* strength prediction model
R_r	LB-regression coefficient
d	Diameter of steel headed stud anchor shank, in. (mm)
e_{mid}	Distance from center of the steel headed stud anchor to the steel deck web, measured at mid-height of the deck rib, in. (mm)
f_c'	Concrete cylinder compressive strength, ksi (MPa)
h_r	Height of deck rib, in. (mm)
k_t	CSA reduction factor accounting for deck orientation
n_r	Number of studs per rib
t	Thickness of the base metal, in. (mm)
w_r	Average rib width, in. (mm)

ϕ_v Resistance factor for shear strength

γ_v CSA partial safety factor

ρ Concrete density, kip/ft³ (kg/m³)

ACKNOWLEDGMENTS

This material is based upon work supported by the National Science Foundation under Grant 1562669; by the Steel Diaphragm Innovation Initiative, which is funded by the American Institute of Steel Construction (AISC), the American Iron and Steel Institute, the Metal Building Manufacturers Association (MBMA), the Steel Deck Institute (SDI), and the Steel Joist Institute (SJI); and by Northeastern University. The contributions to this research of Nicholas Briggs and Raul Avellaneda are gratefully acknowledged.

REFERENCES

ACI (2019), *Building Code Requirements for Structural Concrete and Commentary, ACI 318-14,* American Concrete Institute, Farmington Hills, Mich.

Ahmed, I.M. and Tsavdaridis, K.D. (2019), "The Evolution of Composite Flooring Systems: Applications, Testing, Modelling and Eurocode Design Approaches," *Journal of Constructional Steel Research,* Vol. 155, pp. 286–300, https://doi.org/10.1016/j.jcsr.2019.01.007.

AISC (1978), *Specification for the Design, Fabrication and Erection of Structural Steel for Buildings*, American Institute of Steel Construction, Chicago, Ill.

AISC (2022a), *Seismic Provisions for Structural Steel Buildings,* ANSI/AISC 341-22, Chicago, Ill.

AISC (2022b), *Specification for Structural Steel Buildings,* ANSI/AISC 360-22, Chicago, Ill.

Al-Majhdowi, A.S. (1975), "Behavior of Composite Shear Connections with and Without Ribbed Metal Deck," Master's Thesis, University of Washington, Seattle, Wash.

Allan, B., Yen, B.T., Slutter, R.G., and Fisher, J.W. (1976), "Comparative Tests on Composite Beams with Formed Metal Deck," Fritz Engineering Laboratory Report No. 200.76.458.1, Lehigh University, Bethlehem, Pa.

An, L. and Cederwall, K. (1996), "Push-out Tests on Studs in High Strength and Normal Strength Concrete," *Journal of Constructional Steel Research,* Vol. 36, No. 1, pp. 15–29.

Baldwin, J.W., Henry, J.R., and Sweeney, G.M. (1965), "Study of Composite Bridge Stringers, Phase II," Report for the Highway Commission of Missouri and U.S. Bureau of Public Roads, University of Missouri, Columbia, Mo.

Bond, R.B., Schafer, B.W., Eatherton, M.R., Easterling, W.S., and Hajjar, J.F., (2022), "Design of Steel Headed Stud Anchors in Concrete-Filled Steel Composite Deck," Report No. NEU-CEE-2021-02, Northeastern University, Department of Civil and Environmental Engineering Reports, Boston, Mass.

Briggs, N.E., Bond, R.B., and Hajjar, J.F. (2022), "Cyclic Behavior of Steel Headed Stud Anchors in Concrete-Filled Steel Deck Diaphragms through Pushout Tests," Report No. NEU-CEE-2021-01, Northeastern University, Department of Civil and Environmental Engineering Reports, Boston, Mass.

Bursi, O.S. and Gramola, G. (1999), "Behaviour of Headed Stud Shear Connectors under Low-Cycle High Amplitude Displacements," *Materials and Structures/Materiaux et Constructions*, Vol. 32, No. 4, pp. 290–297.

Buttry, K.E. (1965), "Behavior of Stud Shear Connectors in Lightweight and Normal-Weight Concrete," Report No. 68-6, Missouri Cooperative Highway Research Program, Missouri State Highway Department and University of Missouri, Columbia, Mo.

Cashell, K. and Baddoo, N. (2014), "Experimental Assessment of Ferritic Stainless Steel," *Composite Construction in Steel and Concrete VII.*

CEN (2004), *Eurocode 4: Design of Composite Steel and Concrete Structures—Part 1-1: General Rules and Rules for Buildings, EN 1994-1-1:2004,* European Committee for Standardization, Brussels, Belgium.

Chapman, J.C. and Balakrishnan, S. (1964), "Experiments on Composite Beams," *The Structural Engineer*, Vol. 42, No. 11, pp. 369–383.

Chinn, J. (1965), "Pushout Tests on Lightweight Composite Slabs," *Engineering Journal*, AISC, Vol. 2, No. 4, pp. 129–134.

CSA (2019), *Design of Steel Structures*, Standard S16:19, Canadian Standards Association, Toronto, Canada.

Dallam, L.N. (1968), "Push-out Tests of Stud and Channel Shear Connectors in Normal-Weight and Lightweight Concrete Slabs," Report No. 68-7, Missouri Cooperative Highway Research Program, Missouri State Highway Department and University of Missouri, Columbia, Mo.

Davies, C. (1967), "Small-Scale Push-out Tests on Welded Stud Shear Connectors," *Concrete*, Vol. 1, No. 9, pp. 311–316.

Easterling, W.S., Gibbings, D.R., and Murray, T.M. (1993), "Strength of Shear Studs in Steel Deck on Composite Beams and Joists," *Engineering Journal*, AISC, Vol. 30, No. 2, pp. 44–54.

Ernst, S. (2006), "Factors Affecting the Behaviour of the Shear Connection of Steel-Concrete Composite Beams," Doctoral Dissertation, Western Sydney University, Sydney, Australia.

Fisher, J.W., Kim, S.W., and Slutter, R.G. (1967), "Tests of Lightweight Concrete Composite Beams and Pushout Specimens with Cellular Steel Deck," Fritz Engineering Laboratory Report No. 200.67.438.1, Lehigh University, Bethlehem, Pa.

Fisher, J.W. (1970), "Design of Composite Beams with Formed Metal Deck," *Engineering Journal*, AISC, Vol. 7, No. 3, pp. 88–96.

Furlong, R.W. and Henderson, W.D. (1975), "Report of Load Tests on Composite Beams of Lightweight Concrete in Three-Inch Metal Deck with Stud Length as the Principle Variable," University of Texas at Austin.

Gibbings, D.R., Easterling, W.S., and Murray, T.M. (1993), "Influence of Steel Deck on Composite Beam Strength," *Composite Construction in Steel and Concrete II*, ASCE, pp. 758–770.

Goble, G.G. (1968), "Shear Strength of Thin Flange Composite Specimens," *Engineering Journal,* Vol. 5, No. 2, pp. 62–65.

Grant, J.A., Fisher, J.W., and Slutter, R.G. (1977), "Composite Beams with Formed Steel Deck," *Engineering Journal*, AISC, Vol. 14, No. 1, pp. 24–43.

Hawkins, N.M. (1971), "The Strength of Stud Shear Connectors," Report No. R141, Department of Civil Engineering, University of Sydney, Sydney, Australia.

Hawkins, N.M. and Mitchell, D. (1984), "Seismic Response of Composite Shear Connections," *Journal of Structural Engineering*, Vol. 110, No. 9, pp. 2120–2136, https://doi.org/10.1061/(ASCE)0733-9445(1984)110:9(2120).

Hicks, S. (2009), "Strength and Ductility of Headed Stud Connectors Welded in Modern Profiled Steel Sheeting," *Structural Engineering International: Journal of the International Association for Bridge and Structural Engineering (IABSE)*, Vol. 19, No. 4, pp. 415–419.

Jayas, B.S. and Hosain, M.U. (1988), "Behaviour of Headed Studs in Composite Beams: Push-Out Tests," *Canadian Journal of Civil Engineering,* Vol. 15, No. 2, pp. 240–253.

Jayas, B.S. and Hosain, M.U. (1989), "Behavior of Headed Studs in Composite Beams: Full-Size Tests," *Canadian Journal of Civil Engineering,* Vol. 16, No. 5, pp. 712–724.

Johnson, R.P. and Yuan, H. (1997), "Resistance of Stud Shear Connectors in Troughs of Profiled Sheeting," Research Report CE 55, February 1997, Department of Civil Engineering, University of Warwick, U.K.

Johnson, R.P. and Yuan, H. (1998a), "Existing Rules and New Tests for Stud Shear Connectors in Troughs of Profiled Sheeting," *Proceedings of the Institution of Civil Engineers: Structures and Buildings*, ICE Publishing Ltd, pp. 244–251.

Johnson, R.P. and Yuan, H. (1998b), "Models and Design Rules for Stud Shear Connectors in Troughs of Profiled Sheeting," *Proceedings of the Institution of Civil Engineers: Structures and Buildings*, ICE Publishing Ltd, pp. 252–263.

Jones, B.T. (1975), "Composite Beam Test '3 + 2' BPTC Technical Data Report No. 75-16," H. H. Robertson Co., Pittsburgh, Pa., September.

Lacap, D.A. (1975), "Composite Beam Tests (W24×61 and W24×55) for Columbia University Life Science Bldg., New York, N.Y., Test Nos. 174-75 and 175-75," Inland-Ryerson Construction Products Co.

Lawson, R.M. (1992), "Shear Connection in Composite Beams," *Composite Construction in Steel and Concrete II*, pp. 81–97.

Lawson, R.M., Aggelopoulos, E., Obiala, R., Hanus, F., Odenbreit, C., Nellinger, S., Kuhlmann, U., Eggert, F., Lam, D., Dai, X., and Sheehan, T. (2017), "Development of Improved Shear Connection Rules in Composite Beams (DISCCO)," Final Report, Directorate-General for Research and Innovation, Publications Office of the European Union, Luxembourg.

Lim, O.K., Lam, D., Dai, X., and others (2020), "Fire Performance of Headed Shear Studs in Profiled Steel Sheeting," *Journal of Constructional Steel Research,* Vol. 164, 105791, https://doi.org/10.1016/j.jcsr.2019.105791.

Lloyd, R.M. and Wright, H.D. (1990), "Shear Connection between Composite Slabs and Steel Beams," *Journal of Constructional Steel Research,* Vol. 15, No. 4, pp. 255–285.

Lyons, J.C., Easterling, W.S., and Murray, T.M. (1994), "Strength of Welded Shear Studs, Vols. I and II," Report CE/VPI-ST 94/07, Virginia Polytechnic Institute and State University, Blacksburg, Va.

Mainstone, R.J. and Menzies, J.B. (1967), "Shear Connectors in Steel-Concrete Composite Beams for Bridges. I. Static and Fatigue Tests on Push-out Specimens," *Concrete*, Vol. 1, No. 9, pp. 291–302.

Menzies, J.B. (1971), "CP 117 and Shear Connectors in Steel-Concrete Composite Beams Made with Normal-Density or Lightweight Concrete," *The Structural Engineer*, Vol. 49, No. 3, pp. 137–154.

Mottram, J.T. and Johnson, R.P. (1990), "Push Tests on Studs Welded through Profiled Steel Sheeting," *The Structural Engineer*, Vol. 68, No. 10, pp. 187–193.

Nellinger, S. (2015), "On the Behaviour of Shear Stud Connections in Composite Beams with Deep Decking," Doctoral Dissertation, University of Luxembourg.

Oehlers, D.J. and Johnson, R.P. (1981), "The Splitting Strength of Concrete Prisms Subjected to Surface Strip or Patch Loads," *Magazine of Concrete Research*, Vol. 33, No. 116, pp. 171–179.

Ollgaard, J.G., Slutter, R.G., and Fisher, J.W. (1971), "Shear Strength of Stud Connectors in Lightweight and Normalweight Concrete," *Engineering Journal*, AISC, Vol. 8, No. 2, pp. 55–64.

Pallarés, L. and Hajjar, J.F. (2010), "Headed Steel Stud Anchors in Composite Structures, Part I: Shear," *Journal of Constructional Steel Research*, Vol. 66, No. 2, pp. 198–212.

Rambo-Roddenberry, M., Easterling, W.S., and Murray, T.M. (2002a), "Behavior and Strength of Welded Stud Shear Connectors-Data Report," Report No. CE/VPI–ST 02/05, Virginia Polytechnic Institute and State University, Blacksburg, Va.

Rambo-Roddenberry, M., Easterling, W.S., and Murray, T.M. (2002b), "Behavior and Strength of Welded Stud Shear Connectors," Report No. CE/VPI-ST 02/04, Virginia Polytechnic Institute and State University, Blacksburg, Va.

Robinson, H. and Wallace, I.W. (1971), "Composite Beams with Partial Connection," Meeting Preprint No. 1549, ASCE Annual and National Environmental Engineering Meeting, St. Louis, Mo., October 18–22.

Robinson, H. (1988), "Multiple Stud Shear Connections in Deep Ribbed Metal Deck," *Canadian Journal of Civil Engineering*, Vol. 15, No. 4, pp. 553–569.

Russell, M.J., Clifton, G.C., and Lim, J.B.P. (2021), "Vertical and Horizontal Push Tests on Specimens with a Trefoil Decking Profile," *Structures*, Vol. 29, pp. 1096–1110, https://doi.org/10.1016/j.istruc.2020.11.064.

Sanden, P. van der (1996), "The Behaviour of a Headed Stud Connection in a 'New' Push Test Including a Ribbed Slab," BKO-Report 95-16, Technische Universiteit Eindhoven.

Seek, W.G., Fisher, J.W., and Slutter, R.G. (1970), "Tests of Lightweight Composite Beams with Metal Decking," Fritz Engineering Laboratory Report No. 200.70.458.1, Lehigh University, Bethlehem, Pa.

Shaikh, A.F. and Yi, W. (1985), "In-Place Strength of Welded Headed Studs," *PCI Journal,* Vol. 30, No. 2, pp. 56–81.

Shim, C.S., Lee, P.G., and Yoon, T.Y. (2004), "Static Behavior of Large Stud Shear Connectors," *Engineering Structures,* Vol. 26, 12, pp. 1853–1860.

Shoup, T.E. and Singleton, R.C. (1963), "Headed Concrete Anchors," *Journal of the American Concrete Institute,* Vol. 60, No. 9, pp. 1229–1235.

Slutter, R.G. and Driscoll, G.C., Jr. (1963), "The Flexural Strength of Steel and Concrete Composite Beams," Fritz Laboratory Report No. 279.15, Department of Civil and Environmental Engineering, Lehigh University, Bethlehem, Pa.

Smith, A.L. and Couchman, G.H. (2010), "Strength and Ductility of Headed Stud Shear Connectors in Profiled Steel Sheeting," *Journal of Constructional Steel Research,* Vol. 66, No. 6, pp. 748–754, http://dx.doi.org/10.1016/j.jcsr.2010.01.005.

Steele, D.H. (1967), "The Use of Nelson Studs with Lightweight Aggregate Concrete in Composite Construction," M.S. Thesis, University of Colorado, Boulder, Colo.

Sublett, C.N., Easterling, W.S., and Murray, T.M. (1992), "Strength of Welded Headed Studs in Ribbed Metal Deck on Composite Joist," Report No. CE/VPI-ST 92/03, Virginia Polytechnic Institute and State University, Blacksburg, Va.

Viest, I.M. (1956), "Investigation of Stud Shear Connectors for Composite Concrete and Steel T-Beams," *ACI Journal Proceedings,* Vol. 52, No. 4.

Vigneri, V. (2021), "Load Bearing Mechanisms of Headed Stud Shear Connection in Profiled Steel Sheeting Transverse to the Beam," Doctoral Dissertation, University of Luxembourg.

Vigneri, V., Hicks, S.J., Taras, A., and Odenbreit, C. (2022), "Design Models for Predicting the Resistance of Headed Studs in Profiled Sheeting," *Steel and Composite Structures,* Vol. 42, No. 5, pp. 633–647.

Zandonini, R. and Bursi, O.S. (2000), "Cyclic Behavior of Headed Stud Shear Connectors," *Proceedings of the Conference: Composite Construction in Steel and Concrete IV*, pp. 470–482.

Zhai, C., Ding, Y., Ma, H., and others (2018), "Experimental Study on Shear Behavior of Studs under Monotonic and Cyclic Loadings," *Journal of Constructional Steel Research,* Vol. 151, pp. 1–11, https://doi.org/10.1016/j.jcsr.2018.07.029.

Lateral Force Distributions in Multistory Braced-Moment Frames

RALPH M. RICHARD, ERIC KELDRAUK, and JAY ALLEN

ABSTRACT

Braced frames traditionally have been analyzed and designed as trusses with all joints modeled as pins, such that only the braces provide lateral force resistance. However, frames with gusset plate connections create a rigid joint zone between frame beams and columns, effectively resulting in moment frame behavior, particularly at larger drift angles when the braces have yielded or buckled. Described herein is a rationale for multistory braced-moment frames that includes the frame's moment resistance to lateral displacements when subjected to story-drift angles where the lateral resistance of the frame comprises both brace and moment frame action.

Keywords: braced-moment frame, lateral force distribution.

INTRODUCTION

Braced frames are typically modeled and designed as pinned connected truss members, wherein all lateral resistance is provided by the braces (Muir and Thornton, 2014). The design of the gusset plates is subsequently based upon only the transfer of the brace forces to the pin-connected beams and columns. This design rationale has proven acceptable for story-drift angles at and below that which induces yielding in the braces. However, at story-drift angles of approximately 0.0025 (1/400) rad, the braces yield, as shown in the single-story frame pushover analysis in Figure 1, and additional lateral displacement is resisted by moment frame action (Walters et al., 2002). Designers of braced frames often ignore the frame action or mitigate it by introducing simple or semi-rigid connections in the braced frame, as discussed in the AISC *Seismic Provisions* Commentary Section F2.6b (2016b). Described herein is a design rationale for mutistory buckling restrained braced frames (BRBF) that includes the moment frame action of the braced frame to lateral loads after the braces have yielded (Richard et al., 2024).

Shown in Figure 2 is a single-story, braced-moment frame (a) modeled for analysis of the lateral force distribution as a combination of the force distributions in a braced frame (b) and a moment frame (c). The force distributions in Figures 2(b) and (c) are based upon a frame drift angle that results in the yielding of the braces in Figure 2(b) and inelastic action in the top and bottom beams in Figure 2(c), based on strong column-weak beam frame design (Richard et al., 2024). Beam plastic hinges as shown are located at the ends of the gusset plates as shown by both test and analyses (Lopez et al., 2002, 2004; Richard et al., 2017).

ANALYSIS OF MULTISTORY BRACED-MOMENT FRAMES

Shown in Figure 3 is a four-story braced frame with all gusset plate connections replaced with pins for analysis (Uniform Force Method). This truss model disregards the moment frame resistance after the braces yield shown in Figure 1.

Figure 4 depicts a virtual lateral displacement for this frame with plastic hinges located in the beams for strong column-weak beam design.

Lateral force distributions in multistory braced frames are analyzed herein using the single-story rational applied to each story as shown in Figures 2(b) and (c) (Richard et al., 2024). As shown in Figure 4, the virtual lateral frame displacement where the columns remain straight is based upon a strong column-weak beam frame design with two plastic beam hinges for each story. For each story, the moment frame shear, V_m, is determined using the virtual work equation where external work (EW) is equal to the internal work (IW). For a story drift, Δ, a story moment frame shear, V_m, a beam moment, M_b, and two beam hinge rotations θ_{hinge}, the virtual work equation is:

$$V_m \Delta = 2 M_b \theta_{hinge} \quad (1)$$

Ralph M. Richard, Professor Emeritus, University of Arizona, Tucson, Ariz. Email: ralph@u.arizona.edu (corresponding)

Eric Keldrauk, Structural Engineer Analyst, Schuff Company, Phoenix, Ariz. Email: eric.keldrauk@gmail.com

Jay Allen, Executive VP of Engineering, Schuff Company, Phoenix, Ariz. Email: jayallense@yahoo.com

Paper No. 2024-17R

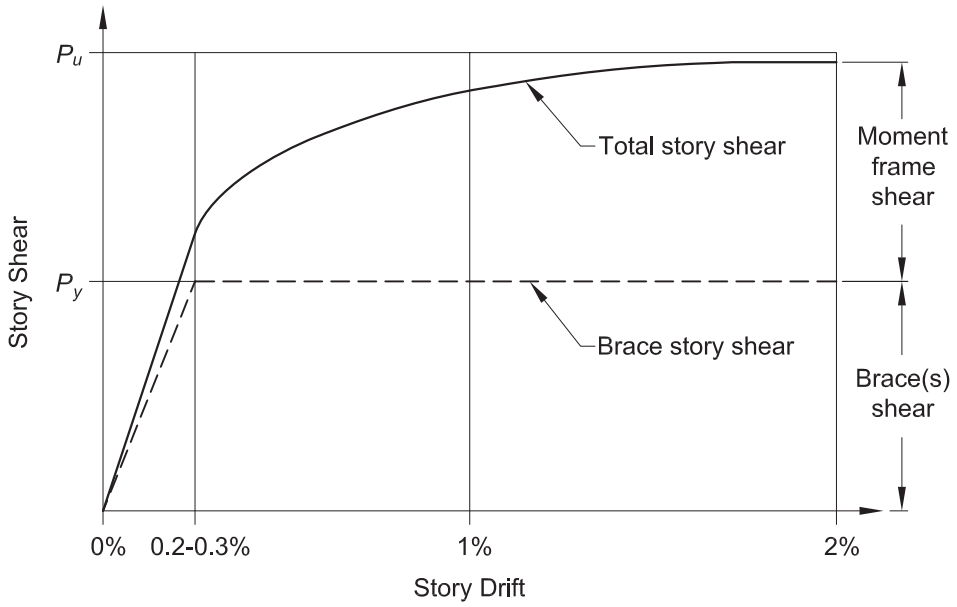

Fig. 1. Typical story shear distribution in a braced frame pushover analysis.

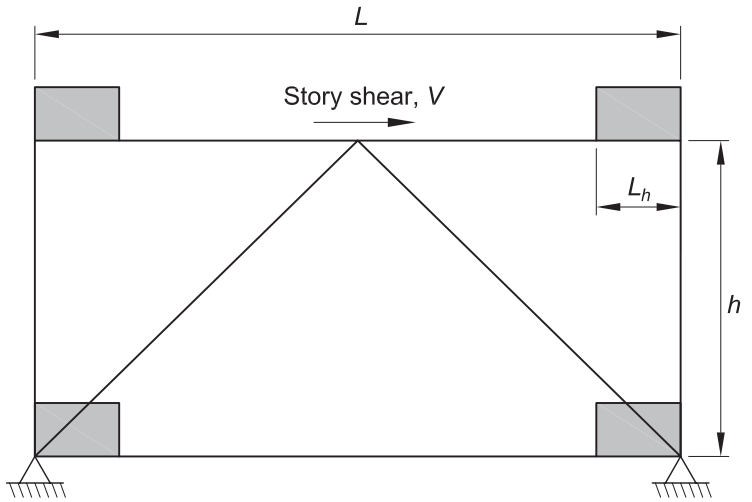

(a) Braced-moment frame

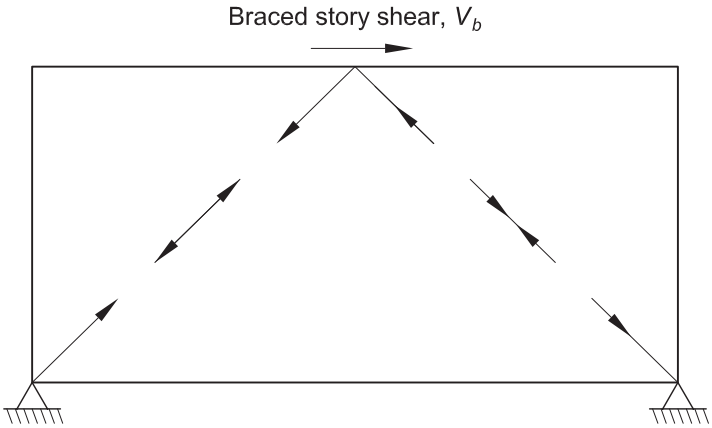

(b) Braced frame

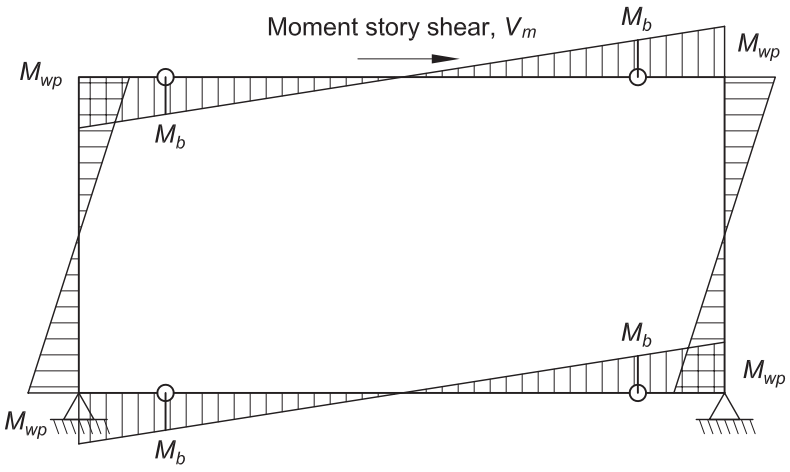

(c) Moment frame force distributions

Fig. 2. Single-story frame.

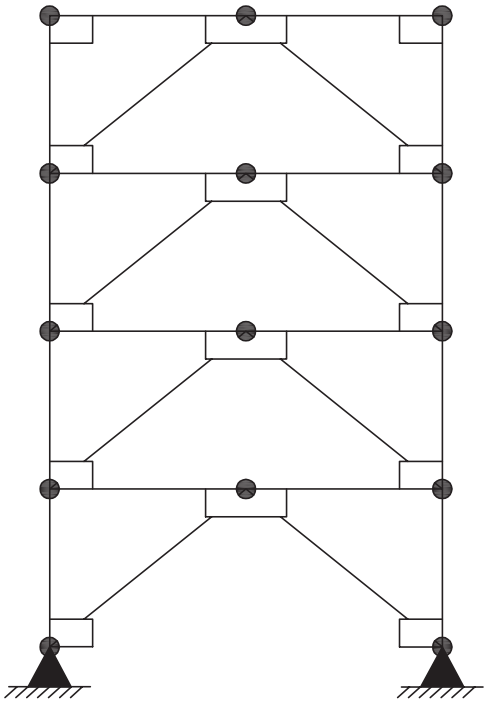

Fig. 3. Braced-moment frame with UFM pin connections.

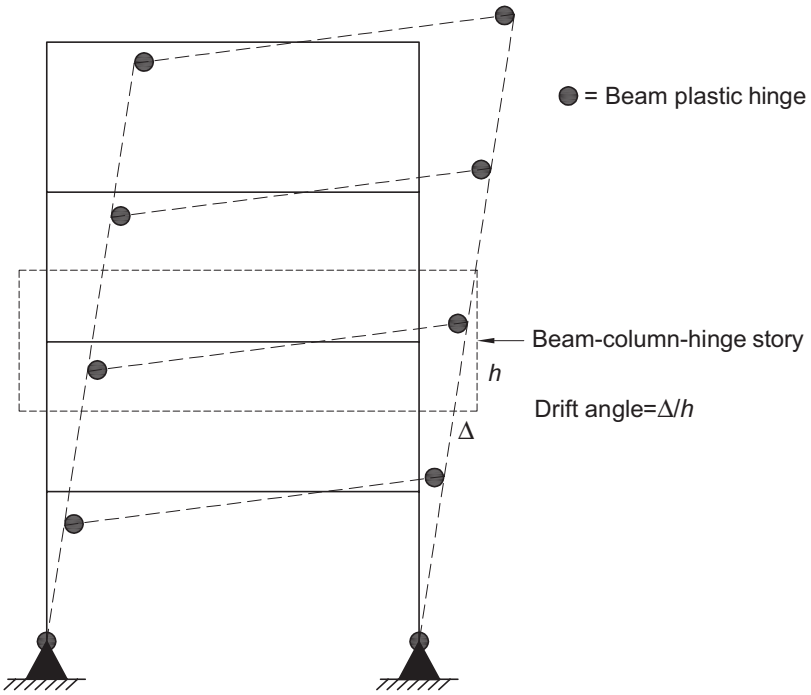

Fig. 4. Moment frame beam plastic hinge locations.

The plastic hinge rotation in terms of the story drift angle, θ, is:

$$\theta_{hinge} = \theta k_1 = \frac{\Delta k_1}{h} \quad (2)$$

where the constant k_1 is defined in Appendix A and h is the story height.

The beam hinge plastic moment, M_b, is determined as follows:

$$M_b = M_u k_2 \quad (3)$$

where k_2 is a material term that adjusts the pure bending plastic hinge moment, M_u, to account for axial-moment interaction. The derivations of k_1 and k_2 are presented in the appendix of this paper. Substituting Equation 2 and Equation 3 into Equation 1 gives the story shear for the moment story frame in Figure 2(c).

$$V_m = \frac{2M_u k_1 k_2}{h} \quad (4)$$

In Figure 4 with the moment frame story shear, V_m, known, the brace frame story shear, V_b, is determined as:

$$V_b = V - V_m \quad (5)$$

where V is the frame story shear. The design of the braces is based upon their expected yield stress. This rationale provides the forces in the braces, beams, and columns to design the gusset plates based upon a braced-moment frame force distribution.

DESIGN EXAMPLE—BRACED-MOMENT FRAME ANALYSIS

Given:

Analyze the single-bay, four-story braced frame shown in Figure 5. The beam, column, and gusset plate material is ASTM A992/A992M (2022) (F_y = 50 ksi). The frame bay width is 30 ft and the story height is 15 ft. Gusset plates are 24 in. × 24 in. The force distributions shown use the equivalent lateral force method given in ASCE/SEI 7 (2016) with a base seismic shear of 600 kips. (Frame design with grade beam is optional.)

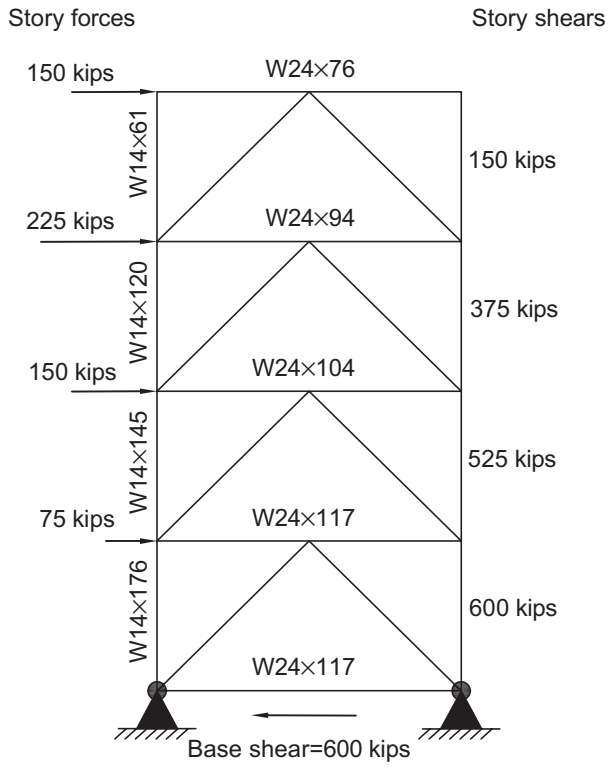

Fig. 5. Four-story braced-moment frame.

Table 1. Four-Story Frame Data												
Story	V_s (kips)	P_b (kips)	P_y (kips)	P_b/P_y	k_2	k_1	M_u (kip-in.)	V_m (kips)	V_m/V_s	V_t (kips)	V_t/V_s	Beam
4	150	75	1120	0.062	0.97	1.15	10000	124	0.83	26	0.17	W24×76
3	375	188	1385	0.125	0.94	1.15	12700	165	0.44	210	0.56	W24×94
2	525	263	1535	0.158	0.92	1.15	14450	170	0.32	355	0.68	W24×104
1	600	300	1720	0.161	0.92	1.15	17658	206	0.34	394	0.66	W24×117
0	600				1.00	1.15	16350					W24×117

Table 2. Four-Story Frame with Modified Beam Design Data												
Story	V_s (kips)	P_b (kips)	P_y (kips)	P_b/P_y	k_2	k_1	M_u (kip-in.)	V_m (kips)	V_m/V_s	V_t (kips)	V_t/V_s	Beam
4	150	75	1120	0.067	0.97	1.15	10000	124	0.83	26	0.17	W24×76
3	375	188	1120	0.167	0.92	1.15	10000	116	0.31	255	0.69	W24×76
2	525	263	1120	0.234	0.88	1.15	10000	112	0.21	413	0.78	W24×76
1	600	300	1120	0.267	0.86	1.15	10000	110	0.18	490	0.81	W24×76
0	600				1.00	1.15	10000					W24×76

Solution:

The frame is analyzed as shown in Tables 1 and 2.

where

M_u = beam plastic moment
P_b = beam axial load
P_y = beam axial yield load
V_m = story moment frame shear
$= 2M_u k_1 k_2/h$
V_s = story shear
V_t = story brace frame shear
h = story height
= 180 in.

For k_1 and k_2, refer to the Appendix or Richard et al. (2024), and the AISC *Specification* (2016a).

For this frame design, the story braces resist 17%, 56%, 68%, and 66% of the story shear forces. If all the beams are replaced with more flexible W24×76 beams, the story brace forces are 17%, 69%, 78%, and 81% of the story shear forces, as shown in Table 2.

For comparison, The UFM rationale assigns all the story shear to the braces so that the ratio V_t/V_s would be equal to 1.00 for all stories.

Table 3. Beam Designs for the Four-Story Frame												
Story	V_s (kips)	$0.5V_s$ (kips)	M_u (kip-in.)	$Z_{req'd}$ (in.^{3})	Beam Selected	Z Beam (in.^{3})	P_b (kips)	P_y (kips)	P_b/P_y	k_2	k_2k_1	
4	150	75	6750	135	W24×55	134	37.5	810	0.046	0.98	1.13	ok
3	375	187	16830	336	W24×117	327	93.5	1720	0.054	0.98	1.13	ok
2	525	262	23580	472	W24×146	418	131	2150	0.061	0.96	1.10	ok
1	600	300	27000	540	W24×176	511	150	2585	0.058	0.97	1.11	ok
0	600	300	27000	540	W24×176	511	150	2585	0.058	0.97	1.11	ok

REDESIGN OF MULTISTORY BRACED-MOMENT FRAMES

Using the braced-moment frame in Figure 5, redesign this frame so that the braces and moment frame each resist approximately 50% of the story shears. In the iterative design procedure for the redesign, make the following approximations for all stories: estimate $k_1 = 1.15$ and $k_1k_2 = 1.0$ so that the beams meet both strength (k_2) and stiffness (k_1) requirements. Specify an acceptable design criterion for k_1k_2. Estimate the plastic moment in the beam.

$$M_u = h_x V_m / 2 \tag{6}$$

where h is the story height and V_m is moment frame shear. Compute the beam plastic modulus required to select the beams for redesign.

$$Z_{req'd} = M_u / F_y \tag{7}$$

Shown in Table 3 are the selected beam designs using this rationale and where a selected design criterion $k_1k_2 \leq 1.15$ is satisfied for all the selected beams.

With the schedule of beams shown in Table 3, the moment frames resist approximately 50% of the story shears. Design the braces to resist 50% of the story shear. With this schedule of beams, the potentially large shear forces in the beams in the connection region of chevron-braced frames are reduced by approximately 50% (Sabelli and Bolin, 2021, 2022). The design rationale shown here results in a significant reduction in the forces and weights of the frame braces by including the moment resistance of the frame. When frames are designed using loads determined herein, the dual system provisions of SEI/ASCE 7 should be satisfied.

SUMMARY

A chevron frame analysis and design rationale for multistory buckling restrained braced frames that includes the inherent moment frame forces when the frame is subjected to seismic or wind forces that result in inelastic frame displacements is presented herein. The evaluation of the distribution of the story shears between the braces and the moment frame is made using conventional plastic analysis of the moment frame. This rationale includes the moment frame action and may be used to optimize story shear distributions between the frame braces and the moment frame as shown in the design example. The design methodology of AISC Design Guide 29 (Muir and Thornton, 2014) wherein all the story shear is resisted by the braces is applicable for elastic frame response.

REFERENCES

AISC (2016a), *Specification for Structural Steel Buildings*, ANSI/AISC 360-16, American Institute of Steel Construction, Chicago, Ill.

AISC (2016b), *Seismic Provisions for Structural Steel Buildings*, ANSI/AISC 341-16, American Institute of Steel Construction, Chicago, Ill.

ASCE (2016), *Minimum Design Loads and Associated Criteria for Buildings and Other Structures*, SEI/ASCE 7-16, American Society of Civil Engineers, Reston, Va.

ASTM (2022), *Standard Specification for Structural Steel Shapes*, ASTM A992/A992M, ASTM International, West Conshohocken, Pa.

Lopez, W.A., Gwie, D.S., Saunders, C.M., and Lauck, T.W. (2002), "Lessons Learned from Large-Scale Tests of Unbonded Braced Frame Subassemblies," *Proceedings of the Structural Engineers Association of California 2002 Convention.*

Lopez, W.A., Gwie, D.S., Saunders, C.M., and Lauck, T.W. (2004), "Structural Design and Experimental Verification of a Buckling-Restrained Braced Frame System," *Engineering Journal*, AISC, Vol. 41, No. 4, pp. 77–86.

Muir, L.S. and Thornton, W.A. (2014), *Vertical Bracing Connections—Analysis and Design*, Design Guide 29, AISC, Chicago, Ill.

Richard, R.M., Keldrauk, E., and Allen, J. (2024), "Lateral Force Distributions in Braced-Moment Frames," *Engineering Journal*, AISC, Vol. 61, No.2, pp. 59–70.

Richard, R.M., Radau, R.E., and Allen, J. (2017), "Damage Tolerant Braced Frame Designs," *Proceedings of the Structural Engineers Association of California 2017 Convention*.

Sabelli, R. and Bolin, E. (2021), "Design for Member Local Member Shear at Brace Connections: Full Height and Chevron Gussets," *Engineering Journal*, AISC, Vol. 58, No. 1, pp. 45–78.

Sabelli, R. and Bolin, E., (2022), "The Chevron Effect: Reserve Strength of Existing Chevron Frames," *Engineering Journal,* AISC, Vol. 53, No. 3, pp. 209–224.

Walters, M.T., Maxwell, B.H., and Berkowitz, R.A. (2002), "Design for Improved Performance of Buckling-Restrained Braced Frames," *Proceedings of the Structural Engineers Association of California 2002 Convention,* pp. 507–513.

APPENDIX

Derivation of k_1

Figure A-1 depicts a magnified view of the plastic hinge rotation. The offset hinge rotation, θ_h, is calculated as:

$$\begin{aligned}\theta_h &= \theta + \frac{2\theta L_h}{L-2L_h}\\ &= \theta\left(1+\frac{2L_h}{L-2L_h}\right)\\ &= \theta k_1\end{aligned}$$

where L_h is the hinge offset and L is the length of the beam. k_1 is then determined as:

$$\begin{aligned}k_1 &= 1+\frac{2L_h}{L-2L_h}\\ &= \frac{L}{L-2L_h}\end{aligned}$$

Derivation of k_2

The beam plastic moment, M_p, is evaluated using the beam-column interaction equations given in AISC *Specification* Section H1 (2016a). Assuming the beams (with gross area, A_b, and strong axis plastic modulus, Z_b) are in uniaxial bending, the moment capacity for a given axial load, P, is found by rearranging the equations as shown:

$$k_2 = \frac{M_p}{M_u} = \begin{cases}\dfrac{9}{8}\left(1-\dfrac{P}{P_y}\right) & \text{for } \dfrac{P}{P_y} \geq 0.2\\ 1-\dfrac{P}{2P_y} & \text{for } \dfrac{P}{P_y} < 0.2\end{cases}$$

where

$$P_y = F_y A_b \text{ and } M_u = F_y Z_x$$

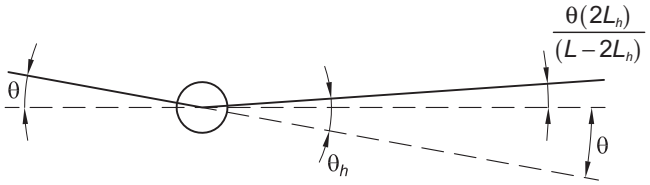

Fig. A-1. Magnified view of plastic hinge rotation.

Tensile Rupture of Rectangular Hollow Section Flexural Members with Holes In the Tension Flange

BRENDAN RICHARDS and KYLE TOUSIGNANT

ABSTRACT

An evaluation of the AISC *Specification* Section F13.1 provisions for the reduction in strength of beams and girders with holes in the tension flange is performed. Twelve simply supported rectangular hollow section (RHS)-to-RHS splice connections with variations in RHS shape, number of bolts, and bolting arrangement are tested under monotonic four-point bending, and net-section rupture (in the tension flange) is achieved. The results demonstrate that, for RHS members, the current AISC *Specification* Section F13.1 provisions are vastly conservative. The current results are combined with the previous data from 138 tests on wide-flange girders with holes in the tension flange, and a new nominal flexural strength (M_n) equation is developed using net section properties. The new equation is shown to increase the accuracy of M_n predictions and reduce scatter in the predicted results. A reliability analysis is performed to demonstrate that the new approach provides acceptable levels of reliability when compared to the target reliability index of 4.0 specified in Chapter B of the *Specification* commentary.

KEYWORDS: rectangular hollow sections, flexural members, beams, girders, tensile rupture, bolts.

INTRODUCTION

The current expression in AISC *Specification for Structural Steel Buildings* Section F13.1 (2022a), hereafter referred to as the AISC *Specification*, for the nominal flexural strength, M_n, of members (i.e., beams and girders) with holes in the tension flange covers rolled or built-up shapes and cover-plated beams with holes, proportioned on the basis of flexural strength of the gross section. According to this section, M_n—for the limit state of tensile rupture of the tension flange—is calculated when

$$F_u A_{fn} < Y_t F_y A_{fg} \tag{1}$$

in which case,

$$M_n = \frac{F_u A_{fn}}{A_{fg}} S_x \tag{2}$$

where F_u and F_y are the specified minimum tensile and yield strengths, respectively, given in Table 2-4 of the AISC *Steel Construction Manual* (2023); A_{fn} and A_{fg} are the net and gross area of the tension flange, respectively; S_x is the minimum elastic section modulus taken about the x-axis; and $Y_t = 1.0$ for $F_y/F_u \le 0.8$ and 1.1 otherwise. When Equation 1 is not met—that is, when $Y_t F_y A_{fg} \le F_u A_{fn}$—the limit state of rupture does not apply.

Equation 2 reduces the flexural strength of the cross section as a function of A_{fn}/A_{fg} to provide an acceptable margin of safety against rupture of the tension flange; however, its predictions are well-known to be conservative for plastic design/compact sections (which, in the absence of holes, can develop the plastic moment, M_p). With an interest in developing field-bolted connections for hollow structural sections (HSS) members, the over-conservatism of AISC *Specification* Section F13.1—for all members—is a salient issue.

AISC *Specification* Section F13.1 was developed from experiments on W-shape and T-shaped cross sections (Dexter and Altstadt, 2004; Yuan et al., 2004), with scant research done to assess its overall reliability and applicability to other cross-sectional shapes. This study addresses that gap by evaluating Section F13.1 in a probabilistic manner, in relation to rectangular hollow section (RHS) members with holes in the tension flange. The design of these connections—namely, RHS-to-RHS bolted splice connections for flexure—is required by the AISC *Seismic Provisions for Structural Steel Buildings* (2022b) for (beam-)columns in intermediate moment frames (IMFs), special moment frames (SMFs), and special truss moment frames (STMFs).

This paper presents an experimental program to assess the applicability of AISC *Specification* Section F13.1 (2022a) to RHS-to-RHS bolted splice connections, a comparison(s) of the results to those from 138 previous numerical and experimental tests on W-shaped cross sections, and a reliability assessment. The results of this research support a recommendation to modify the provision to improve its accuracy and economy.

Brendan Richards, Ph.D. Candidate, Department of Civil & Resource Engineering, Dalhousie University, Halifax, NS, Canada.
Email: brendan.richards@dal.ca

Kyle Tousignant, Associate Professor, Department of Civil & Resource Engineering, Dalhousie University, Halifax, NS, Canada.
Email: kyle.tousignant@dal.ca (corresponding)

Paper No. 2025-03R

Table 1. RHS and Plate Dimensions and Properties										
	RHS							Plate(s)		
No.	Shape	H (in.)	B (in.)	t_{des} (in.)	A_{fg}* (in.^{2})	S_x (in.^{3})	Z_x (in.^{3})	Dimensions	B_p (in.)	t_p (in.)
1	6×6×¼	6.00	6.00	0.233	1.18	9.52	11.2	4⅞×⅞	4.88	0.88
2	7×7×¼	7.00	7.00	0.233	1.41	13.3	15.5	5⅞×¾	5.88	0.75
3	7×7×¼	7.00	7.00	0.233	1.41	13.3	15.5	5⅞×¾	5.88	0.75
4	8×8×½	8.00	8.00	0.465	2.86	31.2	37.5	5¾×1⅝	5.75	1.63
5	8×8×⅝	8.00	8.00	0.581	3.30	36.5	44.7	5^3⁄$_{16}$×⅞	5.19	0.88
6	8×8×⅝	8.00	8.00	0.581	3.30	36.5	44.7	5^3⁄$_{16}$×⅞	5.19	0.88
7	10×8×½	10.00	8.00	0.465	2.86	42.7	51.9	5¾×1⅞	5.75	1.88
8	12×6×¼	12.00	6.00	0.233	1.18	25.2	31.1	4⅞×1⅜	4.88	1.38
9	12×8×⅜	12.00	8.00	0.349	2.30	43.7	52.9	6^5⁄$_{16}$×1⅝	6.31	1.63
10	12×8×⅜	12.00	8.00	0.349	2.30	43.7	52.9	6^5⁄$_{16}$×1¾	6.31	1.75
11	7×5×⅜	7.00	5.00	0.349	1.26	14.1	17.5	3^5⁄$_{16}$×1¾	3.31	1.75
12	7×5×⅜	7.00	5.00	0.349	1.26	14.1	17.5	3^5⁄$_{16}$×1¾	3.31	1.75

* Note: Determined in accordance with AISC *Specification* using $A_{fg} = (B - 4t_{des})t_{des}$.

Table 2. Bolt Nominal Properties									
No.	Size	Grade	n_b	n_r	d (in.)	d_h (in.)	s (in.)	g (in.)	l_c (in.)
1	¾×2¾	A490	24	2	0.750	0.813	3.38	2.00	3.38
2	¾×2¾	A490	32	1	0.750	0.813	3.00	—	3.00
3	⅞×2¾	A490	28	1	0.875	0.938	3.00	—	3.00
4	⅞×3¾	A490	40	1	0.875	0.938	3.00	—	3.00
5	⅞×3	A325	24	1	0.875	0.938	3.00	—	3.00
6	¾×3¼	A490	32	1	0.750	0.813	3.00	—	3.00
7	⅞×4	A490	44	1	0.875	0.938	3.00	—	3.00
8	¾×3	A490	40	2	0.750	0.813	3.50	2.00	3.50
9	¾×3¾	A325	64	2	0.750	0.813	3.00	3.00	3.00
10	1×4	A325	40	2	1.000	1.063	4.00	3.00	4.00
11	⅞×3¼	A490	24	1	0.875	0.938	3.00	—	3.00
12	¾×3¼	A325	32	1	0.750	0.813	3.00	—	3.00

SCOPE OF TESTING

Overview of Connections

For the current study, 12 RHS-to-RHS bolted splice connections comprised of two RHS members, finished to bear and bolted together by means of internal splice plates, were designed to fail by rupture of the tension flange under strong-axis bending. The 12 connections were designed with varying ratios of A_{fn}/A_{fg} and S_x and, as a result, varied the net elastic section modulus taken about the axis of bending, the plastic section modulus taken about the x-axis, and the net plastic section modulus taken about the axis of bending (S_n, Z_x, and Z_n, respectively). These variations were achieved by using RHS members with different shapes and connections with different numbers of bolts, bolt sizes, and bolt arrangements, within the limits outlined in AISC *Specification* Sections J3.3 and J3.4. Table 1 summarizes the RHS shapes for each connection and provides nominal values of the members' overall height, H; overall width, B; design wall thickness, t_{des} (= $0.93t_{nom}$, where t_{nom} = nominal wall thickness); and gross-section properties, A_{fg}, S_x, and Z_x. The splice-plate cross-sectional dimensions, including width, B_p, and thickness, t_p, are also given. Table 2 provides the bolt designations (i.e., $d \times l_{bolt}$, where d is the nominal diameter of the fastener and l_{bolt} is the nominal bolt

length); bolt grades; total number of bolts per connection, n_b; number of bolts per row, n_r; diameter of the bolt hole, d_h; longitudinal center-to-center spacing (pitch) of two consecutive bolt holes, s; transverse center-to-center spacing (gage) between fastener gage lines, g; and clear distance, in the direction of the force, between the edge of the hole and the edge of the material, l_c, for each connection. A detail/schematic of a typical test connection is also presented, in Figure 1, where A_{net} is the net-effective area subjected to tension under pure flexure, shown shaded in Figure 1(a).

The RHS members were dual certified to ASTM A500 Grade B and C with a minimum F_y = 50 ksi and a minimum F_u = 62 ksi (AISC, 2022a; ASTM, 2021). The internal splice plates conformed to CAN/CSA-G40.20/G40.21 Grade 350W with a minimum F_y = 51 ksi and a minimum F_u = 65 ksi (AISC, 2022a; CSA, 2023). As shown in Table 2, the bolts conformed to ASTM F3125/F3125M Grade A325 or Grade A490 with nominal shear stress, F_{nv}, of 68 ksi or 84 ksi, respectively, with threads excluded from the shear plane (AISC, 2022a; ASTM, 2023). All bolts were installed in drilled holes with $d_h = d + 1/16$ in.

Design Process for Rupture-Critical Tests

To ensure that rupture of the RHS tension flange governed the connection strength, the other possible limit states for the RHS (i.e., gross-section yielding and block shear), splice plates (tensile rupture, plate buckling and block shear), and bolts (bearing, tear-out, and shear), were designed to have an axial resistance equal to or greater than a force resulting from bending of $A_{net}F_u$.

For Specimens 5 and 6 (which utilized HSS 8×8×⅝ members), the geometric limitations and necessary bolt configurations precluded this design approach, so an alternative method was used. In these cases, the connections were designed so that all other limit state capacities exceeded a force from bending of $1.15A_{fg}F_y$. This was justified by 138 past experimental and numerical tests on W-shape sections that failed by tensile rupture of the tension flange in which the ultimate bending moments were 12% greater, on average, than the nominal plastic bending moment resistance of the gross section(s).

Because test specimens were designed to fail by rupture of the tension flange (of the RHS), tensile coupon (TC) tests were conducted on the RHS material(s). For each heat of material, three TCs taken from mid-width of the RHS flats (excluding the face with the weld seam) were tested in accordance with ASTM E8/E8M-22 (ASTM, 2022). Table 3 summarizes the average results of the tests for each member, including the modulus of elasticity, E; measured values of F_y and F_u; and the yield, ultimate, and rupture strains (ε_y, ε_u, and ε_r, respectively).

The geometric properties of the RHS (i.e., H, B, and t, where t is the measured wall thickness) were also measured, and the gross-section properties (i.e., A_{fg}, S_x, and Z_x) were recomputed assuming an outside corner radius of 2.0t (AISC, 2022a). The measured geometric properties of the RHS and calculated gross section properties are shown in Table 4.

To facilitate tensile rupture of the tension flange of the RHS, portions of members outside the connection region (i.e., beyond the ends of the splice plates) were reinforced using material taken from the elastic shear spans of previously tested specimens. The reinforcement was applied to the compression flange and part of each web, as shown in Figure 2 (where B_s is the stiffener plate overall width, H_s is the stiffener plate overall height, t_s is the stiffener plate thickness, and A_{gc} is the gross area subjected to compression, shown shaded). The measured geometric properties of

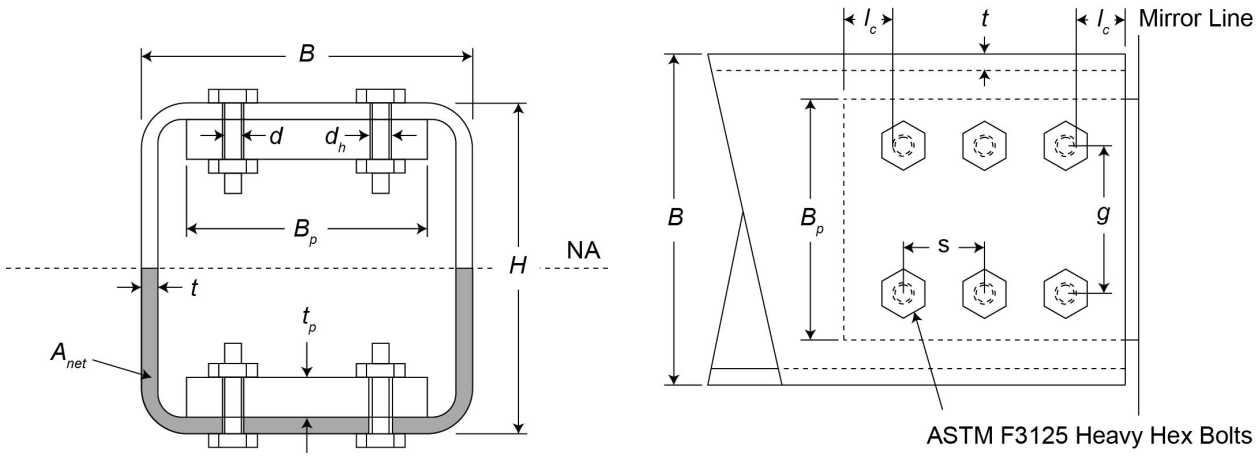

(a) Cross section *(b) Plan view*

Fig. 1. Test connection schematic.

Table 3. Measured RHS Material Properties							
No.	Shape	E (ksi)	F_y (ksi)	F_u (ksi)	ε_y%	ε_u%	ε_r%
1	6×6×¼	32457	56.2	71.8	0.351	16.3	29.1
2	7×7×¼	32192	63.2	75.2	0.359	14.4	26.9
3	7×7×¼	32192	63.2	75.2	0.359	14.4	26.9
4	8×8×½	28326	50.7	66.3	0.366	14.3	29.4
5	8×8×⅝	29117	60.9	72.1	0.378	10.6	28.8
6	8×8×⅝	29117	60.9	72.1	0.378	10.6	28.8
7	10×8×½	31141	50.7	68.4	0.356	14.5	31.2
8	12×6×¼	28853	56.5	72.0	0.366	15.2	25.7
9	12×8×⅜	32764	62.2	75.6	0.354	13.1	28.9
10	12×8×⅜	32764	62.2	75.6	0.354	13.1	28.9
11	7×5×⅜	27984	60.9	73.2	0.413	12.1	29.1
12	7×5×⅜	27984	60.9	73.2	0.413	12.1	29.1

the stiffeners and the locations of the geometric centroid, y, in the stiffened region of the connection—measured from the bottom of the RHS (Figure 2)—are given in Table 4.

The predicted (nominal) strength for each limit state was calculated in accordance with the AISC *Specification* using the measured properties of the RHS (Tables 3 and 4) and the nominal properties of the plates and bolts (Tables 1 and 2). The latter, conservative, approach was only used for noncritical limit states to ensure they did not govern. The predicted axial strengths are summarized in Table 5, which assumes each element to be loaded by a force couple from bending acting through its geometric center. Table 6 summarizes the predicted flexural strengths, which were determined by multiplying the axial strength(s)/forces in Table 5 by their corresponding lever arm(s). The limit state governing each test is indicated by a bold value in each corresponding row, and tensile rupture of the tension flange was predicted to govern, under flexure, in 10 out of 12 connections. References to the appropriate sections of the AISC *Specification* for each limit state are also given, and Figures 3(a) and (b) illustrate the block-shear failure patterns considered (in which A_{gv} is the gross area subject to shear, A_{nv} is the net area subject to shear, and A_{nt} is the net area subject to tension).

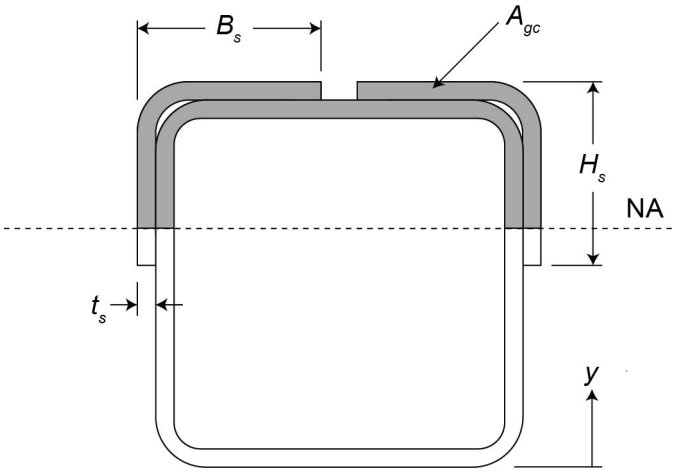

Fig. 2. Stiffened cross section.

Table 4. Measured Dimensions and Properties

No.	RHS							Stiffener			
	Shape	H (in.)	B (in.)	t (in.)	A_{fg} (in.^{2})	S_x (in.^{3})	Z_x (in.^{3})	H_s (in.)	B_s (in.)	t_s (in.)	y (in.)
1*	6×6×¼	5.94	5.98	0.226	1.15	9.16	10.8	—	—	—	2.97
2	7×7×¼	7.01	7.01	0.240	1.45	13.7	16.0	2.97	2.99	0.226	5.13
3	7×7×¼	7.01	7.01	0.240	1.45	13.7	16.0	3.50	3.50	0.240	5.29
4	8×8×½	8.03	8.03	0.457	2.84	31.0	37.3	2.54	3.52	0.342	6.20
5	8×8×⅝	8.07	8.07	0.575	3.32	37.0	45.2	4.02	4.02	0.457	5.69
6	8×8×⅝	8.07	8.07	0.575	3.32	37.0	45.2	4.04	4.04	0.575	6.14
7	10×8×½	10.04	8.07	0.453	2.84	42.4	51.4	4.04	4.04	0.575	8.15
8	12×6×¼	12.01	6.02	0.228	1.16	24.8	30.6	5.02	3.22	0.453	9.36
9	12×8×⅜	12.01	8.07	0.338	2.27	42.9	51.9	6.00	3.01	0.228	7.74
10	12×8×⅜	12.01	8.07	0.338	2.27	42.9	51.9	6.00	4.04	0.338	8.56
11	7×5×⅜	7.05	5.08	0.342	1.27	14.2	17.5	3.50	2.50	0.240	4.83
12	7×5×⅜	7.05	5.08	0.342	1.27	14.2	17.5	3.52	2.54	0.342	5.09

* Note: Unreinforced.

Table 5. Predicted Axial Strength(s) (kips)

No.	RHS				Plate(s)				Bolts		
	F_uA_{net}	$1.15A_{fg}F_y$	F_yA_{gc}	Block Shear*	Tensile Rupture	Buckling	Block Shear* (Pattern 1)	Block Shear* (Pattern 2)	Bearing	Tear-Out	Shear
	AISC *Specification* Section										
	J4.1	J4.1	J4.4	J4.3	J4.1	J4.4	J4.3	J4.3	J3.11	J3.11	J3.7
1	149	—	**142**	173	184	247	619	669	199	392	223
2	217	—	**272**	—	247	256	—	—	282	480	297
3	**215**	—	301	—	241	256	—	—	288	400	353
4	**391**	—	452	—	509	542	—	—	783	949	505
5	—	232	668	—	**242**	263	—	—	592	791	245
6	—	232	729	—	**249**	263	—	—	676	1103	240
7	**464**	—	632	—	587	625	—	—	854	1066	555
8	**250**	—	395	289	289	389	1588	1667	335	678	371
9	**429**	—	510	600	494	595	2485	2520	795	1361	481
10	**417**	—	599	514	474	641	2294	2332	663	1163	534
11	**238**	—	315	—	269	336	—	—	352	478	303
12	**241**	—	344	—	284	336	—	—	402	666	297

* Note: See Figure 3 for block-shear failure patterns.

Table 6. Predicted Flexural Strength(s) (kip-ft)											
	RHS				Plate(s)				Bolts		
	F_uA_{net}	$1.15A_{fg}F_y$	F_yA_{gc}	Block Shear*	Tensile Rupture	Buckling	Block Shear* (Pattern 1)	Block Shear* (Pattern 2)	Bearing	Tear-Out	Shear
	AISC *Specification* Section										
No.	J4.1	J4.1	J4.4	J4.3	J4.1	J4.4	J4.3	J4.3	J3.11	J3.11	J3.7
1	49	—	**50**	83	71	95	238	257	91	179	102
2	88	—	**107**	—	119	123	—	—	154	261	161
3	**87**	—	115	—	116	123	—	—	157	217	192
4	**175**	—	205	—	233	248	—	—	465	563	299
5	—	145	296	—	**122**	133	—	—	341	456	142
6	—	145	320	—	**125**	133	—	—	390	636	139
7	**253**	—	318	—	355	378	—	—	650	811	423
8	**151**	—	221	287	245	330	1347	1413	322	652	357
9	**273**	—	328	592	399	481	2010	2038	751	1285	454
10	**260**	—	370	507	379	512	1832	1862	626	1098	504
11	**87**	—	116	—	104	129	—	—	187	253	161
12	**88**	—	124	—	109	129	—	—	213	353	157

* Note: See Figure 3 for block-shear failure patterns.

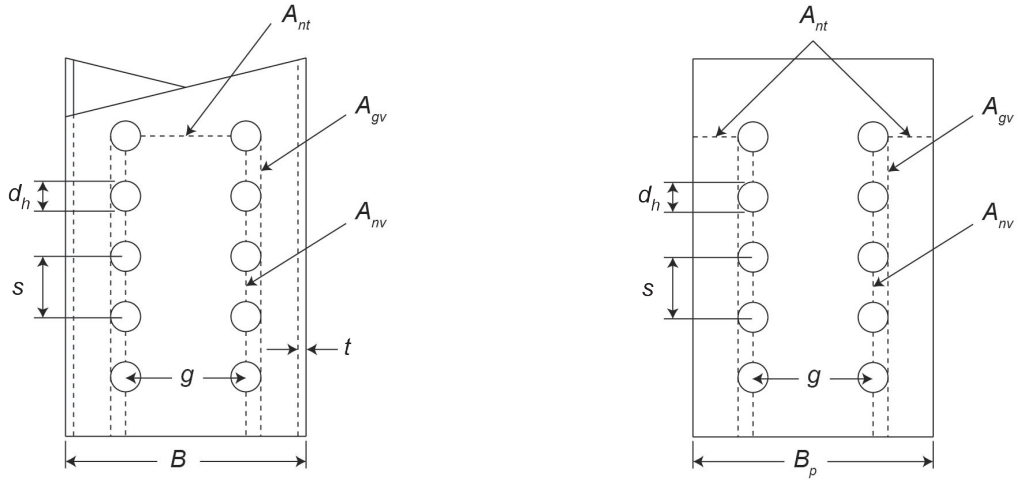

(a) Block shear failure pattern 1 (RHS and splice plate) *(b) Block shear failure pattern 2 (splice plate only)*

Fig. 3. Block shear failure patterns.

Testing Arrangement, Instrumentation, and Loading

Testing Arrangement

Each test specimen was designed with an overall length, L, of 13 ft. 2 in. (12 ft. 10 in. between centerlines of support), with a moment (or shear-free) span of 6 ft. 8 in. that included the connection (Figure 4). They were tested under four-point bending transferred by a W14×53 stiffened spreader beam that was pointed-loaded, at mid-span, by a 225-kip capacity, displacement-controlled, MTS actuator. The specimens were supported at each end by steel rollers atop several layers of blocking (used for elevation control). Web doubler plates ⅝ in. thick were also provided at the load-application and reaction points to prevent web instability.

Instrumentation

To determine the utilization of the cross sections, strain distributions around the perimeter of each RHS were measured using eight linear strain gages (SGs), equidistantly spaced through the RHS web, on the RHS corners, and on half of the tension flange, shown in Figure 5(a). As shown in Figure 5(b), the SGs were placed approximately 1.3 in. from the centerline of the critical net section for consistency in avoiding conflict with the varying bolt-head diameters. Figure 6 shows the three 24-in. string potentiometers (SPs) and two linear variable displacement transducers (LVDTs) used to measure beam displacements. The SPs were placed at mid-span and 3 ft. 4 in. in either direction. The LVDTs were placed at the supports to measure rigid-body movement.

Loading

Displacement-controlled loads were applied at an average rate of 0.2 in./min. to generate applied moments in the constant-moment region. The applied moment, M_a, was determined based on statics, using the specimen geometry and the load applied by the actuator (as measured by an in-line load cell). All data (from the SGs, SPs, LVDTs, and load cell) were recorded by a data acquisition (DAQ) system (see Figure 6) at a rate of 1 Hz.

EXPERIMENTAL RESULTS

Specimens 3, 4, and 7–12 exhibited the desired failure mode of RHS tension flange rupture, as shown typically (for Specimens 3, 4, 10 and 11) in Figure 7. Figure 8 presents typical plots of the measured strains around the cross section(s) at 50%, 75%, 90%, and 95% of the ultimate moment, M_u, and Figure 9 shows beam displacement profiles at the corresponding intervals.

The measured strains in the tension flange(s) at the critical net-section indicates a strain distribution at the onset of fracture (approximately $0.90M_u$), which extends beyond the flat portion of the tension flange (i.e., gages 1–3) and into the corner (i.e., gage 4), after which there is a loss of stiffness caused by incipient fracture near the bolt hole(s) (i.e., gages 1 and 2). When this happens, the stress/strain redistributes from the center of the tension flange out toward the stiffer corner region(s) (i.e., gages 3 and 4). This is illustrated by the typical sharp increase(s) in strain in gages 3 and 4 at $0.95M_u$.

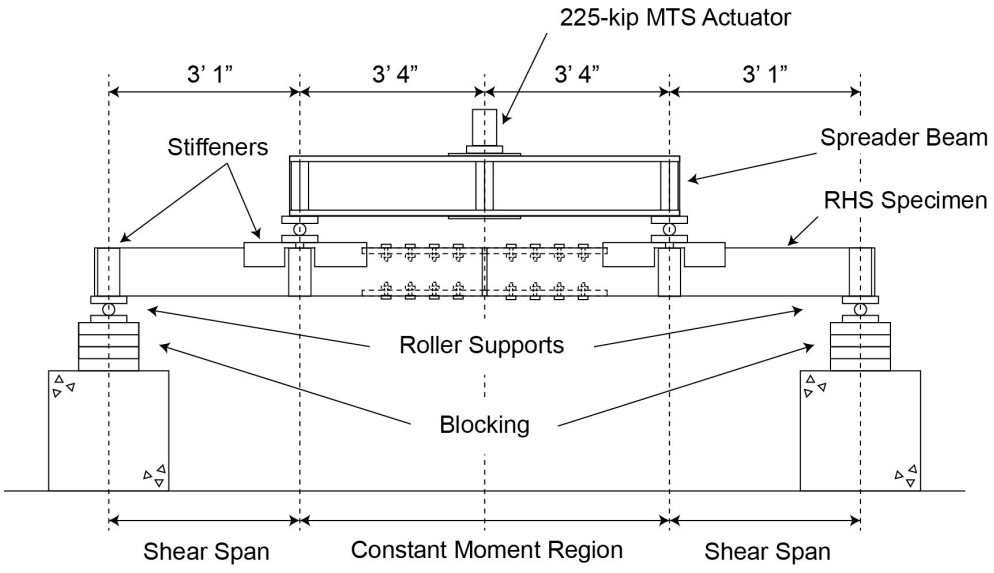

Fig. 4. Testing arrangement.

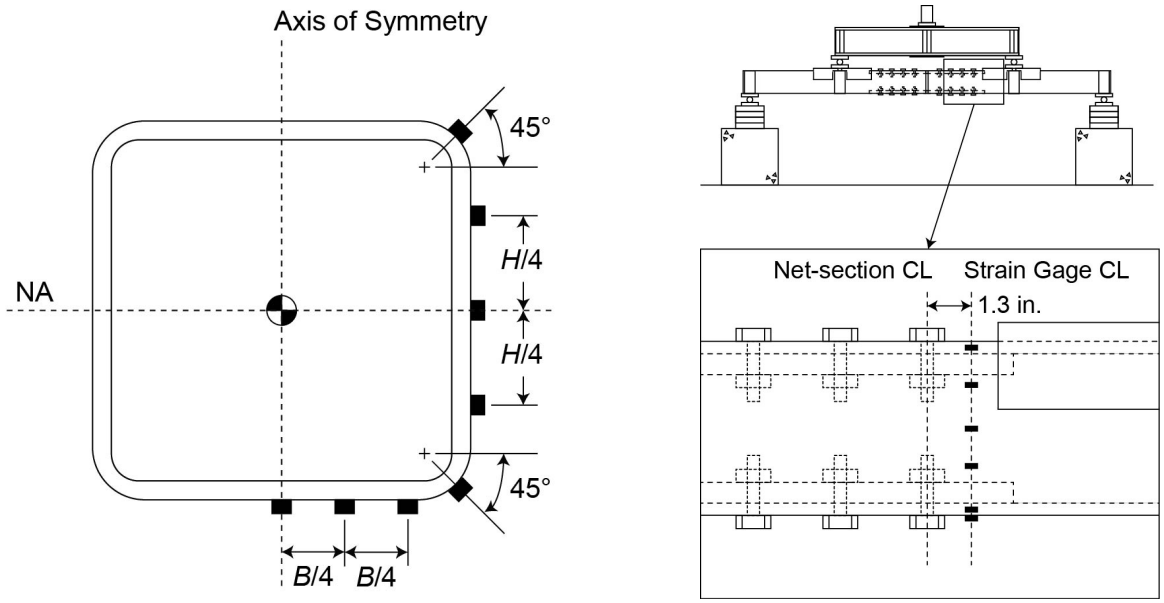

(a) Cross section *(b) Elevation*

Fig. 5. Strain gage locations.

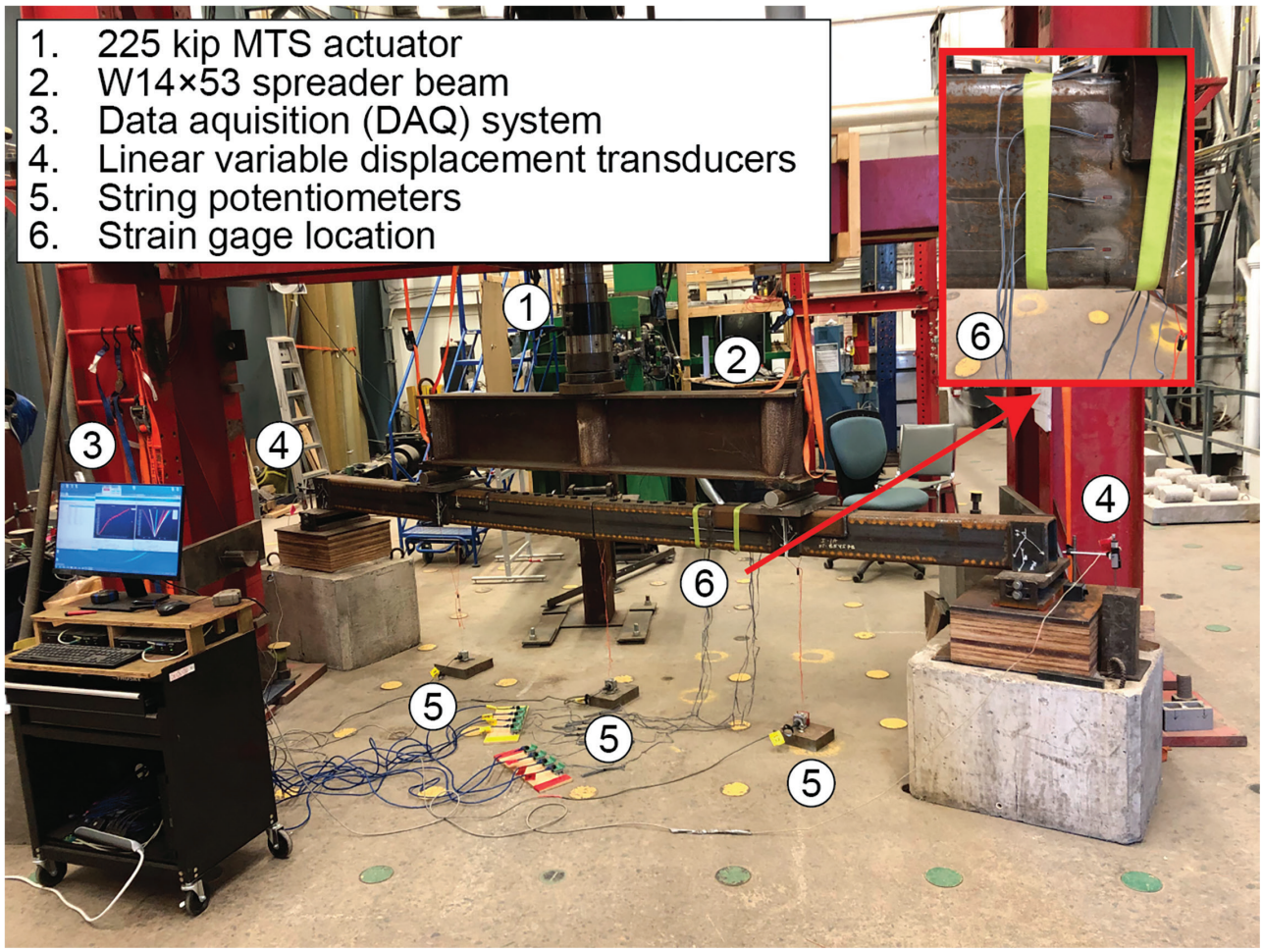

Fig. 6. Instrumentation.

(a) Specimen 3 (HSS 7×7×¼)

(b) Specimen 4 (HSS 8×8×½)

(c) Specimen 10 (HSS 12×8×⅜)

(d) Specimen 11 (HSS 7×5×⅜)

Fig. 7. RHS tension flange ruptures.

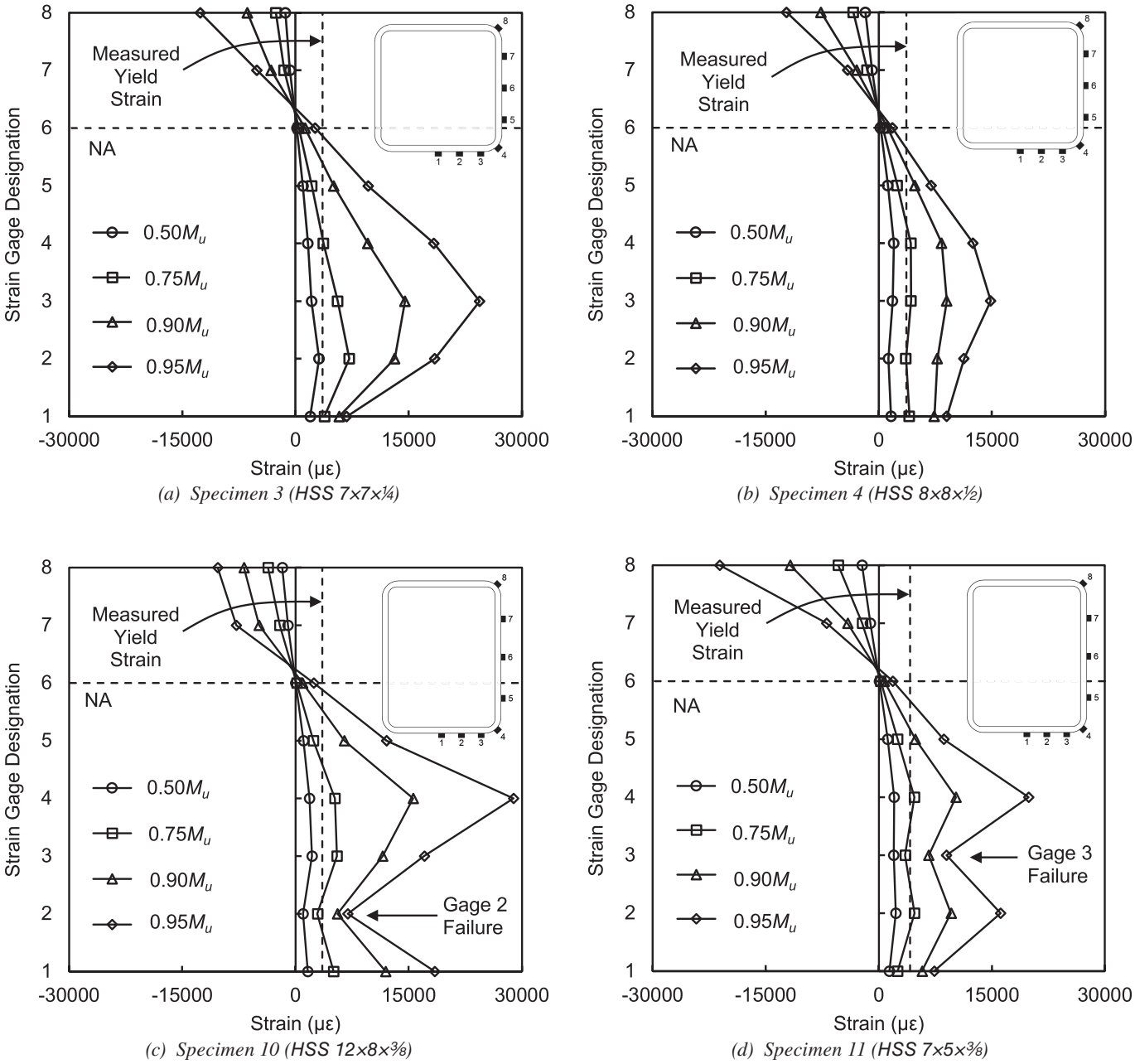

(a) Specimen 3 (HSS 7×7×¼)

(b) Specimen 4 (HSS 8×8×½)

(c) Specimen 10 (HSS 12×8×⅜)

(d) Specimen 11 (HSS 7×5×⅜)

Fig. 8. Measured strains at the critical net section.

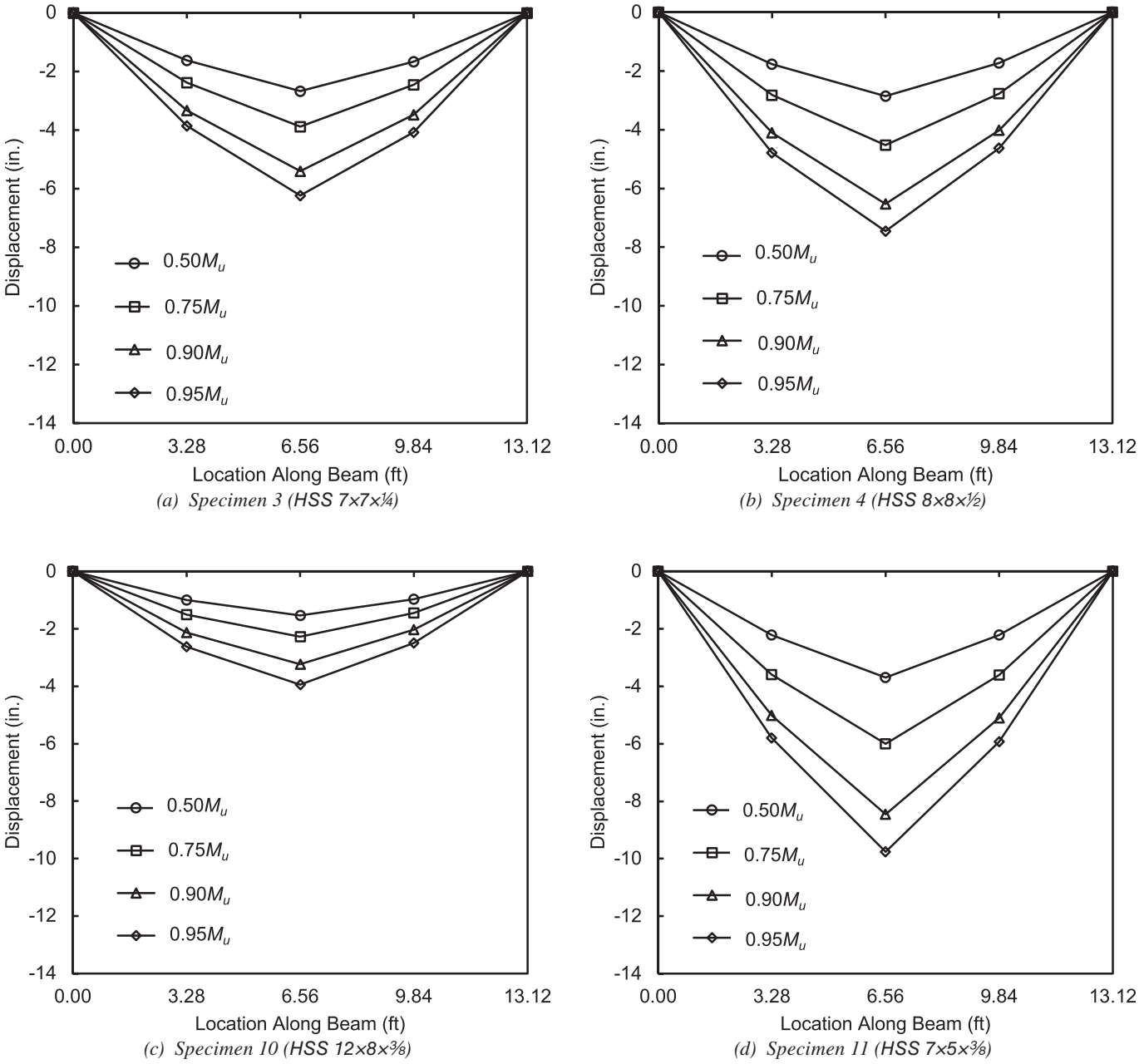

(a) Specimen 3 (HSS 7×7×¼)

(b) Specimen 4 (HSS 8×8×½)

(c) Specimen 10 (HSS 12×8×⅜)

(d) Specimen 11 (HSS 7×5×⅜)

Fig. 9. Beam displacement profiles.

Table 7. Measured and Predicted Nominal Flexural Strength(s)					
		AISC *Specification*		Equation 3	
No.	M_u (kip-ft)	M_n (kip-ft)	M_u/M_n	M_n (kip-ft)	M_u/M_n
1*	57.8	36.9	1.56	51.5	1.12
2*	88.7	74.0	1.20	91.8	0.97
3	99.2	72.2	1.37	90.6	1.10
4	214	157	1.36	188	1.14
5*	167	186	0.90	247	0.68
6*	171	190	0.90	250	0.68
7	318	217	1.47	269	1.18
8	168	101	1.67	157	1.07
9	346	204	1.70	286	1.21
10	331	184	1.80	273	1.21
11	116	64.6	1.79	93.7	1.24
12	117	67.5	1.73	95.4	1.23
Mean			1.45 (1.61)		1.07 (1.17)
CoV			0.211 (0.107)		0.177 (0.049)
* Note: Non-TFR failure modes.					

This, along with the significant amount of tensile strain consistently measured in gage 4, initially suggests that the AISC *Specification*'s current simplified approach to calculating the RHS tension flange area (A_{fg}, and hence, A_{fn}) according to Sections B4.3 and F13.1 (i.e., $b = B\text{-}4t_{des}$, where b is the width of the element) is conservative.

The four remaining specimens (i.e., Specimens 1, 2, 5, and 6) failed due to the manifestation of other limit states. Specimen 1, which was the first to be tested (without compression flange reinforcing) failed by buckling of the compression flange. Specimen 2, which included this reinforcing, failed due to excessive rotation of the connection. This rotation caused the ends of the adjoining RHS members to butt up and yield in compression, which inhibited tension failure on the opposite side. Specimens 5 and 6, which were designed using the "alternate method" (discussed in the section "Design Process for Rupture-Critical Tests"), failed by tensile rupture of the splice plate, as predicted in Table 6. Photos of these failure modes are shown in Figure 10. The peak loads for these specimens (i.e., Specimens 1, 2, 5, and 6) can nonetheless be used as conservative estimates of the tension flange rupture strength.

The ultimate moment, M_u, for each of the 12 specimens (which, for Specimens 3, 4, and 7–12, reflect the true rupture strength of the RHS tension flange) are shown in Table 7, where TFR (in the footnote) stands for tension flange rupture.

ANALYSIS

Evaluation of the AISC *Specification* Nominal Flexural Strength Prediction

The flexural strength, M_n, for each RHS specimen computed using AISC *Specification* Section F13.1 and measured properties is listed in the third column of Table 7 along with the corresponding actual-to-predicted ratios (M_u/M_n). Figure 11(a) shows correlation plots for M_n and M_u and states the mean values of the bias coefficient and coefficient of variation (CoV) for the professional factor, P, (δ_P and V_P, respectively) for (1) all 12 connections (denoted as "all") and (2) for connections that failed by rupture of the tension flange. The conservative estimates (for specimens that failed by other limit states) are indicated by upward arrows in Figure 11(a).

For comparison, the average M_u/M_n ratios and corresponding CoVs from 138 past experiments on tension flange rupture in W-shaped cross-sections are presented in Figure 11(b) for the M_n according to Section F13.1, computed using measured properties. Both numerical results (Carlson et al., 2019) and experimental results from the Georgia Institute of Technology (Schrauben, 1999; Smallidge, 1999; Swanson, 1999; Swanson and Leon, 2000), the University of Texas (Barbaran, 1996; Larson, 1996), the University of Illinois (Schneider and Teeraparbwong, 2002), and the University of California–San Diego (Sato et al., 2007), all of

(a) Specimen 1 (compression flange buckling)

(b) Specimen 2 (flange yielding in compression)

(c) Specimen 5 (tensile rupture of splice plate)

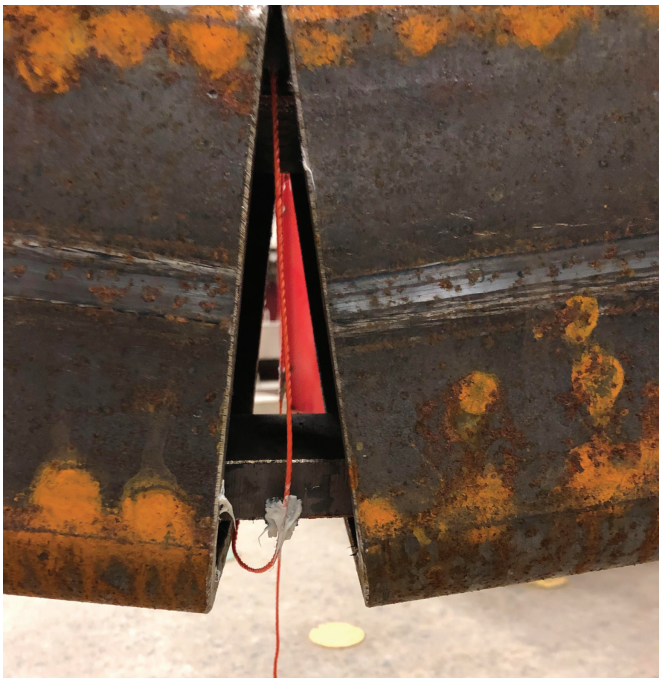

(d) Specimen 6 (tensile rupture of splice plate)

Fig. 10. Additional failure modes.

which were obtained from Swanson (2016) and Arasaratnam (2008), are included.

As shown in Figure 11, Section F13.1 underpredicts the nominal flexural strength of members with holes in their tensile flange (with an actual-to-predicted strength ratio of 1.61 for RHS, 1.65 for all previous data on W-shaped cross sections, and 1.33 for experimentally tested W-shaped cross sections). A contributing factor to the large(r) over-conservatism for RHS when compared to W-shapes is that the ratio of S_x/Z_x is inherently smaller.

The provision can be further assessed by plotting the nominally computed flexural strength normalized by M_p—that is, M_n/M_p—against the ratio A_{fn}/A_{fg}, as shown in Figure 12. In Figure 12(a), the Section F13.1 prediction is shown as a dashed black line for the dual certified ASTM A500 Grades B and C material, and in Figure 12(b), the Section F13.1 prediction is presented as dashed black or red lines for ASTM A572 Grade 50 (2025) or ASTM A992 (2020) and ASTM A36 (2019) material, respectively. Comparing these predictions to the tension flange rupture strengths (M_u/M_p) for each specimen, it is evident that Section F13.1 is a very conservative lower-bound for all (RHS and W-shaped) sections.

Figure 12 also shows that the flexural strength of member(s) with holes in the tension flange indeed depends on the ratio of A_{fn}/A_{fg}, but not as predicted by Equation 2. Figures 13(a) and (b) show the coefficients of determination, R^2, for a linear trendline through the A_{fn}/A_{fg} vs. M_u/M_p ordinates, in which $R^2 = 0.311$ for RHS, given in Figure 13(a), and $R^2 = 0.1697$ for the experimentally tested W-shaped sections, given in Figure 13(b). For all W-shaped specimens (i.e., numerical and experimental), $R^2 = 0.947$, but this is clearly dominated by the finite element (FE) data.

For rupture to manifest in the tensile flange, stresses in the extreme fiber(s) must not only reach F_u, but the material must undergo significant plastic strain (at which point, a plastic flexural stress distribution will develop over the entire net section). This was discussed by Altstadt (2004), who recommended that M_n for members with holes in the tension flange be computed using the net plastic section modulus, Z_n, and the ultimate material strength, F_uZ_n. This was later reinforced in studies by Arasaratnam (2008), Swanson (2016), and Carlson et al. (2019) for W-shaped sections. Figure 13(c) evaluates this approach for the RHS specimens, with Z_n ranging from 8.61 in.^{3} to 47.22 in.^{3} in this study [and Figure 13(d) confirms it for the W-shaped specimens]. The linear trendline for RHS in Figure 13(c) has an R^2 value of 0.967, and for the W-shapes, in Figure 13(d), $R^2 = 0.9592$ for the experiments. When the FE data in Figure 13(d) is also included, R^2 increases to 0.9896.

Recommended Approach

Based on the forgoing analysis, M_n for members (i.e., beams and girders) with holes in the tension flange is best based on the following expression:

$$M_n = F_u Z_n \tag{3}$$

Figure 14(a) shows the correlation between M_u and M_n predicted using Equation 3. The corresponding professional

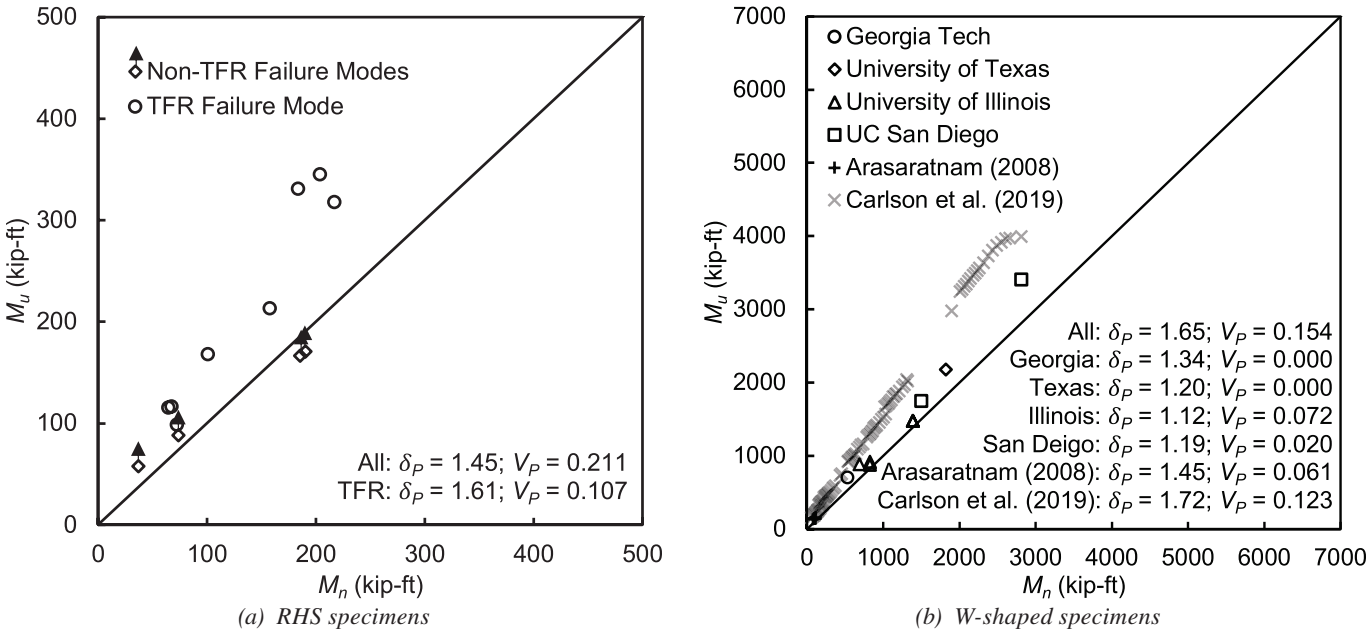

(a) RHS specimens *(b) W-shaped specimens*

Fig. 11. Correlation plots for AISC Specification *Section F13.1.*

factor statistics, δ_P and V_P, are also provided. Figure 14(b) extends this correlation to the W-shaped tests (Arasaratnam, 2008; Barbaran, 1996; Carlson et al., 2019; Larson, 1996; Sato et al., 2007; Schneider and Teeraparbwong, 2002; Schrauben, 1999; Smallidge, 1999; Swanson, 1999; Swanson and Leon, 2000).

Equation 3 is also compared to AISC *Specification* Section F13.1 prediction(s) in Figures 12(a) and 12(b) (as solid lines), shown previously. As shown in these figures and Table 7, Equation 3 is better at predicting the nominal strength (i.e., δ_P closer to unity, by about 44% on average, with a lower CoV) and the observed trends. In Table 7, the means and CoVs are given for the full data set, as well as for the eight specimens that failed by TFR (in parenthesis).

RELIABILITY ANALYSIS

Reliability indices for the foregoing provisions can be computed (and compared) using a first-order reliability method (FORM) analysis (Nowak and Lind, 1979; Schmidt and Bartlett, 2002b) in which

$$\beta = \frac{1}{\sqrt{V_R^2 + V_S^2}} \ln\left[\frac{\delta_R}{\phi}\frac{\alpha_D + \alpha_L\left(L/D\right)}{\delta_D + \delta_L\left(L/D\right)}\right] \tag{4}$$

where β is the reliability index; ϕ is the resistance factor (= 0.9); α_D and α_L are the load factors for dead and live loads, respectively (ASCE, 2022); δ_R, δ_D, and δ_L are the bias coefficients for the resistance, dead load, and live load, respectively; V_R = CoV of δ_R; V_S = CoV of total load effect; and

$$V_s = \frac{\sqrt{\left(\delta_D V_D\right)^2 + \left[\delta_L V_L\left(L/D\right)\right]^2}}{\delta_D + \delta_L\left(L/D\right)} \tag{5}$$

where V_D and V_L = CoVs of δ_D and δ_L, respectively.

This approach is described in Schmidt and Bartlett (2002b) and, in this study, a nondimensional live-to-dead load ratio (L/D) range of $1 \le L/D \le 3$ is considered (Ziemian, 2010). The value(s) of β found using Equation 4, with ASCE/SEI 7-22 (ASCE, 2022) load factors (i.e., $\alpha_D = 1.40$ for dead load only, and $\alpha_D = 1.20$ and $\alpha_L = 1.60$ for dead plus live load), can then be compared to the AISC *Specification* target of 4.0 for connections (AISC, 2022a).

Statistical Parameters

Statistical parameters for the resistance, R, (i.e., δ_R and V_R) were based on the following model:

$$R = GMPd \tag{6}$$

in which G, M, P, and d are the geometric, material, professional, and discretization factors, respectively. If these factors are lognormally distributed and independent, then

$$\delta_R = \delta_G \delta_M \delta_P \delta_d \tag{7}$$

and

$$V_R = \sqrt{V_G{}^2 + V_M{}^2 + V_P{}^2 + V_d{}^2} \tag{8}$$

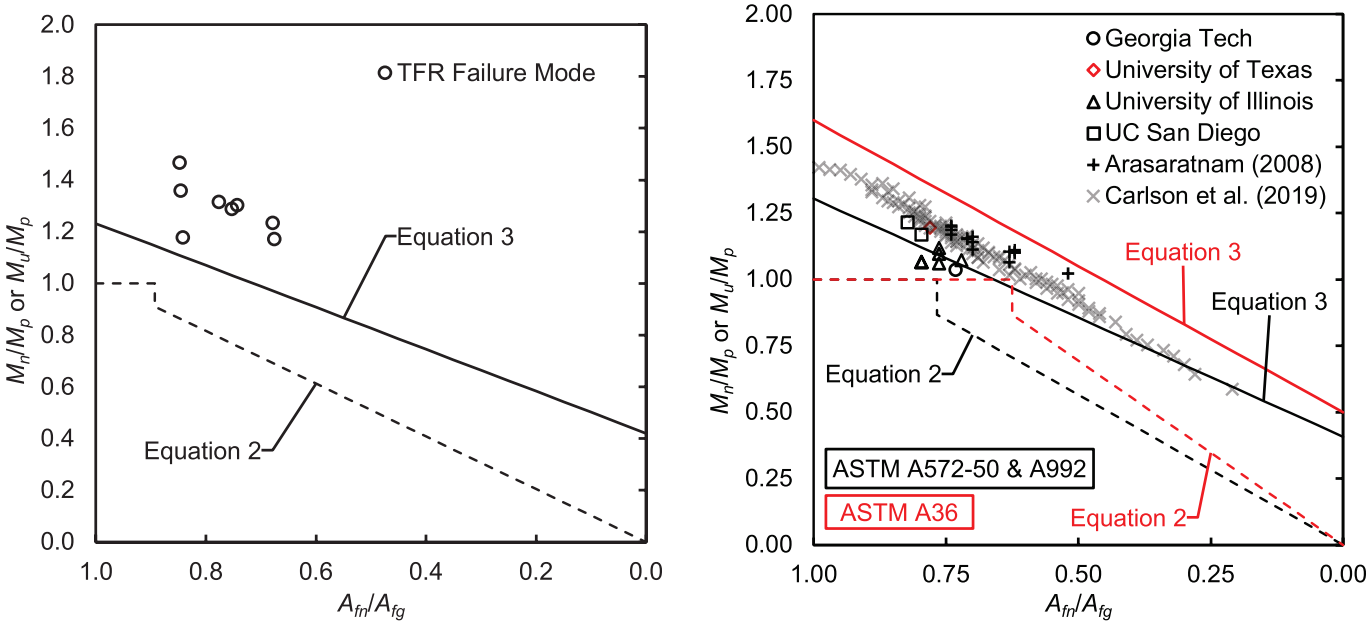

(a) RHS specimens *(b) W-shaped specimens*

Fig. 12. Evaluation of AISC Specification *Section F13.1 and Equation 3.*

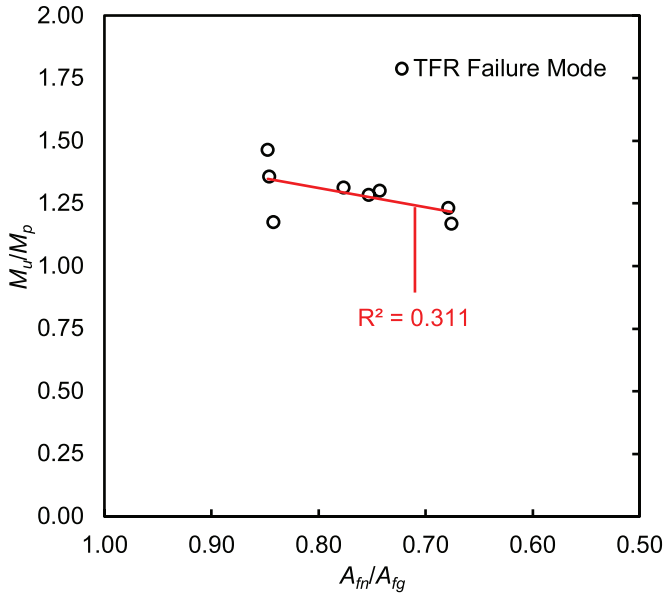

(a) A_{fn}/A_{fg} *vs.* M_u/M_p *for RHS specimens*

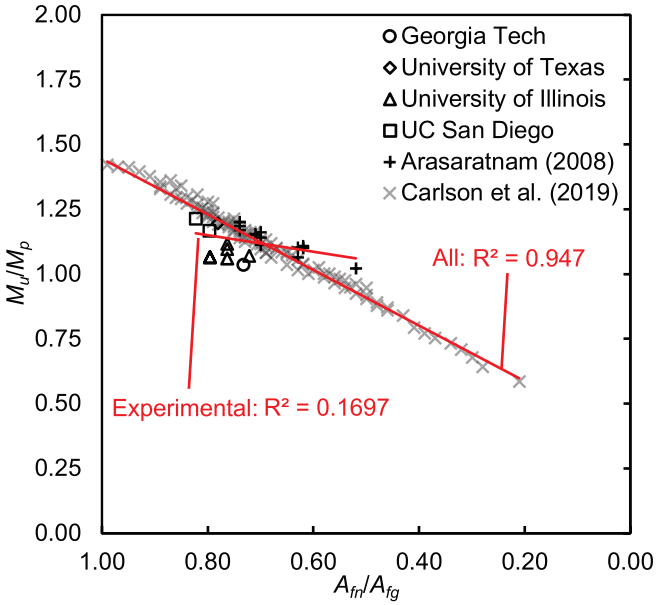

(b) A_{fn}/A_{fg} *vs.* M_u/M_p *for W-shaped specimens*

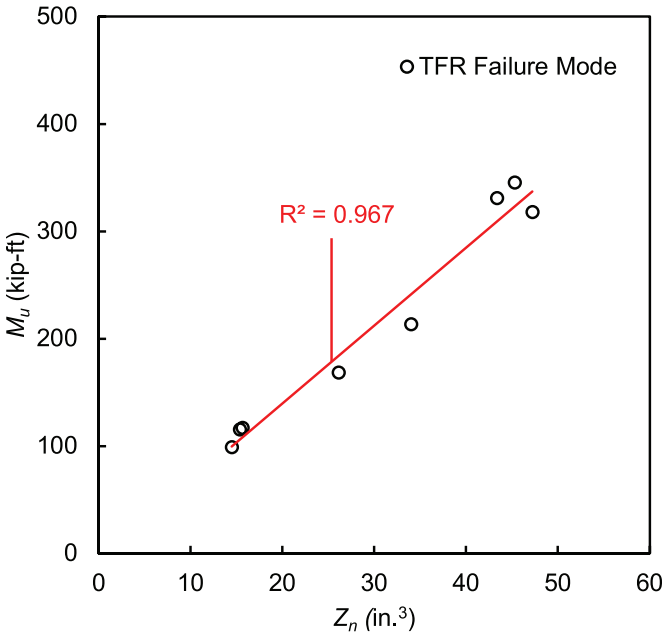

(c) Z_n *vs.* M_u *for RHS specimens*

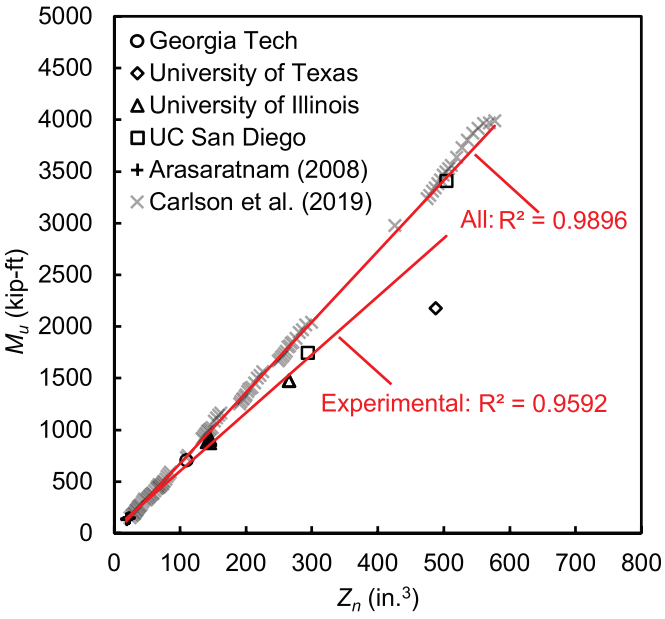

(d) Z_n *vs.* M_u *for W-shaped specimens*

Fig. 13. Assessment of flexural strength dependence on A_{fn}/A_{fg} *and* Z_n.

Table 8. Statistical Parameters for Basic Random Variables		
Variable	**δ**	***V***
B	1.004	0.018
H	1.000	0.010
*t**	0.994	0.007
F_y	1.280	0.090
F_u	1.180	0.080
* Note: Statistics for *t* are with respect to AISC's design wall thickness for ASTM A500 RHS.		

where δ_G, δ_M, and δ_d are the bias coefficients for the geometric, material, and discretization factors, respectively, and V_G, V_M, and V_d are the associated CoVs.

Geometric Factors

For compact RHS that do not satisfy Equation 1, AISC *Specification* Section F13.1 defers to Section F7.1, in which $M_n = M_p = F_yZ$, where Z is the plastic section modulus about the axis of bending. In this case $G = Z$, which can be expressed in terms of B, H, and t. For sections that satisfy Equation 1, M_n is predicted according to the AISC *Specification* using Equation 2, and G is the product of A_{fn}/A_{fg} and S_x, computed for an RHS (with the plastic neutral axis at $H/2$ in the web) as

$$\frac{A_{fn}S_x}{A_{fg}} = \left(1-\frac{n_r d_h}{b}\right)\times \left\{\frac{4\left[\frac{bt^3}{12}+bt\left(\frac{H}{2}-\frac{t}{2}\right)^2\right]+4\left[\frac{th^3}{12}\right]+8\left[0.634t^4+0.75\pi t^2\left(\frac{H}{2}-1.01t\right)^2\right]}{H}\right\} \quad (9)$$

where h = element height = H-4t (AISC, 2022a).

For the recommended approach using Equation 3, $G = Z_n$, computed as

$$Z_n = 2A_{net}\bar{x} \quad (10)$$

in which

$$A_{net} = t\left(b+h+1.5\pi t-n_r d_h\right) \quad (11)$$

and

$$\bar{x} = \frac{\left[0.5t(b-n_r d_h)(H-t)\right]+\left[\left(\frac{h}{2}\right)(2t)\left(\frac{h}{4}\right)\right]+\left[(1.5\pi t^2)\left(\frac{H}{2}-1.01t\right)\right]}{\left[t(b-n_r d_h)\right]+\left[\left(\frac{h}{2}\right)(2t)\right]+\left[1.5\pi t^2\right]} \quad (12)$$

where $\bar{x}$ is the distance between the centroid of A_{net} and the plastic neutral axis.

The statistical parameters for G for each provision were derived for RHS using the statistics for the basic random variables (B, H, and t) (Table 8) (Ncube and Tousignant, 2024), based on

$$\bar{\delta} = \frac{1}{n}\left[\sum_{i=1}^{n}(\delta_i)\right] \quad (13)$$

and

$$V = \frac{1}{\bar{\delta}_i}\sqrt{\frac{1}{n}\left[\sum_{i=1}^{n}(V_i\delta_i)^2+\sum_{i=1}^{n}\left(\bar{\delta_i}-\delta_i\right)^2\right]} \quad (14)$$

where $\bar{\delta}$ is the overall mean bias coefficient value, δ_i = bias coefficient value for an individual shape, V is the coefficient of variation, V_i is the coefficient of variation for an individual shape, and n is the number of specimens.

Using the data in Table 8 for the basic random variables, adopted from Ncube and Tousignant (2024), and considering an outside corner radius of 2.0t (AISC, 2022a), δ_G and V_G were calculated individually for the eight RHS shapes that exhibited tension flange rupture as follows:

$$\delta_G = \frac{G_m}{G_{des}} \quad (15)$$

and

$$V_G^2 = \frac{1}{G_m^2}\Sigma\left[\left(\frac{\partial G_m}{\partial j}\right)\sigma_j\right]^2 \quad (16)$$

where G_m is the mean value of G, G_{des} is the design value of G, j is the random variable(s) comprising G, and σ_j is the standard deviation of the random variable(s) j.

Material Factors

For compact RHS that do not satisfy Equation 1, $M = F_y$ according to the AISC *Specification*. When Equation 1 is satisfied, and for the recommended approach (Equation 3), $M = F_u$. The statistical parameters for F_y and F_u were computed by Ncube and Tousignant (2024) from the results of

Liu (2016). The data shown represents RHS made to the dual certified ASTM A500 in Grades B and C (ASTM, 2021).

Discretization Factor and Load Effects

The statistical parameters for dead and live load effects were taken as $\delta_D = 1.05$, $V_D = 0.100$ and $\delta_L = 0.78$, $V_L = 0.320$, respectively, and the discretization factor was taken as $\delta_d = 1.04$ and $V_d = 0.028$ (Schmidt and Bartlett, 2002a).

FORM ANALYSIS RESULTS

The mean bias coefficient and CoV of the geometric factor for Section F13.1 were found to be $\delta_G = 0.997$ and $V_G = 0.037$, and the professional factor statistics ($\delta_P = 1.61$ and $V_P = 0.107$) are as shown in Figure 11(a) for the specimens failing by TFR only. The mean bias coefficient and CoV of the geometric factor for Equation 3 were found to be $\delta_G = 0.997$ and $V_G = 0.016$, with the professional factor statistics ($\delta_P = 1.17$ and $V_P = 0.049$) shown in Figure 14(a), for the specimens failing by TFR only. By combining these statistics with those of the material and discretization factors, in accordance with Equations 7 and 8, the bias factor and CoV for R can be determined. For Section F13.1, $\delta_R = 2.14$ with $V_R = 0.147$, and for Equation 3, $\delta_R = 1.43$ with $V_R = 0.099$.

To assess the inherent reliability of AISC *Specification* Section F13.1 for W-shape sections, values of δ_G, δ_M, $\delta_d = 1.01$, 1.11, 1.05, respectively, and V_G, V_M, $V_d = 0.035$, 0.063, 0.035, respectively, were adopted from Schmidt and Bartlett (2002a). Similarly, to assess Equation 3, values of δ_G, δ_M, $\delta_d = 1.01$, 1.13, 1.05, respectively, and V_G, V_M, $V_d = 0.034$, 0.044, 0.035, respectively, are used (Schmidt and Bartlett, 2002a), resulting in $\delta_R = 1.93$ and $V_R = 0.173$ for Section F13.1 and $\delta_R = 1.29$ and $V_R = 0.076$ for Equation 3 for all data. For experimentally tested W-shapes, $\delta_R = 1.56$ and 1.24 and $V_R = 0.149$ and 0.084 for Section F13.1 and Equation 3, respectively.

Ranges of β computed from Equation 4, with $\phi = 0.90$, are shown in Figure 15 for both the Section F13.1 provision and Equation 3. In Figure 15, the dashed horizontal line corresponds to the target safety index of $\beta = 4.0$ as outlined in AISC *Specification* Chapter B. The vertical line represents the lower bound of $L/D = 1.0$ considered for this study (Ziemian, 2010). As shown, values of β computed for both Section F13.1—that is, Figures 15(a) and 15(b)—and Equation 3—that is, Figures 15(c) and 15(d)—are at or above the target across the full range of $1 \le L/D \le 3$ for both RHS and W-shaped sections. The high safety indices for Section F13.1 are due almost exclusively to over-conservatism in the current design model.

CONCLUSION

The scope of testing presented herein covered 12 rectangular hollow section (RHS)-to-RHS splice connections loaded under monotonic four-point bending (about their strong axis) to produce tension flange rupture. Each RHS was dual certified to ASTM A500 Grades B and C with an aspect

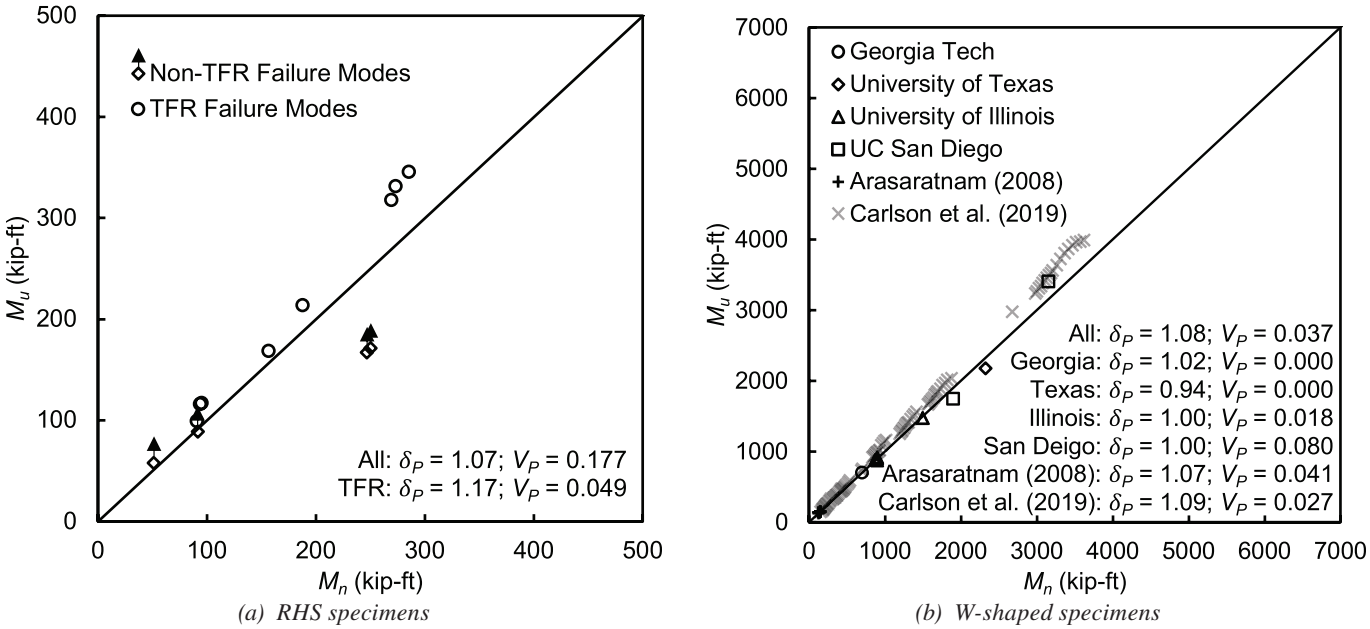

(a) RHS specimens *(b) W-shaped specimens*

Fig. 14. Correlation plots for Equation 3.

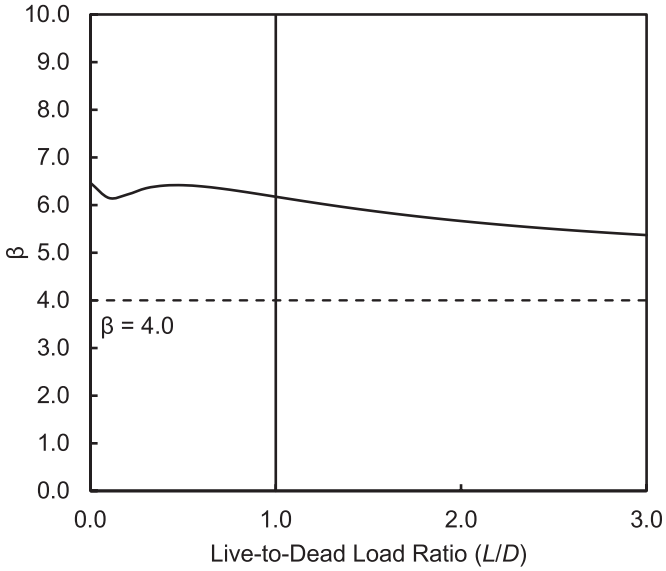

(a) AISC Specification *Section F13.1 for RHS specimens*

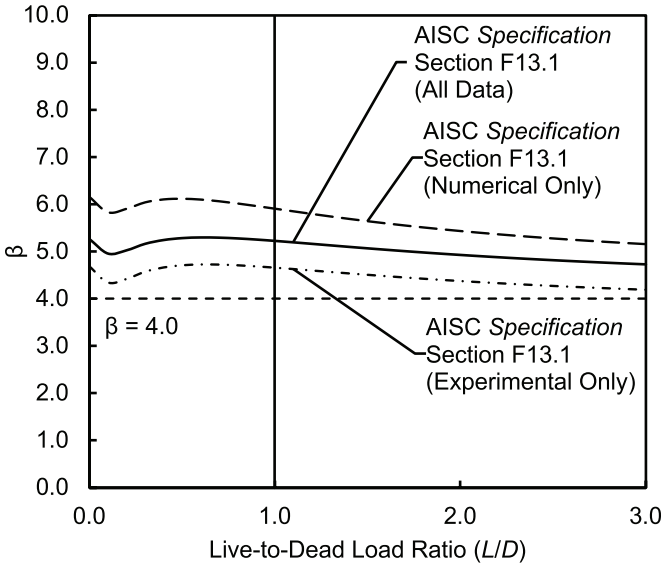

(b) AISC Specification *Section F13.1 for W-shaped specimens*

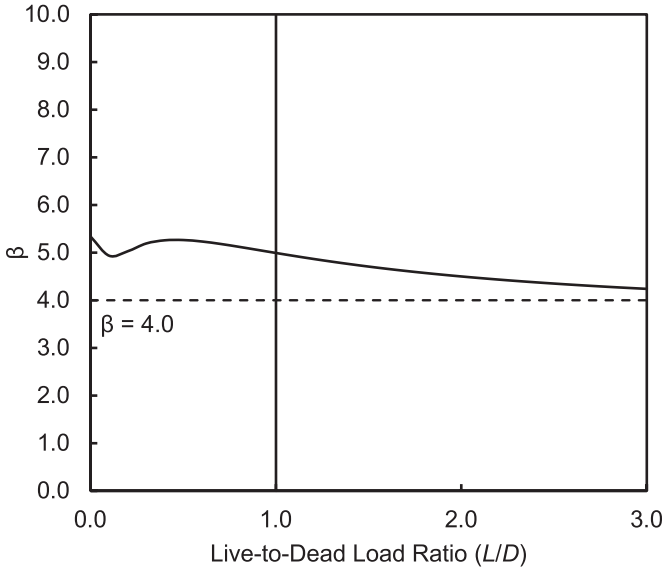

(c) Equation 3 for RHS specimens

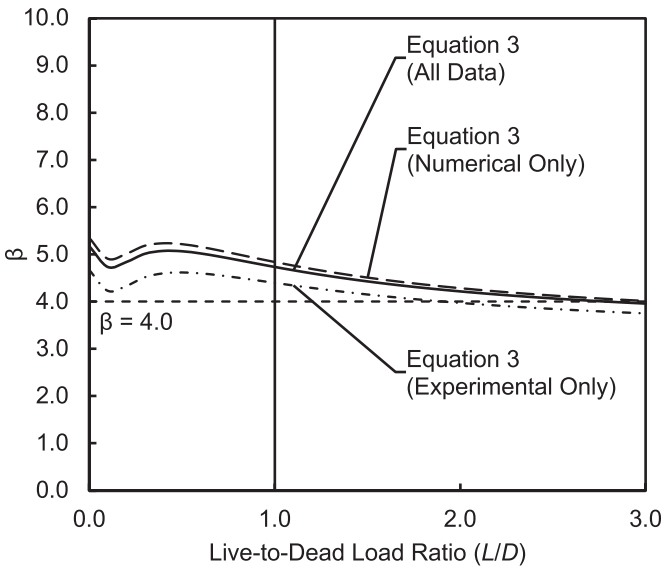

(d) Equation 3 for W-shaped specimens

Fig. 15. β *versus* L/D *for AISC* Specification *Section F13.1 and Equation 3.*

ratio(s) of 1.0 to 2.0, nominal wall thickness(es) from ¼ in. to ⅝ in., a flange slenderness ratio(s) from 10.03 to 25.16, and a web slenderness ratio(s) from 10.03 to 48.71. Each connection had a net plastic section modulus ranging from 8.61 in.^{3} to 47.22 in.^{3} and either a one- or two-row bolt configuration. Based on these results, and an analysis of 138 previous tests on W-shaped sections (113 numerical and 25 experimental), which were primarily comprised of ASTM A992 and A572-50 material, it can be concluded that:

- AISC *Specification* Section F13.1 predictions of M_n for members with holes in their tension flange are over-conservative.
- The flexural strength of members with holes in their tension flange is well-correlated with Z_n, and less so with the ratio of A_{fn}/A_{fg}.
- The nominal strength equation given by Equation 3, which utilizes Z_n and F_u, provides a significant improvement in accuracy over AISC *Specification* Section F13.1, while still providing acceptable levels of reliability.

It is therefore recommended that the latter half of AISC *Specification* Section F13.1 be modified to:

F13. PROPORTIONS OF BEAMS AND GIRDERS

1. Strength Reductions for Members with Bolt Holes in the Tension Flange

In addition to the limit states specified in other sections of this chapter, the nominal flexural strength, M_n, shall be limited according to the limit state of tensile rupture of the tension flange.

$$M_n = F_u Z_n \quad \text{(F13-1)}$$

where

Z_n = minimum net plastic section modulus, in.^{3} (mm^3)

F_u = specified minimum tensile strength, ksi (MPa)

ACKNOWLEDGMENTS

The authors of this paper gratefully acknowledge the financial support of the Canadian Institute of Steel Construction (CISC) and the Natural Sciences of Engineering Research Council (NSERC). The authors also wish to acknowledge Atlas Tube for supplying the steel rectangular hollow sections and Cherubini Metal Works for their fabrication services.

SYMBOLS

A_{fg} Gross area of tension flange, in.^{2}

A_{fn} Net area of tension flange, in.^{2}

A_{gc} Gross area subjected to compression, in.^{2}

A_{gv} Gross area subjected to shear, in.^{2}

A_{net} Net-effective area subjected to tension under pure flexure, in.^{2}

A_{nt} Net area subjected to tension, in.^{2}

A_{nv} Net area subjected to shear, in.^{2}

B Overall width, in.

B_p Splice plate overall width, in.

B_s Stiffener plate overall width, in.

E Modulus of elasticity, ksi

F_{nv} Nominal shear stress of the bolt, ksi

F_u Specified minimum tensile strength, ksi

F_y Specified minimum yield strength, ksi

G Geometric factor

G_{des} Design value of the geometric factor

G_m Mean value of the geometric factor

H Overall height, in.

H_s Stiffener plate overall height, in.

L Overall beam length, in.

M Material factor

M_a Applied moment, kip-ft

M_n Nominal flexural strength, kip-ft

M_p Plastic moment, kip-ft

M_u Ultimate moment, kip-ft

P Professional factor

R Resistance factor

R^2 Coefficient of determination

S_n Minimum net elastic section modulus taken about the axis of bending, in.^{3}

S_x Minimum elastic section modulus taken about the x-axis, in.^{3}

V Coefficient of variation

V_D Coefficient of variation of the dead load

V_d Coefficient of variation of the discretization factor

V_G Coefficient of variation of the geometric factor

V_i Coefficient of variation for an individual shape

V_L Coefficient of variation of the live load

V_M Coefficient of variation of the material factor

V_P Coefficient of variation of the professional factor

V_R Coefficient of variation of the resistance factor

V_S Coefficient of variation of the total load effect

Y_t Coefficient corresponding to yield-to-tensile strength ratio

Z Plastic section modulus taken about the axis of bending, in.^{3}

Z_x Plastic section modulus taken about the x-axis, in.^{3}

Z_n Net plastic section modulus taken about the axis of bending, in.^{3}

b Width of the element, in.

d Discretization factor

d Nominal diameter of fastener, in.

d_h Diameter of bolt hole, in.

g Transverse center-to-center spacing between fastener gage lines, in.

h Height of the element, in.

j Random variable(s) comprising the geometric factor expression

l_{bolt} Nominal bolt length, in.

l_c Clear distance, in the direction of the force, between the edge of the hole and the edge of the adjacent hole or edge of material, in.

n Number of specimens

n_b Number of bolts per connection

n_r Number of bolts per row

s Longitudinal center-to-center spacing of any two consecutive bolt holes, in.

t Measured wall thickness, in.

t_{des} Design wall thickness, in.

t_{nom} Nominal wall thickness, in.

t_p Splice plate thickness, in.

t_s Stiffener plate thickness, in.

$\bar{x}$ Distance between the centroid of net-effective area subjected to tension and the plastic neutral axis, in.

y Geometric centroid, in.

α_D Load factor for dead load

α_L Load factor for live load

β Reliability index

$\bar{\delta}$ Overall mean bias coefficient value

δ_D Bias coefficient of the dead load

δ_d Bias coefficient of the discretization factor

δ_G Bias coefficient of the geometric factor

δ_i Bias coefficient value for an individual shape

δ_L Bias coefficient of the live load

δ_M Bias coefficient of the material factor

δ_P Bias coefficient of the professional factor

δ_R Bias coefficient of the resistance factor

ε_r Strain at rupture, in./in.

ε_u Strain at the ultimate stress, in./in.

ε_y Strain at the yield stress, in./in.

σ_j Standard deviation of the random variable(s) comprising the geometric factor expression

ϕ Resistance factor

REFERENCES

AISC (2022a), *Specification for Structural Steel Buildings*, ANSI/AISC 360-22, American Institute of Steel Construction, Chicago, Ill.

AISC (2022b), *Seismic Provisions for Structural Steel Buildings*, ANSI/AISC 341-22, American Institute of Steel Construction, Chicago, Ill.

AISC (2023), *Steel Construction Manual*, 16th Ed., American Institute of Steel Construction, Chicago, Ill.

Altstadt, S. (2004), "Tensile Strength and Ductility of High Performance Steel Girders," M.S. Thesis, University of Minnesota, Minneapolis, Minnesota.

Arasaratnam, P. (2008), "Effects of Flange Holes on Flexural Behavior of Steel Beams," M.A.Sc. Thesis, Department of Civil Engineering, McMaster University, Hamilton, Ontario.

ASCE (2022), *Minimum Design Loads and Associated Criteria for Buildings and Other Structures*, ASCE/SEI 7-22, American Society for Civil Engineers, Reston, Va.

ASTM (2019), *Standard Specification for Carbon Structural Steel*, A36/A36M, American Society for Testing and Materials International, West Conshohocken, Pa.

ASTM (2020), *Standard Specification for Structural Steel Shapes*, A992/A992M, American Society for Testing and Materials International, West Conshohocken, Pa.

ASTM (2021), *Standard Specification for Cold-Formed Welded and Seamless Carbon Steel Structural Tubing in Rounds and Shapes*, A500/A500M-21, American Society for Testing and Materials International, West Conshohocken, Pa.

ASTM (2022), *Standard Test Methods for Tension Testing of Metallic Materials*, ASTM E8/E8M-22, American Society for Testing and Materials International, West Conshohocken, Pa.

ASTM (2023), *Standard Specification for High Strength Structural Bolts and Assemblies, Steel and Alloy Steel, Heat Treated, Inch Dimensions 120 ksi and 150 ksi Minimum Tensile Strength, and Metric Dimensions 830 MPa and 1040 MPa Minimum Tensile Strength*, ASTM F3125/F3125M, American Society for Testing and Materials International, West Conshohocken, Pa.

ASTM (2025), *Standard Specification for High-Strength Low-Alloy Columbium-Vanadium Structural Steel*, A572/A572M, American Society for Testing and Materials International, West Conshohocken, Pa.

Barbaran, F.V.U. (1996), "Tension Bolt Behavior in Moment Connections for Seismic Applications," M.S. Thesis, Department of Civil, Architectural, and Environmental Engineering, University of Texas at Austin, Austin, Texas.

Carlson, R.B., Swanson, J.A., Rassati, G.A., and Burns, T.M. (2019), "Flexural Strength of Steel Beams with Holes in the Tension Flange," Internal Report, Department of Civil and Environmental Engineering, University of Cincinnati, Cincinnati, Ohio.

CSA (2023), *General Requirements for Rolled or Welded Structural Quality Steel/Structural Quality Steel*, CSA G40.20-13/G40.21-13 (R2023), Canadian Standards Association, Toronto, Ontario.

Dexter, R.J. and Altstadt, S.A. (2004), "Strength and Ductility of Tension Flange Girders," *Recent Developments in Bridge Engineering*, *Proceedings of the Second New York City Bridge Conference*, October 20–21, 2003, New York, N.Y., Mahmoud, K.M. (ed.), A.A. Balkema/Swets & Zeitlinger, Lisse, The Netherlands, pp. 67–81.

Larson, P.C. (1996), "The Design and Behavior of Bolted Beam-to-Column Frame Connections under Cyclical Loading," M.S. Thesis, Department of Civil, Architectural, and Environmental Engineering, University of Texas at Austin, Austin, Texas.

Liu, J. (2016), "Updates to Expected Yield Stress and Tensile Stress Ratios for Determination of Expected Member Capacity in the 2016 AISC Seismic Provisions," *Engineering Journal*, AISC, Vol. 53, No. 4, pp. 215–228.

Ncube, M. and Tousignant, K. (2024), "Assessing the Impact of Design Wall Thickness on the Reliability of ASTM A500 HSS Compression Members," *Proceedings of the Annual Conference of the Canadian Society of Civil Engineering*, July 5–7, Niagara Falls, Ontario.

Nowak, A.S. and Lind, N.C. (1979), "Practical Bridge Code Calibration," Journal of the Structural Division, ASCE, Vol. 105, No. 12, pp. 2497–2510.

Sato, A., Newell, J., and Uang, C.M. (2007), "Cyclic Testing of Bolted Flange Plate Steel Moment Connections for Special Moment Frames," Final Report to the American Institute of Steel Construction from the Department of Structural Engineering, University of California, San Diego.

Schmidt, B.J. and Bartlett, F.M. (2002a), "Review of Resistance Factor for Steel: Data Collection," *Canadian Journal of Civil Engineering*, Vol. 29, No. 1, pp. 98–108.

Schmidt, B.J. and Bartlett, F.M. (2002b), "Review of Resistance Factor for Steel: Resistance Distributions and Resistance Factor Calibration," *Canadian Journal of Civil Engineering*, Vol. 29, No. 1, pp. 109–118.

Schneider, S.P. and Teeraparbwong, I. (2002), "Inelastic Behavior of Bolted Flange Plate Connections," *Journal of Structural Engineering*, ASCE, Vol. 128, No. 4, pp. 492–500.

Schrauben, C.S. (1999), "Behavior of Full-Scale Bolted Beam-to-Column T-Stub and Clip Angle Connections under Cyclic Loads," M.S. Thesis, submitted to the faculty of the Georgia Institute of Technology, Atlanta, Georgia.

Smallidge, J.M. (1999), "Behavior of Bolted Beam-to-Column T-Stub Connections under Cyclic Loading," M.S. Thesis, submitted to the faculty of the Georgia Institute of Technology, Atlanta, Georgia.

Swanson, J.A. (1999), "Characterization of the Strength, Stiffness, and Ductility of T-Stub Connections," Ph.D. dissertation, Georgia Institute of Technology, Atlanta, Georgia.

Swanson, J.A. (2016), "Strength of Beams in Beam-to-Column Connections with Holes in the Tension Flange," *Engineering Journal*, AISC, Vol. 53, pp. 159–172.

Swanson, J.A. and Leon, R.T. (2000), "Bolted Steel Connections: Tests on T-Stub Components," *Journal of Structural Engineering*, ASCE, Vol. 126, No. 1, pp. 50–56.

Yuan, Q., Swanson, J., and Rassati, G.A. (2004), "An Investigation of Hole Making Practices in the Fabrication of Structural Steel," Internal Report, Department of Civil and Environmental Engineering, University of Cincinnati, Cincinnati, Ohio.

Ziemian, R.D. (2010), *Guide to Stability Design Criteria for Metal Structures*, 6th Ed., Wiley, N.Y.

Optimal Design of W-Shape Members Subjected to Combined Forces

ABBAS AMINMANSOUR

ABSTRACT

Design of members subjected to combined forces is an iterative process in which the designer selects a trial section and checks the selection for compliance with the appropriate provisions of AISC *Specification for Structural Steel Buildings* Chapter H. This process is repeated until a desired section is identified. The introduction of AISC *Steel Construction Manual* Table 6-1 has made the calculations involved in checking different trial sections considerably easier and faster. However, there is still no comprehensive resource for the designer to select an initial trial section for various scenarios of members subjected to combined forces which leads to an optimal final selection quickly. This paper presents a method and aids for more rational and efficient selection of trial sections for W-shapes subject to combined compression and bending about one or two principal axes, tension and bending about one or two principal axes, or biaxial bending. Unlike some previous methods, there are no limitations on the values of unbraced and effective lengths (e.g., requiring that $L_b = L_{cy}$). The design aids are developed for all W-shapes in Grade 50 steel using both LRFD and ASD methods. The method presented converges quickly, reducing the need for multiple repeated calculations before a final W-shape is selected. Example problems are also included.

Keywords: steel design, structural steel, combined forces, compression and bending, beam-column, tension and bending, biaxial bending, structural optimization.

INTRODUCTION

Section H1 of the AISC *Specification for Structural Steel Buildings* (2022), hereafter referred to as the AISC *Specification*, requires compliance with AISC *Specification* Equation H1-1a or H1-1b for design of doubly and singly symmetric members subject to flexure and axial force. Note that the term *force* refers to both axial load as well as bending moment.

When $\frac{P_r}{P_c} \geq 0.20$

$$\frac{P_r}{P_c} + \frac{8}{9}\left(\frac{M_{rx}}{M_{cx}} + \frac{M_{ry}}{M_{cy}}\right) \leq 1.0 \quad \text{(AISC } \textit{Spec.} \text{ Eq. H1-1a)}$$

When $\frac{P_r}{P_c} < 0.20$

$$\frac{P_r}{2P_c} + \left(\frac{M_{rx}}{M_{cx}} + \frac{M_{ry}}{M_{cy}}\right) \leq 1.0 \quad \text{(AISC } \textit{Spec.} \text{ Eq. H1-1b)}$$

Abbas Aminmansour, Associate Professor, Structures Concentration, School of Architecture, University of Illinois at Urbana-Champaign, Urbana, Ill. Email: aamin@illinois.edu

Paper No. 2025-08

where

P_r = required axial strength, determined in accordance with AISC *Specification* Chapter C using LRFD or ASD load combinations, kips
= P_u (LRFD) and P_a (ASD), must include second-order effects for compression and bending

P_c = available axial strength determined in accordance with AISC *Specification* Chapter D for tension and Chapter E for compression, kips
= ϕP_n (LRFD) and P_n/Ω (ASD)

M_r = required flexural strength, determined in accordance with AISC *Specification* Chapter C using LRFD or ASD load combinations, kip-in.
= M_u (LRFD) and M_a (ASD), must include second-order effects for compression and bending

M_c = available flexural strength determined in accordance with AISC *Specification* Chapter F, kip-in.
= $\phi_b M_n$ (LRFD) and M_n/Ω_b (ASD)

AISC *Specification* Equations H1-1a and H1-1b apply to members subjected to either compression and bending (beam-columns) or tension and bending as well as members subjected to biaxial bending.

Second-order effects do not adversely affect the strength of members subject to combined tension and bending. However, second-order effects need to be considered in the design of members subject to compression and bending using pertinent provisions of the AISC *Specification* after identifying a trial section.

For biaxial bending ($P_r = 0$, $P_r/P_c = 0 < 0.20$), only the portion of the AISC *Specification* Equation H1-1b with moment terms applies; namely,

$$\frac{M_{rx}}{M_{cx}} + \frac{M_{ry}}{M_{cy}} \leq 1.0 \quad (1)$$

For members subject to tension and bending, AISC *Specification* Section H4 offers provisions for tensile rupture of the tension flange with holes subjected to tension. This section in turn references AISC *Specification* Section F13.1, "Strength Reductions for Members with Holes in the Tension Flange." The reader may refer to Swanson (2016) for an in-depth overview of this subject.

Given the scope of this article, which is the optimum selection of trial sections for members subject to combined forces, there will not be any further elaboration of the calculation of M_{rx}, M_{ry}, M_{cx}, and M_{cy} in the remainder of this article.

REVIEW OF PREVIOUS WORK

Over the last few decades, multiple researchers have offered procedures and design aids for facilitating selection of a trial section and/or checking the selection for compliance with pertinent provisions of the AISC *Specification*.

A very early method for selecting a beam-column trial section was presented by Rubinsky (1968). The author offered two methods, which he referred to as the PM_X and MP methods, for selecting a trial section.

The PM_X method converted the axial load and the bending moment about the *y*-axis into equivalent bending moments about the *x*-axis. The values of the converted axial load and bending moment about the *y*-axis were added to obtain a total equivalent moment bout the *x*-axis. At that point, the problem was reduced to selection of a trial beam section with bending about the *x*-axis only. This method was most appropriate when significant bending about the *x*-axis existed.

The second Rubinsky method, the MP method, converted the bending moments about the *x*-axis and *y*-axis into equivalent axial loads. In a similar manner to the PM_X method, values of the converted bending moment about the *x*- and *y*-axes were added to the original axial load to obtain an overall equivalent axial load. This method reduced the problem to the selection of a column shape as a trial section.

Later, Burgett (1973) offered a similar method that used tabulated coefficients m and U to convert the bending moments about the *x*- and *y*-axes to equivalent axial loads $M_x m$ and $M_y mU$. Then a trial section was selected from the column design tables of Part 4 of the AISC *Steel Construction Manual* (2023), hereafter referred to as the AISC *Manual*, that could carry a hypothetical effective load, P_{eff}, equal to the original axial load, P_o, plus the equivalent axial loads for bending about the *x*- and *y*-axes.

$$P_{eff} = P_o + M_x m + M_y mU \quad (2)$$

This trial section would be checked for compliance with provisions of the AISC *Specification* Chapter H using the original combined forces. This process would be repeated until a satisfactory section is obtained.

Uang et al. (1990) observed that when using the LRFD method, the Burgett method resulted in "significantly understressed" or overdesigned members. The authors offered new equations and tabulated values for m and U for use with the LRFD method. In the development of their equations and values for m and U, the authors stated, "…the unbraced length L_b of the compression flange is conservatively assumed equal to the effective length of the column." In other words, $L_b = L_{cx} = L_{cy}$. This assumption deserves a discussion.

L_x and L_y are the laterally unbraced lengths of the member for flexural buckling about the *x*- and *y*-axes under column action. To brace the member for this condition, it is necessary to prevent lateral displacement of the member in the appropriate direction and prevent flexural buckling where the member is braced. Effective lengths L_{cx} and L_{cy} are the products of the appropriate K and L; that is, $L_{cx} = K_x L_x$ and $L_{cy} = K_y L_y$.

On the other hand, L_b is the laterally unbraced length of the member in flexure. To brace a member to resist lateral torsional buckling, it is necessary to either restrain the member from twist or prevent lateral displacement and thus prevent bending about the *y*-axis at the point where bracing occurs. Therefore, bracing a member to prevent flexural buckling about the *y*-axis at a particular point will automatically brace the member for lateral torsional buckling at the same location; namely, always $L_b = L_y$.

If $K_y > 1.0$, such as a beam-column in an unbraced frame, then $L_b < L_{cy} = K_y L_y$, and the assumption $L_b = L_{cy}$ in selecting a shape based on L_{cy} will indeed be conservative. However, if $K_y < 1.0$, then $L_b > L_{cy} = K_y L_y$, and the assumption $L_b = L_{cy}$ will be unconservative. If $K_y = 1.0$, then $L_b = L_{cy} = K_y L_y$. There is no such relationship between L_b and L_x (or L_{cx}).

In summary, there is more to the relationship between L_b and L_c (specifically L_{cy}), and a blanket statement assuming L_b and L_c are equal is a conservative assumption that may not always hold.

The Burgett (1973) method and its variations presented by Uang et al. (1990) have been used the longest and remain the most popular method.

In 2000, a new approach and aids for design of steel beam-columns using the LRFD load combinations was presented (Aminmansour, 2000). The method converted AISC *Specification* Equations H1-1a and H1-1b to the following.

When $bP_u \geq 0.20$

$$bP_u + mM_{ux} + nM_{uy} \leq 1.0 \quad (3)$$

When $bP_u < 0.20$

$$0.5bP_u + (9/8)(mM_{ux} + nM_{uy}) \le 1.0 \quad (4)$$

where

$$b = \frac{1}{\phi_c P_n} \quad (5)$$

$$m = \frac{8}{9\phi_b M_{nx}} \quad (6)$$

$$n = \frac{8}{9\phi_b M_{ny}} \quad (7)$$

Tables were generated with values of b, m, and n for all W-shapes with $F_y = 50$ ksi.

Tabulated values of b, m, and n are all exact, taking into consideration all applicable limit states for compression and flexure about the x- and y-axes. Criteria such as width-to-thickness ratios of cross-sectional elements, L_b versus L_p and L_r were already accounted for. Further, L_c and L_b need not be equal. The tables developed covered a wide range of L_c and L_b values.

The method and aids presented in Aminmansour (2000) allow the designer to use sections of any nominal depth as beam-columns rather than being limited to column sections only. Further, there was no need for repeated computations of strength properties. As another benefit of the method, the designer could judge the effectiveness of the section under consideration by observing the values of b, m, and n. Further, tabulated values of b, m, and n and Equations 5, 6, and 7 could be used to obtain other information such as $\phi_c P_n$, $\phi_b M_{nx}$, $\phi_b M_{ny}$, $\phi_b M_{px}$, and $\phi_b M_{py}$ for a range of L_c and L_b for all W-shapes. The paper also presented aids for selecting initial trial sections. An expanded version of the same method and design aids for selecting trial sections was published later (Aminmansour, 2004).

Keil (2000) developed a graphical method using interaction diagrams that could be used for checking a trial section for compliance with the AISC *Specification*. This method is developed for $L_b = L_c = 12$ ft, $C_b = 1.0$, and members under consideration must be subject to axial compression and bending about x-axis only. Conversion factors use linear transformation to convert compressive and flexural strength for values of L_b and L_c other than 12 ft. The method applies to W-shapes typically used as columns ranging from W6 to W14.

Aminmansour (2006) presented a new method and aids for design of structural steel sections subject to tension and bending. The method and aids for tension and bending were very similar to those of compression and bending described previously (Aminmansour, 2000). Equations and design aids developed by Aminmansour (2000, 2006) and were adopted by AISC and included in the third edition of AISC *Manual* Part Six (2001). This was the first time the AISC *Manual* had a part dedicated to design of members subject to combined forces.

Hosur and Augustine (2007) built on the work done previously by Keil (2000) offering a method for incorporating $C_b > 1.0$ in the approach developed earlier by Keil. The authors use design aids developed by Aminmansour (2004) for selection of an efficient section.

In 2009, a method for incorporating C_b for design of members subject to compression and bending, tension and bending, or biaxial bending using AISC *Manual* Table 6-1 was developed (Aminmansour, 2009) and included in the 14th Edition of the AISC *Manual* (AISC, 2011).

Sa'adat and Banan (2014) developed a graphical design aid for selecting the lightest W-shape subject to combined forces. The charts developed along with conversion equations and interpolation allow the designer to select the lightest trial W-shape for a range of L_b, L_c, M_{cx}, and M_{cy}.

Reynolds and Uang (2019) offered a modified version of the equivalent axial load method, originally developed by Burgett (1973) and later refined by Uang et al. (1990), using the following equations.

When $P_r/P_c \ge 0.20$

$$P_{eq} = P_r + mM_{rx} + muM_{ry} \le P_c \quad (8)$$

When $P_r/P_c < 0.20$

$$P_{eq} = \frac{P_r}{2} + \frac{9}{8}mM_{rx} + \frac{9}{8}muM_{ry} \le P_c \quad (9)$$

The authors provide tabulated average values of m and u for wide-flange nominal depths W8 to W36 based on values of L_c ranging from 8 ft and higher, at 2 ft increments. Tables for modified values of m and u include one set for $C_b = 1.0$ and another set of values for what the authors call high moment gradient cases. The authors also offer an innovative equation for selecting a nominal depth for the member based on the applied forces. This method requires $L_b = KL = L_c$. As noted earlier about similar methods, this assumption is indeed conservative if $L_b \le KL = L_c$, otherwise the results will be unconservative. Table 5 presented later in this article summarizes the different methods and their characteristics.

The 15th Edition of the AISC *Manual* (AISC, 2017) includes Table 6-1, also referred to as the "super table," that offers direct available strengths in compression, tension, shear, and flexure about x- and y-axes. Tabulated values are exact and consider all applicable limit states with the exception of using $A_e = 0.75A_g$ for the tensile rupture strength, similar to the assumption made in AISC *Manual* Table 5-1.

AISC *Manual* Table 6-1 can be used for design of beams, columns, and tension members, as well as members subject to combined forces. The table may be used for a wide range of L_b and L_c values. Aminmansour (2017) describes the features and uses of this AISC *Manual* table.

DEVELOPMENT OF THE NEW METHOD AND DESIGN AIDS

Design of W-shape members subjected to combined forces is an iterative process in which a trial section is chosen and checked for compliance with AISC *Specification* Equation H1-1a or H1-1b using available strength values from AISC *Manual* Table 6-1. The process of checking trial sections continues until a desired section is found. The objective, however, is to begin with a trial section from AISC *Manual* Table 6-1 that has available strengths close to the final section and check that section for compliance with AISC *Specification* Equation H1-1a or H1-1b. Note that regardless of which one of Equations H1-1a and H1-1b applies, these equations have three components: axial load component (first term), bending about the x-axis (second term), and bending about the y-axis (third term).

AISC *Manual* Table 6-1 is very helpful for checking for compliance of a trial section with provisions of the AISC *Specification*. However, arriving at a trial section that is most appropriate for the given combined forces and as close to the final selection as possible remains a challenge. This is due to the interaction between axial force and bending moments about the x- and y-axes. There are at least two, potentially three, variables that need to be established in advance of selecting a trail section: the needed available strengths P_c, M_{cx}, and M_{cy}. A method that would help come up with estimates for values for these variables in order to select a good trial section would be helpful.

The method presented here relies on using approximate (average) values for the available strengths for the two less dominant forces (smaller values) and a more educated estimate for the available strength of the more dominant force in order to get estimate values for P_c, M_{cx}, and M_{cy}.

At this point in the process, we are strictly looking at numerical values of the forces; namely, values of the required axial force (tension or compression) and bending moment about the x- and y-axes. The objective is to select a trial section that gives a value of equal to or less than but as close to 1.0 as possible for the interaction equation. The largest required force will have a bigger impact on the value of the interaction equation. That force is referred to as the most dominant force.

Of the three variables needed to select a trial section, normally M_{cy} has the least numerical impact on the overall value of the interaction equation. Therefore, using an estimate such as the average value of M_{cy} for all shapes within the same nominal depth seems reasonable. Recall that M_{cy} is a cross-sectional property for W-shape flexural members and only depends on whether the section is compact or noncompact. Specifically, lateral torsional buckling does not apply to bending of W-shape flexural members bent about their weak axis, and thus, there is no unbraced length to use. The available strength M_{cy} of a W-shape is a single number and depends on whether the section is compact or not.

For the two remaining applied forces—axial force and bending moment about the x-axis—often one is more dominant or larger than the other. Therefore, using an average value for the available strength for the force that is less dominant also seems reasonable. If the numerical value of the applied axial force (tension or compression) is more dominant or larger than the numerical value of the bending about the x-axis, the designer can use the average value of M_{cx} for W-shapes within the same nominal depth over the same unbraced length to obtain an estimate for M_{cx}. On the other hand, if bending about the x-axis is more dominant or larger, the designer can use the average value of P_c for W-shapes of the same nominal depth and for the same effective length to obtain an estimate for P_c. By limiting the averages to the shapes within the same nominal depth and the same unbraced length as the design problem, we lower the error in our calculations.

An estimated value for the third available strength related to the most dominant or the largest force can be found by inserting the estimates for the other two available strengths found earlier in the interaction equation while setting the value of the interaction equation equal to unity (1.0). The process of calculating an estimate for the available strength for the most dominant force using the interaction equation will lead to a smaller error in the outcome.

The procedure of using average values for two variables to calculate an estimate for the third variable may seem overly simplistic. However, as will be illustrated in the examples that follow, the method works well, leading to an optimum section in two or three tries with each taking very little time when using AISC *Manual* Table 6-1.

Tables 1, 2, 3, and 4 were developed using a spreadsheet to calculate the average available strengths discussed earlier. Tabulated values are listed for W-shapes with ASTM A992/A992M (2022) (F_y = 50 ksi and F_u = 65 ksi) and for all nominal depths. Given that at this point we are interested in average values of available strengths, it was assumed that all W-shapes are nonslender for compression and that all W-shapes are compact for flexure. In addition, only two significant figures were used in the development of the tables. Finally, it is assumed that the designer has established a desired nominal depth for the design at this point. The design aid tables developed are as follows.

- Table 1: Average values of P_c in compression ($\phi_c P_n$ for LRFD and P_n/Ω_c for ASD)
- Table 2: Average values of M_{cx} ($\phi_b M_{nx}$ for LRFD and M_{nx}/Ω_b for ASD)
- Table 3: Average values of M_{cy} ($\phi_b M_{ny}$ for LRFD and M_{ny}/Ω_b for ASD)
- Table 4: Average values of P_c in tension ($\phi_t P_n$ for LRFD and P_n/Ω_t for ASD)

F_y = 50 ksi

Table 1
Average Available Compressive Strength $(P_c)_{avg}$, kips
W-Shapes

	Effective Length, L_c (ft)															
	0		2		4		6		8		10		12		14	
	ASD	LRFD	ASD	LRFD	ASD	LRFD	ASD	LRFD	ASD	LRFD	ASD	LRFD	ASD	LRFD	ASD	LRFD
Nominal Depth	P_n/Ω_c	$\phi_c P_n$	P_n/Ω_c	$\phi_c P_n$	P_n/Ω_c	$\phi_c P_n$	P_n/Ω_c	$\phi_c P_n$	P_n/Ω_c	$\phi_c P_n$	P_n/Ω_c	$\phi_c P_n$	P_n/Ω_c	$\phi_c P_n$	P_n/Ω_c	$\phi_c P_n$
W44	2500	3700	2500	3700	2400	3700	2400	3600	2300	3500	2300	3400	2200	3300	2100	3100
W40 (> 200 lb)	3400	5200	3400	5100	3400	5100	3300	5000	3300	4900	3200	4800	3100	4600	3000	4400
W40 (< 200 lb)	2200	3300	2200	3300	2200	3300	2100	3200	2000	3000	1900	2900	1800	2700	1600	2500
W36 (> 400 lb)	5100	7600	5000	7600	5000	7500	4900	7400	4900	7300	4700	7100	4600	6900	4400	6700
W36 (> 200 lb and < 400 lb)	2500	3700	2500	3700	2500	3700	2400	3600	2400	3500	2300	3400	2200	3300	2100	3100
W36 (< 200 lb)	1500	2200	1500	2200	1400	2100	1400	2100	1300	2000	1200	1900	1200	1700	1100	1600
W33	2000	3000	2000	3000	2000	3000	2000	2900	1900	2900	1800	2800	1800	2600	1700	2500
W30	1800	2700	1800	2700	1800	2600	1700	2600	1700	2500	1600	2400	1500	2300	1400	2200
W27	2000	2900	1900	2900	1900	2900	1900	2800	1800	2700	1800	2600	1700	2500	1600	2400
W24	1500	2200	1500	2200	1500	2200	1400	2100	1400	2000	1300	1900	1200	1800	1100	1700
W21	1100	1600	1100	1600	1000	1600	1000	1500	950	1400	900	1400	830	1300	770	1200
W18	1200	1700	1100	1700	1100	1700	1100	1600	1000	1500	970	1500	900	1400	830	1200
W16	500	740	490	730	470	710	440	660	410	610	370	550	320	480	280	420
W14 (> 300 lb)	4300	6400	4300	6400	4300	6400	4200	6300	4200	6200	4100	6100	4000	6000	3900	5800
W14 (< 300 lb)	760	1100	750	1100	740	1100	720	1100	690	1000	660	990	630	940	590	880
W12 (> 200 lb)	1000	1600	1000	1600	1000	1500	990	1500	950	1400	910	1400	860	1300	810	1200
W12 (< 200 lb)	640	970	640	960	620	940	600	900	570	860	540	810	510	760	540	810
W10	430	640	420	630	410	610	380	570	360	540	330	490	300	450	300	450
W8	280	420	270	410	260	390	240	360	220	330	190	290	170	250	140	220
W6	130	200	130	190	120	180	100	150	82.0	120	65	97	50	76	39	58
W5	150	230	150	230	140	210	120	180	100	150	80	120	60	90	44	66
W4	120	170	110	170	97	150	79	120	59	88	40	60	28	42	20	31

Table 1 (continued)
Average Available Compressive Strength $(P_c)_{avg}$, kips
W-Shapes

$F_y = 50$ ksi

	Effective Length, L_c (ft)															
	16		18		20		22		24		26		28		30	
	ASD	LRFD	ASD	LRFD	ASD	LRFD	ASD	LRFD	ASD	LRFD	ASD	LRFD	ASD	LRFD	ASD	LRFD
Nominal Depth	P_n/Ω_c	$\phi_c P_n$	P_n/Ω_c	$\phi_c P_n$	P_n/Ω_c	$\phi_c P_n$	P_n/Ω_c	$\phi_c P_n$	P_n/Ω_c	$\phi_c P_n$	P_n/Ω_c	$\phi_c P_n$	P_n/Ω_c	$\phi_c P_n$	P_n/Ω_c	$\phi_c P_n$
W44	2000	3000	1900	2800	1700	2600	1600	2400	1500	2200	1400	2100	1200	1900	1100	1700
W40 (> 200 lb)	2800	4200	2700	4000	2500	3800	2400	3500	2200	3300	2000	3000	1900	2800	1700	2600
W40 (< 200 lb)	1500	2200	1300	2000	1200	1800	1000	1600	900	1300	770	1200	670	1000	580	880
W36 (> 400 lb)	4300	6400	4100	6100	3900	5800	3700	5500	3500	5200	3300	4900	3000	4600	2800	4200
W36 (> 200 lb and < 400 lb)	2000	3000	1900	2800	1800	2600	1600	2400	1500	2300	1400	2100	1300	1900	1200	1700
W36 (< 200 lb)	950	1400	850	1300	750	1100	650	970	550	830	470	710	410	610	350	530
W33	1600	2400	1500	2200	1400	2100	1300	1900	1200	1700	1100	1600	970	1500	880	1300
W30	1300	2000	1300	1900	1200	1700	1100	1600	970	1500	880	1300	800	1200	720	1100
W27	1500	2200	1400	2100	1300	1900	1200	1800	1100	1600	970	1500	880	1300	790	1200
W24	1100	1600	970	1500	890	1300	800	1200	790	1200	710	1100	630	950	560	830
W21	700	1100	630	950	570	860	560	840	530	790	470	700	430	650	420	630
W18	760	1100	680	1000	610	920	620	930	550	820	480	720	450	680	460	690
W16	240	360	210	310	210	320	180	270	160	230	140	220	200	300	180	260
W14 (> 300 lb)	3800	5600	3600	5400	3500	5200	3300	5000	3200	4700	3000	4500	2800	4200	2700	4000
W14 (< 300 lb)	550	830	540	810	530	790	490	730	450	680	490	730	450	670	410	610
W12 (> 200 lb)	750	1100	740	1100	720	1100	660	1000	610	910	690	1000	630	940	560	850
W12 (< 200 lb)	530	790	480	730	440	660	400	600	360	540	380	560	330	500	290	440
W10	310	460	270	410	240	360	210	310	220	330	190	290	160	250	140	220
W8	160	230	130	200	110	160	110	160	89.0	130	76	110	79	120	68	100
W6	45	67	42	64	34	52	28	43	24	36						
W5	34	51	27	40	22	33										
W4	16	23														

Table 2
Average Available Flexural Strength about x-Axis $(M_{cx})_{avg}$, kip-ft
W-Shapes

$F_y = 50$ ksi

	Unbraced Length, L_b (ft)															
	0		2		4		6		8		10		12		14	
	ASD	LRFD	ASD	LRFD	ASD	LRFD	ASD	LRFD	ASD	LRFD	ASD	LRFD	ASD	LRFD	ASD	LRFD
Nominal Depth	M_{nx}/Ω_b	$\phi_b M_{nx}$	M_{nx}/Ω_b	$\phi_b M_{nx}$	M_{nx}/Ω_b	$\phi_b M_{nx}$	M_{nx}/Ω_b	$\phi_b M_{nx}$	M_{nx}/Ω_b	$\phi_b M_{nx}$	M_{nx}/Ω_b	$\phi_b M_{nx}$	M_{nx}/Ω_b	$\phi_b M_{nx}$	M_{nx}/Ω_b	$\phi_b M_{nx}$
W44	3400	5100	3400	5100	3400	5100	3400	5100	3400	5100	3400	5100	3400	5100	3300	4900
W40 (> 200 lb)	4500	6700	4500	6700	4500	6700	4500	6700	4500	6700	4500	6700	4500	6700	4400	6600
W40 (< 200 lb)	2700	4100	2700	4100	2700	4100	2700	4100	2700	4100	2700	4000	2600	3800	2500	3700
W36 (> 400 lb)	6400	9600	6400	9600	6400	9600	6400	9600	6400	9600	6400	9600	6400	9600	6400	9600
W36 (> 200 lb and < 400 lb)	3000	4500	3000	4500	3000	4500	3000	4500	3000	4500	3000	4400	2900	4400	2900	4300
W36 (< 200 lb)	1600	2400	1600	2400	1600	2400	1600	2400	1600	2400	1600	2400	1500	2200	1400	2100
W33	2200	3400	2200	3400	2200	3400	2200	3400	2200	3400	2200	3300	2200	3300	2200	3200
W30	1800	2700	1800	2700	1800	2700	1800	2700	1800	2700	1800	2700	1800	2600	1700	2600
W27	1800	2700	1800	2700	1800	2700	1800	2700	1800	2700	1800	2700	1800	2700	1700	2600
W24	1200	1800	1200	1800	1200	1800	1200	1800	1200	1800	1200	1800	1200	1800	1200	1700
W21	770	1200	770	1200	770	1200	770	1200	760	1100	750	1100	720	1100	700	1000
W18	740	1100	740	1100	740	1100	740	1100	730	1100	720	1100	700	1100	680	1000
W16	270	400	270	400	270	400	260	390	250	380	240	360	230	340	210	320
W14 (> 300 lb)	2600	3900	2600	3900	2600	3900	2600	3900	2600	3900	2600	3900	2600	3900	2600	3900
W14 (< 300 lb)	370	560	370	560	370	560	370	560	370	550	360	550	360	540	350	530
W12 (> 200 lb)	510	760	510	760	510	760	500	760	500	750	500	740	490	730	480	720
W12 (< 200 lb)	280	420	280	420	280	420	280	420	270	410	270	410	270	400	260	390
W10	150	230	150	230	150	220	150	220	150	220	140	210	140	200	130	200
W8	78	120	78	120	78	120	76	110	74	110	70	110	67	100	64	96
W6	27	41	27	41	27	40	26	38	24	36	22	33	20	30	18	27
W5	27	40	27	40	27	40	26	38	24	37	23	35	22	33	21	31
W4	16	24	16	24	16	23	15	22	14	21	13	20	12	19	12	17

Table 2 (continued)
Average Available Flexural Strength about x-Axis $(M_{cx})_{avg}$, kip-ft
W-Shapes

$F_y = 50$ ksi

	Unbraced Length, L_b (ft)															
	16		18		20		22		24		26		28		30	
	ASD	LRFD	ASD	LRFD	ASD	LRFD	ASD	LRFD	ASD	LRFD	ASD	LRFD	ASD	LRFD	ASD	LRFD
Nominal Depth	M_{nx}/Ω_b	$\phi_b M_{nx}$	M_{nx}/Ω_b	$\phi_b M_{nx}$	M_{nx}/Ω_b	$\phi_b M_{nx}$	M_{nx}/Ω_b	$\phi_b M_{nx}$	M_{nx}/Ω_b	$\phi_b M_{nx}$	M_{nx}/Ω_b	$\phi_b M_{nx}$	M_{nx}/Ω_b	$\phi_b M_{nx}$	M_{nx}/Ω_b	$\phi_b M_{nx}$
W44	3200	4800	3100	4600	3000	4400	2900	4300	2800	4100	2600	4000	2500	3800	2400	3600
W40 (> 200 lb)	4300	6400	4200	6300	4100	6100	4000	6000	3900	5800	3800	5700	3700	5500	3600	5400
W40 (< 200 lb)	2400	3500	2300	3400	2200	3200	2100	3100	2000	2900	1900	2800	1700	2600	1600	2400
W36 (> 400 lb)	6300	9500	6200	9300	6100	9200	6100	9100	6000	8900	5900	8800	5800	8700	5700	8600
W36 (> 200 lb and < 400 lb)	2800	4200	2700	4100	2600	4000	2600	3800	2500	3700	2400	3600	2300	3500	2200	3300
W36 (< 200 lb)	1400	2000	1300	1900	1200	1800	1100	1700	1100	1600	970	1500	880	1300	780	1200
W33	2100	3100	2000	3000	2000	2900	1900	2800	1800	2700	1700	2600	1700	2500	1600	2400
W30	1700	2500	1600	2400	1600	2300	1500	2200	1400	2100	1400	2100	1300	2000	1300	1900
W27	1700	2500	1700	2500	1600	2400	1600	2300	1500	2300	1500	2200	1400	2100	1400	2100
W24	1100	1700	1100	1600	1000	1600	1000	1500	970	1500	940	1400	910	1400	880	1300
W21	670	1000	640	960	620	930	590	890	570	850	550	820	530	790	510	760
W18	660	990	640	960	620	930	600	900	590	880	570	850	550	830	540	800
W16	200	300	180	270	170	250	160	240	150	220	140	210	130	190	120	180
W14 (> 300 lb)	2600	3900	2600	3800	2500	3800	2500	3800	2500	3800	2500	3800	2500	3700	2500	3700
W14 (< 300 lb)	340	510	330	500	320	480	310	470	300	460	290	440	290	430	280	420
W12 (> 200 lb)	470	700	460	690	450	680	440	660	440	650	430	640	420	630	410	620
W12 (< 200 lb)	250	380	240	370	240	360	230	350	220	340	220	330	210	320	210	310
W10	130	190	120	180	120	180	110	170	110	160	110	160	100	150	98	150
W8	61	91	58	87	55	83	53	79	50	75	48	72	46	68	44	65
W6	16	25	15	22	14	20	12	19	11	17	10	16	10	14	8.9	13
W5	20	30	18	28	17	26	16	24	15	22	14	20	13	19	12	17
W4	11	16	10	15	9.2	14	8.3	13	7.6	11	7.0	11	6.5	10	6.1	9.1

Table 3
Average Available Flexural Strength about *y*-Axis $(M_{cy})_{avg}$, kip-ft
W-Shapes

Shape	ASD	LRFD
	M_{ny}/Ω_b	$\phi_b M_{ny}$
W44	490	730
W40 (> 200 lb)	750	1100
W40 (< 200 lb)	330	490
W36 (> 400 lb)	1300	1900
W36 (> 200 lb and < 400 lb)	520	780
W36 (< 200 lb)	200	300
W33	400	610
W30	340	520
W27	380	570
W24	270	400
W21	170	260
W18	190	280
W16	60	90
W14 (> 300 lb)	1300	1900
W14 (< 300 lb)	160	240
W12 (> 200 lb)	210	320
W12 (< 200 lb)	120	180
W10	62	93
W8	32	48
W6	10	16
W5	13	19
W4	7.3	11

Table 4
Average Available Tensile Strength $(P_c)_{avg}$, kips
W-Shapes

Shape	ASD	LRFD
	P_{ny}/Ω_t	$\phi_t P_{ny}$
W44	2200	3400
W40 (> 200 lb)	3100	4700
W40 (< 200 lb)	2000	3000
W36 (> 400 lb)	4600	6900
W36 (> 200 lb and < 400 lb)	2300	3400
W36 (< 200 lb)	1300	2000
W33	1800	2800
W30	1600	2400
W27	1800	2600
W24	1400	2000
W21	970	1500
W18	1000	1600
W16	450	670
W14 (> 300 lb)	3900	5800
W14 (< 300 lb)	690	1000
W12 (> 200 lb)	940	1400
W12 (< 200 lb)	580	880
W10	390	580
W8	250	380
W6	120	180
W5	140	210
W4	100	150

PROCEDURE FOR USING THE PROPOSED METHOD AND TABLES

AISC *Specification* Equations H1-1a and H1-1b apply to members subject to tension and bending as well as subject to compression and bending. Only the values of the first term in the equation are affected if the axial load is tension or compression.

Ideally, the value of the applicable AISC *Specification* interaction Equation H1-1a or H1-1b will be unity as shown here.

When $\frac{P_r}{P_c} \geq 0.20$

$$\frac{P_r}{P_c} + \frac{8}{9}\left(\frac{M_{rx}}{M_{cx}} + \frac{M_{ry}}{M_{cy}}\right) = 1.0 \quad (10)$$

When $\frac{P_r}{P_c} < 0.20$

$$\frac{P_r}{2P_c} + \left(\frac{M_{rx}}{M_{cx}} + \frac{M_{ry}}{M_{cy}}\right) = 1.0 \quad (11)$$

For biaxial bending ($P_r = 0$, $P_r/P_c = 0 < 0.20$), the equivalent for AISC *Specification* Equation H1-1b becomes the following.

$$\frac{M_{rx}}{M_{cx}} + \frac{M_{ry}}{M_{cy}} = 1.0 \quad (12)$$

These equations will be used in the following procedure for design.

If it is not obvious which of Equation 10 or 11 applies, it is reasonable to begin with Equation 10 because this equation is applicable in many common situations. When checking each trial section, the appropriate equation will be used as illustrated in the following examples. The new design procedure may be summarized as follows.

1. Combined axial load (tension or compression) and bending when the numerical value of the required axial strength, P_r, is larger than the value of the required flexural strength about the x-axis, M_{rx}; namely, $|P_r| > |M_{rx}|$.
   a. Look up the average available flexural strength $(M_{cx})_{avg}$ from Table 2 based on L_b.
   b. If bending about y-axis is present, look up the average available flexural strength about y-axis $(M_{cy})_{avg}$ from Table 3.
   c. Use results of steps a and b and Equation 10 or 11 to solve for an estimate for the available axial strength $(\phi_c P_n$ or $P_n/\Omega_c)_{est}$.
   d. Choose a trial section from AISC *Manual* Table 6-1 using the results of steps a, b, and c while paying closer attention to sections with higher available axial strengths.
   e. Check section using AISC *Specification* Equation H1-1a or H1-1b.

The flowcharts of Figures 1 and 2 illustrate this procedure.

2. Combined axial load (tension or compression) and bending when the numerical value of the required flexural strength about the x-axis, M_{rx}, is larger than the value of the required axial strength, P_r; namely, $|M_{rx}| > |P_r|$.
   a. Look up the average available axial strength $(P_c)_{avg}$ from Table 1 for compression based on L_c or $(P_c)_{avg}$ from Table 4 for tension.
   b. If bending about y-axis is present, look up the average available flexural strength about y-axis $(M_{cy})_{avg}$ from Table 3.
   c. Use results of steps a and b and Equation 10 or 11 to solve for an estimate for the desired available flexural strength $(\phi_b M_{nx}$ or $M_{nx}/\Omega_b)_{\text{est}}$.
   d. Choose a trial section from AISC *Manual* Table 6-1 using results of steps a, b, and c while paying closer attention to sections with higher available flexural strengths about x-axis.
   e. Check section using AISC *Specification* Equation H1-1a or H1-1b.

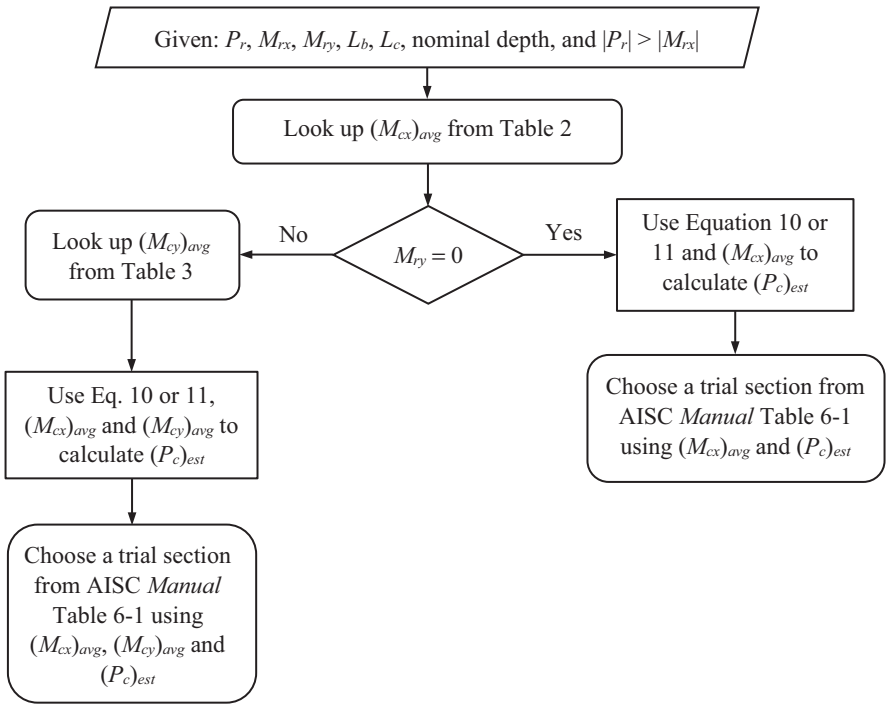

Fig. 1. Flowchart for choosing a trial section for combined compression and bending with large axial load.

The flowcharts of Figures 3 and 4 illustrate this procedure.

3. Biaxial Bending (no axial force)

   a. Look up the average available flexural strength for bending about the *y*-axis $(M_{cy})_{avg}$ from Table 3.

   b. Use result of step a and Equation 12 to solve for an estimate for the available flexural strength $(M_{cx})_{est}$.

   c. Select a trial section from AISC *Manual* Table 6-1 using results of steps a and b while paying closer attention to sections with higher available flexural strength about the *x*-axis.

   d. Check section using AISC *Specification* Equation H1-1b.

The flowchart of Figure 5 illustrates this procedure.

Additional Notes on Use of the Proposed Method and Tables

The following notes are offered for using the proposed method and tables.

1. The proposed procedure converges quickly to the desired section. Ordinarily, the desired section is attained by checking one or two trial sections. At times, three trial sections may need to be checked. It is rare that four trial sections would need to be checked to attain the desired section.
2. If the values of P_r and M_{rx} are close, use either procedure 1 or 2.
3. To choose a trial section, it is reasonable to interpolate between values of L_c and L_b when using Tables 1 and 2 (see Example 3).
4. Some average available strengths for a certain nominal depth in Tables 1 to 4 are broken down based on weight per foot of the member. If a wrong weight range is assumed, the process still works and converges rapidly (see Example 4).
5. Values of average available tensile strength in Table 4 can be used without knowing whether yielding or rupture strength governs design at this point. Exact available

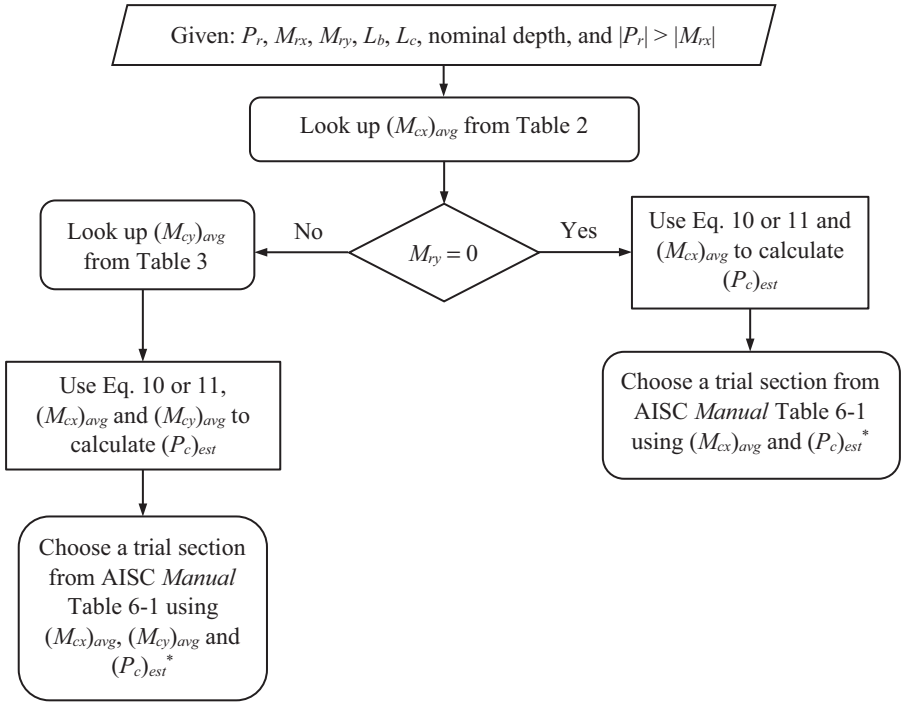

* Consider tensile yielding and tensile rupture available strengths when checking the trial section.

Fig. 2. Flowchart for choosing a trial section for combined tension and bending with large axial load.

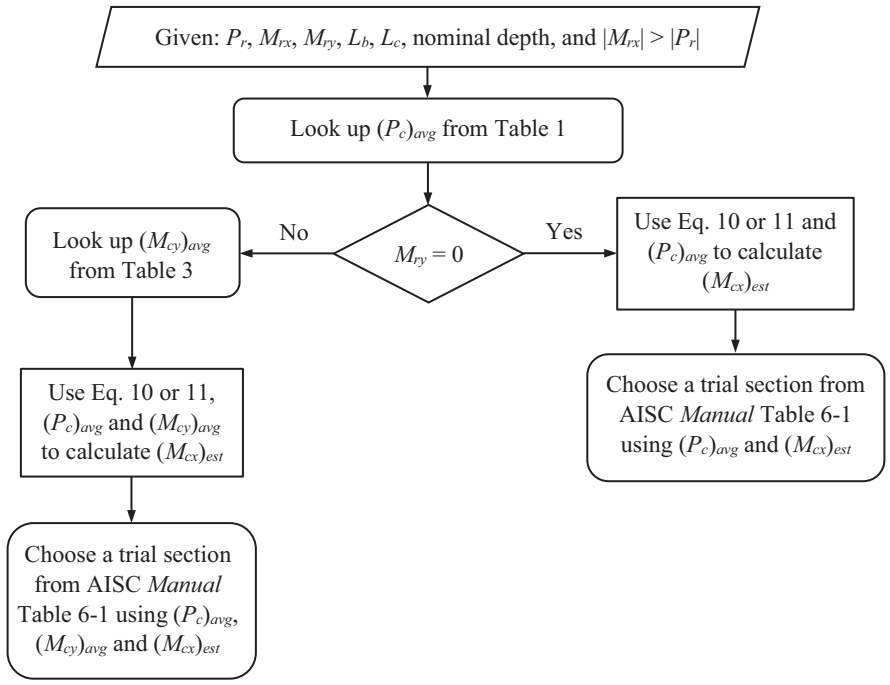

Fig. 3. Flowchart for choosing a trial section for combined compression and bending with large bending moment about the x-*axis.*

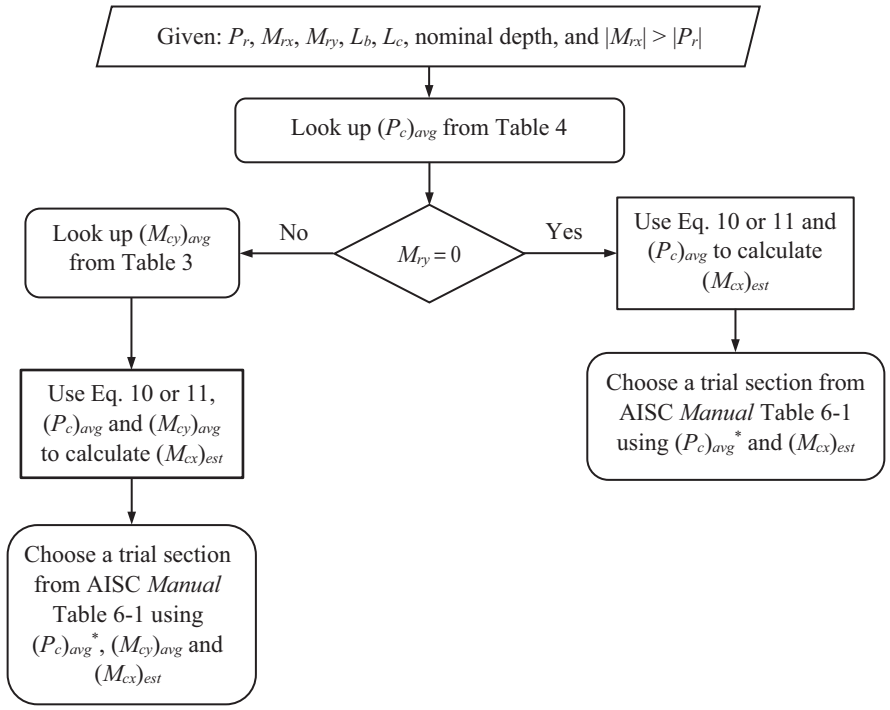

* Consider tensile yielding and tensile rupture available strengths when checking the trial section.

Fig. 4. Flowchart for choosing a trial section for combined tension and bending with large bending moment about the x-*axis.*

strengths for tensile yielding are listed in AISC *Manual* Table 6-1. Available tensile rupture strengths must be calculated based on member connections when checking for compliance with AISC *Specification* provisions regardless of method used to obtain a trial section (see Example 3).

6. When considering a trial section from AISC *Manual* Table 6-1, if each of the available strengths are larger than the average and estimated values, the section will lead to an interaction equation value of less than 1.0 and the shape under consideration is an appropriate trial section for the given conditions. Similarly, if each of the available strengths are smaller than the average and estimated values, the section will lead to an interaction value of greater than 1.0, and the section under consideration is not adequate (see Example 1).
7. At times, a W-shape under consideration from AISC *Manual* Table 6-1 as a trial section will have one available strength larger and one or two smaller than the average and estimated values. The designer may still consider such a trial section since the math for the interaction equation may still result in a value less than or equal to 1.0 (see Example 1).
8. Trial sections must be checked for compliance with AISC *Specification* Equation H1-1a or H1-1b, whichever is appropriate, along with its available strengths. If in choosing a trial section it was assumed that AISC *Specification* Equation H1-1a governs, but indeed AISC *Specification* Equation H1-1b governs, Equation H1-1b must be checked to determine the adequacy of the section (see Example 2).
9. If the required flexural strength about the *y*-axis, M_{ry}, is larger than M_{rx} and P_r, steps 1(a) and 2(a) in the procedure can be adjusted accordingly. Choose a trial section using $(P_c)_{avg}$ and $(M_{cx})_{avg}$, then use AISC *Specification* Equation 10 or 11 to solve for an estimate for the desired available flexural strength $(M_{cy})_{est}$. Select a trial section from AISC *Manual* Table 6-1 based on $(P_c)_{avg}$, $(M_{cx})_{avg}$ and $(M_{cy})_{est}$.

Examples Using the Proposed Method and Design Aids

The focus of this article is on choosing an optimum trial section, not complete design. The following remarks are independent of how the designer chooses a trial section and are not limited to the method and aids proposed here.

Second-order effects must be considered in the design of members subjected to compression and bending (beam-columns). During the process of selecting a trial section, the designer may decide to neglect second-order effects initially. Alternatively, the designer can use estimates for moment amplifications B_1 and B_2 (if applicable) to include some level of second-order effects at this stage. In the end, every trial section must be checked for compliance with all the pertinent provisions of the AISC *Specification*, including second-order effects.

In considering second-order effects, cross-sectional properties of each trial section must be used in calculating P_r, M_{rx}, and M_{ry}. The values of P_r, M_{rx}, and M_{ry} are dependent on the trial section's cross-sectional properties and may be different for one trial section versus another. For example, P-δ effect depends on I_x, which varies from one section to another. However, while choosing a trial section, it may be

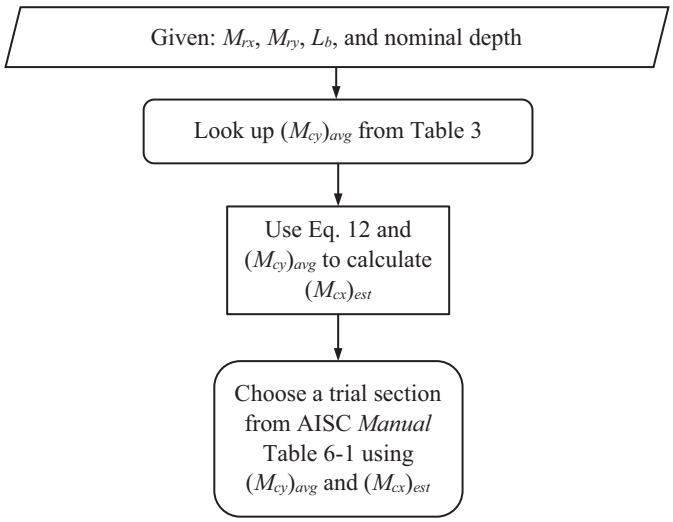

Fig. 5. Flowchart for choosing a trial section for biaxial bending.

reasonable to assume these values do not change between trial sections that are close in size.

The scope of this article does not include second-order effects. Therefore, in the examples that follow, the assumption is made that second-order effects do not change the value of the required strengths P_r, M_{rx}, and M_{ry} for different trial sections.

Example problems that follow are done using the LRFD method. Solutions using the ASD method would be similar except for looking up ASD values from Tables 1 through 4 as well as the ASD versions of Equations 10, 11, and 12.

EXAMPLE 1

Given:

Determine the lightest ASTM A992/A992M W14 section for a beam-column with the following conditions:

$L_b = 10$ ft, $L_c = 14$ ft

$P_u = 600$ kips, $M_{ux} = 170$ kip-ft, $M_{uy} = 40$ kip-ft

Solution:

The numerical value of P_u is larger than that of M_{ux}. Look up the average values for M_{cx} and M_{cy} ($\phi_b M_{nx}$ and $\phi_b M_{ny}$) from Tables 2 and 3, respectively, as follows. Assume member weight is ≤ 200 lb/ft. For $L_b = 10$ ft, $(M_{cx})_{avg} = (\phi_b M_{nx})_{avg} = 550$ kip-ft, and $(M_{cy})_{avg} = (\phi_b M_{ny})_{avg} = 240$ kip-ft.

Use Equation 10 to calculate an estimate for $\phi_c P_n$

$$\frac{P_r}{P_c} + \frac{8}{9}\left(\frac{M_{rx}}{M_{cx}} + \frac{M_{ry}}{M_{cy}}\right) = 1.0 \tag{10}$$

$$\frac{600 \text{ kips}}{(\phi_c P_n)_{est}} + \frac{8}{9}\left(\frac{170 \text{ kip-ft}}{550 \text{ kip-ft}} + \frac{40 \text{ kip-ft}}{240 \text{ kip-ft}}\right) = 1.0$$

Therefore, $(\phi_c P_n)_{est} = 1{,}040$ kips.

From AISC *Manual* Table 6-1, choose a W14 trial section with the following approximate values:

$\phi_c P_n = 1{,}040$ kips ($L_c = 14$ ft), $\phi_b M_{nx} = 550$ kip-ft ($L_b = 10$ ft), and $\phi_b M_{ny} = 240$ kip-ft

Try a W14×90 with $\phi_c P_n = 1{,}030$ kips ($L_c = 14$ ft), $\phi_b M_{nx} = 574$ kip-ft ($L_b = 10$ ft), and $\phi_b M_{ny} = 273$ kip-ft.

Note that this section has a lower $\phi_c P_n$ but higher $\phi_b M_{nx}$ and $\phi_b M_{ny}$ than the target values.

Check the W14×90 for compliance with AISC *Specification* Equation H1-1a or H1-1b.

$$\frac{P_u}{\phi_c P_n} = \frac{600 \text{ kips}}{1{,}030 \text{ kips}} = 0.583 > 0.20$$

Therefore, use AISC *Specification* Equation H1-1a.

$$\frac{P_u}{\phi_c P_n} + \frac{8}{9}\left(\frac{M_{ux}}{\phi_b M_{nx}} + \frac{M_{uy}}{\phi_b M_{ny}}\right) \le 1.0$$

$$0.583 + \frac{8}{9}\left(\frac{170 \text{ kip-ft}}{574 \text{ kip-ft}} + \frac{40 \text{ kip-ft}}{273 \text{ kip-ft}}\right) = 0.976 < 1.0 \quad \textbf{o.k.}$$

The W14×90 is an appropriate trial section.

For a lighter section, try a W14×82 with $\phi_c P_n = 772$ kips ($L_c = 14$ ft), $\phi_b M_{nx} = 511$ kip-ft ($L_b = 10$ ft), and $\phi_b M_{ny} = 168$ kip-ft.

By inspection, a W14×82 is not adequate because all the available strength values are less than what made the interaction equation equal to unity ($\phi_c P_n$ = 772 kips < 1,040 kips, $\phi_b M_{nx}$ = 511 kip-ft < 550 kip-ft, and $\phi_b M_{ny}$ = 168 kip-ft < 240 kip-ft).

Choose a W14×90 (ASTM A992/A992M) as the trial section.

EXAMPLE 2

Given:

Determine the lightest ASTM A992/A992M W18 section for a beam-column with the following conditions:

$L_c = L_b$ = 14 ft

P_u = 170 kips, M_{ux} = 600 kip-ft, M_{uy} = 40 kip-ft

Solution:

The numerical value of M_{ux} is larger than that of P_u. Look up average values for P_c and M_{cy} ($\phi_c P_n$, and $\phi_b M_{ny}$) from Tables 1 and 3, respectively, as follows:

For L_c = 14 ft, $(P_c)_{avg} = (\phi_c P_n)_{avg}$ = 1,200 kips, and $(M_{cy})_{avg} = (\phi_b M_{ny})_{avg}$ = 280 kip-ft

Use Equation 10 to calculate an estimate for $(\phi_b M_{nx})_{est}$.

$$\frac{P_r}{P_c} + \frac{8}{9}\left(\frac{M_{rx}}{M_{cx}} + \frac{M_{ry}}{M_{cy}}\right) = 1.0 \tag{10}$$

$$\frac{170 \text{ kips}}{1{,}200 \text{ kips}} + \frac{8}{9}\left[\frac{600 \text{ kips}}{(\phi_b M_{nx})_{est}} + \frac{40 \text{ kip-ft}}{280 \text{ kip-ft}}\right] = 1.0$$

Therefore, $(\phi_b M_{nx})_{est}$ = 729 kip-ft.

From AISC *Manual* Table 6-1, choose a trial W18 section with the following approximate values:

$\phi_c P_n$ = 1,200 kips (L_c = 14 ft), $\phi_b M_{nx}$ = 729 kip-ft (L_b = 14 ft), and $\phi_b M_{ny}$ = 280 kip-ft

Try a W18×119 with $\phi_c P_n$ = 1,190 kips (L_c = 14 ft), $\phi_b M_{nx}$ = 914 kip-ft (L_b = 14 ft), and $\phi_b M_{ny}$ = 259 kip-ft.

$$\frac{P_u}{\phi_c P_n} = \frac{170 \text{ kips}}{1{,}190 \text{ kips}} = 0.143 < 0.20$$

Use AISC *Specification* Equation H1-1b. Note that originally it was assumed that Equation H1-1a governed.

$$\frac{P_u}{2(\phi_c P_n)} + \left(\frac{M_{ux}}{\phi_b M_{nx}} + \frac{M_{uy}}{\phi_b M_{ny}}\right) \le 1.0$$

$$\frac{0.143}{2} + \left(\frac{600 \text{ kip-ft}}{914 \text{ kip-ft}} + \frac{40.0 \text{ kip-ft}}{259 \text{ kip-ft}}\right) = 0.882 < 1.0 \quad \textbf{o.k.}$$

For a lighter section, try a W18×106 with $\phi_c P_n$ = 1,050 kips (L_c = 14 ft), $\phi_b M_{nx}$ = 795 kip-ft (L_b = 14 ft), and $\phi_b M_{ny}$ = 227 kip-ft.

Check the W18×106 for compliance with AISC *Specification* Equation H1-1a or H1-1b.

$$\frac{P_u}{\phi_c P_n} = \frac{170 \text{ kips}}{1{,}050 \text{ kips}} = 0.162 < 0.20$$

Therefore, use AISC *Specification* Equation H1-1b. Note that originally it was assumed that AISC *Specification* Equation H1-1a controlled.

$$\frac{P_u}{2(\phi_c P_n)}+\left(\frac{M_{ux}}{\phi_b M_{nx}}+\frac{M_{uy}}{\phi_b M_{ny}}\right)\le 1.0$$

$$\frac{0.162}{2}+\left(\frac{600\text{ kip-ft}}{795\text{ kip-ft}}+\frac{40.0\text{ kip-ft}}{227\text{ kip-ft}}\right)=1.01>1.0 \quad \textbf{n.g.}$$

Choose a W18×119 (ASTM A992/A992M) as the trial section.

EXAMPLE 3

Given:

Determine the lightest ASTM A992/A992M W10 section connected as shown in Figure 6.

$L_b = 15$ ft

$d_b = ⅞$ in. bolts at 3 in. o.c.

$P_u = 300$ kips in tension, $M_{ux} = 85$ kip-ft, $M_{uy} = 25$ kip-ft

Solution:

The numerical value of P_u is larger than that of M_{ux}. Look up the average values for M_{cx} and M_{cy} ($\phi_b M_{nx}$, and $\phi_b M_{ny}$) from Tables 2 and 3, respectively, as follows. Note that it is reasonable at this point to interpolate between values of L_b in Table 2 and 3.

At $L_b = 14$ ft, $(M_{cx})_{avg} = (\phi_b M_{nx})_{avg} = 200$ kip-ft, and at $L_b = 16$ ft, $(M_{cx})_{avg} = (\phi_b M_{nx})_{avg} = 190$ kip-ft.

Therefore, at $L_b = 15$ ft, $(M_{cx})_{avg} = (\phi_b M_{nx})_{avg} = 195$ kip-ft (by interpolation). Also, $(M_{cy})_{avg} = (\phi_b M_{ny})_{avg} = 93.0$ kip-ft from Table 3.

Use Equation 10 to calculate an estimate for $\phi_t P_n$.

$$\frac{P_r}{P_c}+\frac{8}{9}\left(\frac{M_{rx}}{M_{cx}}+\frac{M_{ry}}{M_{cy}}\right)=1.0 \tag{10}$$

$$\frac{300\text{ kips}}{(\phi_t P_n)_{est}}+\frac{8}{9}\left(\frac{85.0\text{ kip-ft}}{195\text{ kip-ft}}+\frac{25.0\text{ kip-ft}}{93.0\text{ kip-ft}}\right)=1.0$$

Therefore, $(\phi_t P_n)_{est} = 803$ kips.

From AISC *Manual* Table 6-1, choose a W10 trial section with the following approximate values:

$\phi_t P_n = 803$ kips, $\phi_b M_{nx} = 195$ kip-ft ($L_b = 15$ ft), and $\phi_b M_{ny} = 93.0$ kip-ft

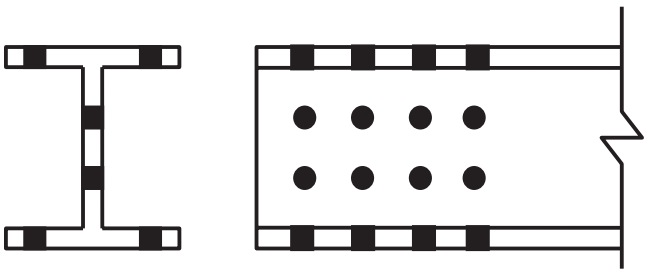

Fig. 6. Example 3 connection.

Consider a W10×60 with $\phi_t P_{ny} = 797$ kips (tensile yielding), $\phi_b M_{nx} = 257$ kips ($L_b = 15$ ft), and $\phi_b M_{ny} = 131$ kip-ft. Also, from AISC *Manual* Table 1-1, $A_g = 17.7$ in.^{2}, $t_w = 0.420$ in., and $t_f = 0.680$ in.

The available tensile rupture strength must be calculated based on the member connection.

$$A_n = 17.7 \text{ in.}^2 - (4 \text{ flange holes})(7/8 \text{ in.} + 1/8 \text{ in.})(0.680 \text{ in.}) - (2 \text{ web holes})(7/8 \text{ in.} + 1/8 \text{ in.})(0.420 \text{ in.})$$
$$= 14.1 \text{ in.}^2$$

$U = 1.0$ (AISC *Specification* Table D3.1, Case 1), therefore, $A_e = A_n = 14.1$ in.^{2}

Available tensile rupture strength:

$$\phi_t P_{nr} = 0.75 F_u A_e$$
$$= (0.75)(65 \text{ ksi})(14.1 \text{ in.}^2)$$
$$= 687 \text{ kips}$$

Available tensile yielding strength:

From AISC *Manual* Table 6-1, $\phi_t P_{nv} = 797$ kips

$$\phi_t P_{nv} = 797 \text{ kips} > \phi_t P_{nr} = 687 \text{ kips}$$

Therefore, use $\phi_t P_n = 687$ kips

Check the W10×60 for compliance with AISC *Specification* Equation H1-1a or H1-1b.

$$\frac{P_u}{\phi_t P_n} = \frac{300 \text{ kips}}{687 \text{ kips}}$$
$$= 0.437 > 0.20$$

Therefore, use AISC *Specification* Equation H1-1a.

$$\frac{P_u}{\phi_t P_n} + \frac{8}{9}\left(\frac{M_{ux}}{\phi_b M_{nx}} + \frac{M_{uy}}{\phi_b M_{ny}}\right) \le 1.0$$

$$0.437 + \frac{8}{9}\left(\frac{85.0 \text{ kip-ft}}{257 \text{ kip-ft}} + \frac{25.0 \text{ kip-ft}}{131 \text{ kip-ft}}\right) = 0.90 < 1.0 \quad \textbf{o.k.}$$

The W10×60 (ASTM A992/A992M) is an appropriate trial section. For the lightest section try a W10×54. The remainder of the solution is similar to trying the W10×60. Note that to complete the design, provisions of AISC *Specification* Sections H4 and F13.1 must be checked as well.

EXAMPLE 4

Given:

Determine the lightest ASTM A992/A992M W12 section in biaxial bending with the following conditions:

$L_b = 14$ ft

$M_{ux} = 600$ kip-ft, $M_{uy} = 110$ kip-ft

Solution:

Look up the average value for M_{cy} ($\phi_b M_{ny}$) from Table 3 as follows. Given the relatively large M_{uy}, assume that this section may be heavier than 200 lb/ft at this point.

$$(M_{cy})_{avg} = (\phi_b M_{ny})_{avg} = 320 \text{ kip-ft}$$

Use Equation 12 to calculate an estimate for $(\phi_b M_{nx})_{est}$.

$$\frac{M_{rx}}{M_{cx}} + \frac{M_{ry}}{M_{cy}} = 1.0 \tag{12}$$

$$\frac{600 \text{ kip-ft}}{(\phi_b M_{nx})_{est}} + \frac{110 \text{ kip-ft}}{320 \text{ kip-ft}} = 1.0$$

Therefore, $(\phi_b M_{nx})_{est} = 914$ kip-ft.

From AISC *Manual* Table 6-1, choose a trial W12 section with the following approximate values:

$\phi_b M_{nx} = 914$ kip-ft ($L_b = 14$ ft), and $\phi_b M_{ny} = 320$ kip-ft

Try a W12×152 with $\phi_b M_{nx} = 895$ kip-ft ($L_b = 14$ ft), and $\phi_b M_{ny} = 416$ kip-ft. Note that this section is not heavier than 200 lb/ft as assumed earlier, but that is fine because exact strength values will be used for these calculations.

Use Equation 12 to check compliance with AISC *Specification* provisions. Note that Equation 12 is a modified version of AISC *Specification* Equation H1-1b with $P_r = 0$ and, thus, $\frac{P_r}{P_c} = 0 < 0.20$.

$$\frac{M_{ux}}{\phi_b M_{nx}} + \frac{M_{uy}}{\phi_b M_{ny}} = \frac{600 \text{ kip-ft}}{895 \text{ kip-ft}} + \frac{110 \text{ kip-ft}}{416 \text{ kip-ft}}$$
$$= 0.935 < 1.0 \quad \textbf{o.k.}$$

For a lighter section, try a W12×136 with $\phi_b M_{nx} = 785$ kip-ft ($L_b = 14$ ft), and $\phi_b M_{ny} = 368$ kip-ft from AISC *Manual* Table 6-1.

Use Equation 12 to check compliance with AISC *Specification* provisions.

$$\frac{M_{ux}}{\phi_b M_{nx}} + \frac{M_{uy}}{\phi_b M_{ny}} = \frac{600 \text{ kip-ft}}{785 \text{ kip-ft}} + \frac{110 \text{ kip-ft}}{368 \text{ kip-ft}}$$
$$= 1.06 > 1.0 \quad \textbf{n.g.}$$

Choose a W12×152 (ASTM A992/A992M) as the trial section.

COMPARISON OF DIFFERENT METHODS

Table 5 lists the characteristics of the different methods discussed for comparison purposes.

REFERENCES

AISC (2001), *Load and Resistance Factor Design (LRFD) Steel Construction Manual*, 3rd Ed., American Institute of Steel Construction, Chicago, Ill.

AISC (2011), *Steel Construction Manual*, 14th Ed., American Institute of Steel Construction, Chicago, Ill.

AISC (2017), *Steel Construction Manual*, 15th Ed., American Institute of Steel Construction, Chicago, Ill.

AISC (2022), *Specification for Structural Steel Buildings*, ANSI/AISC 360-22, American Institute of Steel Construction, Chicago, Ill.

AISC (2023), *Steel Construction Manual*, 16th Ed., American Institute of Steel Construction, Chicago, Ill.

Aminmansour, A. (2000), "A New Approach for Design of Steel Beam-Columns," *Engineering Journal*, AISC, Vol. 37, No. 2, pp. 41–72.

Aminmansour, A. (2004), "Steel Beam-Column Design: New Fast and Practical Approach," *Practice Periodical on Structural Design and Construction*, ASCE, May, pp. 93–97.

Aminmansour, A. (2006), "New Method of Design for Combined Tension and Bending," *Engineering Journal*, AISC, Vol. 43, No. 4, pp. 247–256.

Aminmansour, A. (2009), "Technical Note: Optimum Flexural Design of Steel Members Utilizing Moment Gradient and C_b," *Engineering Journal*, AISC, Vol. 46, No. 1, pp. 47–56.

Table 5. Comparison of Different Methods for Design of Members Subject to Combined Forces								
	Constraints[2]			Flexibilities[3]				
				Axial Load		Bending		
Method[1]	Method Limitations	Column Sections Only[4]	$L_b = L_c$[5]	Comp.	Tension	M_x	M_y	$M_x + M_y$
Burgett (1973)	Uses P_{eff}[6]	x	x	x		x	x	x
Uang et al. (1990)	Uses P_{eff}[6]	x	x	x		x	x	x
Aminmansour (2000)				x		x	x	x
Keil (2000)		x	x[7]	x		x		
Aminmansour (2006)					x	x	x	x
Hosur and Augustine (2007)		x	x[7]	x		x		
Sa'adat and Banam (2014)				x	x	x		
Reynolds and Uang (2019)	Uses P_{eq}[6]		x	x		x	x	x
Proposed Method				x	x	x	x	x

[1] See References list.
[2] Fewer entries per method is better.
[3] More entries per method is better.
[4] Selection limited to sections ordinarily used as columns.
[5] Method assumes $L_b = L_c$, otherwise outcome may be unconservative in some instances.
[6] Method requires conversion of bending moments to an equivalent axial load.
[7] Modifications available for other lengths.

Aminmansour, A. (2017), "Steelwise—One-Stop Shop," *Modern Steel Construction*, AISC, July.

ASTM (2022), *Standard Specification for Structural Steel Shapes*, ASTM A992/A992M, ASTM International, West Conshohocken, Pa.

Burgett, L.B. (1973), "Selection of a Trial Column Section," *Engineering Journal*, Vol. 10, No. 2, pp. 56–59.

Hosur, V. and Augustine, B. (2007), "Graphical Design Aid for Beam-Columns (LRFD)," *Engineering Journal*, Vol. 44, No. 2, pp. 147–180.

Keil, W.J. (2000), "LRFD Beam-Column Graphical Design Aid," *Engineering Journal*, Vol. 37, No. 3, pp. 99–119.

Reynolds, M. and Uang, C.M. (2019), "Updated Equivalent Axial Load Method for Design of Steel Beam-Columns," *Engineering Journal*, Vol. 56, No. 3, pp. 149–158.

Rubinsky, M.A. (1968), "Rapid Selection of Beam-Column," *Engineering Journal*, Vol. 5, No. 3, pp. 100–122.

Sa'adat, M.A. and Banan, M.R. (2014), "A Graphical Design Aid for Selecting Standard W-Shape Steel Beam-Columns with Minimum Weight," *Engineering Journal*, Vol. 51, No. 4, pp. 237–246.

Swanson, J.A. (2016), "Strength of Beams in Beam-to-Column Connections with Holes in the Tension Flange," *Engineering Journal*, Vol. 53, No. 3, pp. 159–172.

Uang, C.M., Wattar, S.W., and Leet, K.M. (1990), "Proposed Revision of the Equivalent Axial Load Method for LRFD Steel and Composite Beam-Column Design," *Engineering Journal*, Vol. 27, No. 4, pp. 150–157.

Column Base Connections: Research, Design, and a Look to the Future

AMIT M. KANVINDE

This paper is based on the 2022 T.R. Higgins lecture.

ABSTRACT

Column base connections are critical to the performance of steel structures, serving as the interface between the steel superstructure and concrete foundation. Historically under-researched, these connections have received significant attention over the past two decades, leading to major advances in understanding their strength, stiffness, seismic behavior, and simulation. This paper provides a synthesis of these developments, focusing on exposed and embedded base connections across a range of loading conditions and structural configurations. Key contributions include improved strength models, detailed assessments of seismic performance, and the introduction of modeling tools now included in the 3rd Edition of AISC Design Guide 1. The paper discusses elastic and inelastic behavior, base connection–frame interaction, and the emerging use of base connections as yielding elements in seismic design. Advances in simulation of base connections, including rotational spring and line-element-based models, enable more accurate structural simulations. Despite this progress, notable gaps remain, including the behavior of braced frame connections, foundation-soil interaction, and performance-based design for repairability and resilience. This work aims to consolidate recent findings, inform ongoing research, and guide future design practices toward a more integrated treatment of base connections in steel structures.

Keywords: base connection, moment frames, composite connection.

INTRODUCTION

Column base connections are arguably the most critical connections in steel buildings because they transfer forces from the entire structure into the foundation. They are essential in every steel building, regardless of the structural system or type of loading. While their forms can vary significantly, depending on their function (e.g., moment frames versus braced frames) or the magnitude of the load (leading to exposed versus embedded connections), they are always located at the interface between steel and concrete. This interface makes both their behavior and design particularly interesting and complex because these connections are inherently composite in nature (i.e., internal forces are carried by both steel and concrete and the interfaces between them). In fact, base connections exist not only at a physical boundary, but also at a disciplinary one, between the steel and concrete trades, where research and standards development often occur independently. Furthermore, base connections interact with the structure affecting its response. These behaviors influence not only the design of the connections, but also the performance and design of the entire structural system.

Amit Kanvinde, Professor, Department of Civil and Environmental Engineering, University of California–Davis, Davis, Calif. Email: kanvinde@ucdavis.edu

Paper No. 2025-09

Figure 1 illustrates base connection details commonly used in U.S. construction practice. Historically, research on base connections has lagged behind that of other structural connections. This is particularly notable given their critical role. However, over the past two decades, there has been a substantial increase in global research attention, leading to significant advances in multiple areas, including: (1) improved understanding of failure modes and the development of strength models for various base connection configurations; (2) evaluation of seismic performance and its implications for both connection and system-level design; (3) development of simulation methodologies tailored specifically to base connections; and (4) integration of research findings into practical design tools, such as manuals and software, notably, the release of the 3rd Edition of AISC Design Guide 1, *Base Connection Design for Steel Structures* (Kanvinde et al., 2024), published nearly two decades after the 2nd Edition (Fisher and Kloiber, 2006). The primary objective of this paper is to provide an overview of these developments, culminating in the current state-of-the-art understanding of base connections. Topics include behavioral characteristics, modeling strategies, design considerations, and emerging research needs and priorities. This paper accompanies the 2022 T.R. Higgins Lectureship Award presentation (of the same title) and expands upon the themes introduced in that lecture.

The paper begins by summarizing key research developments that have emerged since the publication of a landmark report (Grauvilardell et al., 2005) that offers a

comprehensive overview of earlier work on base connections. This is followed by a discussion of the current state-of-the-art in three critical areas: (1) strength models and design approaches for various base connection configurations, (2) modeling of base connection behavior, and (3) seismic response and related design considerations. The narrative also describes how relevant advances in each area have been integrated into the 3rd Edition of Design Guide 1. The paper concludes by highlighting ongoing research, identifying remaining gaps in knowledge and design guidance.

RESEARCH DEVELOPMENTS

Figure 2 illustrates the number of articles published over the past several decades on the general topic of column base connections or base plates. Notably, there is a marked increase in publications following the release of the Grauvilardell et al. (2005) report, suggesting its significant role in catalyzing research in this area. A closer look at these studies reveals that the surge in interest was global, with substantial contributions from researchers in the United States, Europe, Asia, and South America. This body of work can be broadly categorized into three areas: (1) studies on exposed column base plate connections, (2) studies on embedded column base connections, and (3) investigations into the interaction between base connections and the structural frame. The findings from these studies have been integrated to develop strength models, modeling guidance, and design philosophies—particularly in the seismic context—that leverage the available deformation capacity of base connections. This section provides a brief overview of the research conducted since 2006, while the remainder of the paper synthesizes the key findings and implications of this work.

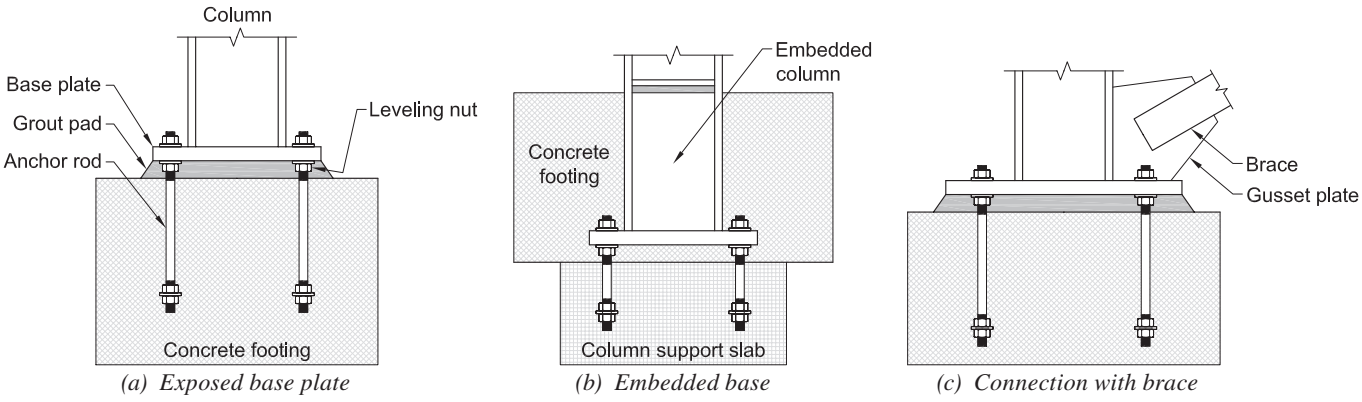

(a) Exposed base plate *(b) Embedded base* *(c) Connection with brace*

Fig. 1. Column base connections commonly used in the United States.

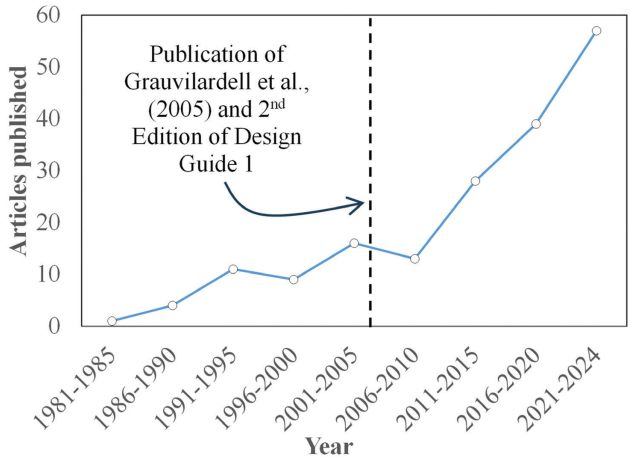

Fig. 2. Articles published on the topic of column base connections during each 5-year period between 1981–2024 (Source: EI-Compendex database with "Column base connections"and related keywords).

A significant portion of research on base connections has focused on exposed base plate connections, such as the configuration shown in Figure 1(a). Much of this work has addressed base connections without braces or gusset plates and has included large-scale experiments by Gomez et al. (2010), Kanvinde et al. (2014), Trautner et al. (2017), and Hassan et al. (2022). These U.S.-based studies are complemented by similar work in Europe (e.g., Wald et al., 2008; Gresnigt et al., 2008; Di Sarno et al., 2007), which has expanded the experimental database for model development and validation. Additional studies from Japan (Choi and Ohi, 2005), South Korea (Choi and Choi, 2013), and France (Seco et al., 2021), as well as from Fasaee et al. (2018), have examined base plates under biaxial bending and axial compression. These experimental efforts have been supported by finite element analyses, which help generalize findings to untested configurations and offer insight into internal force distributions and design strategies.

In contrast, research on embedded base connections was limited prior to 2006. Since then, significant progress has been made on both deeply embedded (Grilli et al., 2017; Hassan and Kanvinde, 2023) and shallowly embedded or "blockout" (Barnwell, 2015; Hassan et al., 2024; Hanks and Richards, 2019) configurations, along with related work in Japan (Cui et al., 2009). As with exposed connections, this body of research has informed strength, stiffness, and load-deformation models. Finally, notable advances have been made in understanding the seismic performance of base connections in moment frame systems. Collectively, these developments have been synthesized into the 3rd Edition of Design Guide 1.

Another important area of research involves the simulation of base connections, particularly their rotational response (both in terms of initial stiffness and hysteresis) and its effect on member and frame response. For example, Kanvinde et al. (2012), Richards et al. (2018), and Torres-Rodas et al. (2017) present stiffness models, while Torres-Rodas et al. (2016), Torres-Rodas et al. (2018), and Villar-Salinas et al. (2024) provide nonlinear load-deformation models. These models have been validated at multiple scales, including through studies of instrumented buildings (Falborski and Kanvinde, 2022), and have informed the development of design considerations for base connections under seismic loading. Research in this area continues to evolve, addressing several unresolved questions that are discussed in the concluding section of this paper.

STRENGTH MODELS AND DESIGN

Almost all research on column base connections has been for connections without braces; this is the focus of discussion in this section. Within this, exposed type base plate connections are first addressed, followed by embedded type base connections. Some discussion of base plates with braces is also provided at the end of this section.

Exposed Base Plate Connections without Braces

The design of exposed base plate connections, wherein a steel column is welded to a base plate anchored to a concrete footing using cast-in or post-installed anchors, has been the focus of the first two editions of Design Guide 1, as well as a majority of prior research. The design process generally involves two key steps: (1) estimating the internal stress or force distribution within the connection and (2) evaluating potential limit states in various components resulting from this distribution. The internal stress distribution arises from complex mechanics, involving phenomena such as contact and separation between components, nonlinear behavior of the footing materials, and deformation of both the base plate and anchors. Except in very simple cases where anchor forces may be assumed equal—such as a rigid base plate in pure tension—estimation of internal force distribution is nontrivial.

For typical base connections subjected to axial load (usually compression) and flexure, the method developed by Drake and Elkin (1999) is widely used. This approach simplifies the connection mechanics by representing the bearing stress in the concrete as a triangular or rectangular stress block [see Figure 3(a)]. This results in a system of two equilibrium equations that can be solved to determine the anchor forces [denoted T in Figure 3(a)] and the width of the bearing stress block [denoted Y in Figure 3(a)]. Once the internal forces are known, they are used to evaluate the following limit states: (1) flexural yielding of the base plate at both the bearing and tension faces, (2) anchor yielding or concrete failure, and (3) concrete crushing in the footing. The concrete limit states at the base plate bearing interface, and the anchorage into the concrete on the tension side are evaluated following the requirements of ACI 318 (ACI, 2019) code requirements for structural concrete and commentary. Figure 3(b) illustrates assumptions underlying the method, which was developed based on engineering judgment prior to much of the testing on base connections. Specifically, Figure 3(b) compares the estimated moment strengths from 35 large-scale tests conducted at UC Davis and UC San Diego with predictions from the Drake and Elkin (1999) method (using the rectangular stress block model) as presented in Design Guide 1. The figure also indicates the predicted failure mode for each test.

A closer examination of the results and underlying test data [not shown here, but see the references in the legend in Figure 3(b)] indicates that the method is accurate or conservative. It is particularly noteworthy that this level of agreement is achieved by a method developed without the benefit of experimental calibration, reaffirming the value of fundamental engineering principles and judgment. In

cases where anchor rod yielding governs, the method demonstrates near-perfect accuracy. Conversely, the method is more conservative when plate bending governs. In fact, when flexural yielding of the base plate controls the response, the method tends to significantly underpredict strength due to several factors: (1) When the plate yields in flexure on the bearing side, a complete failure mechanism does not form until another limit state is reached, typically flexural yielding of the base plate on the tension side or anchor rod yielding, or until bearing failure occurs in the footing. (2) The assumed bearing stress distribution under the plate often does not reflect actual stresses, which tend to concentrate under the column flange, leading to inaccurate estimates of the bending moment in the plate. (3) When flexural yielding occurs on the tension side, the base plate tends to exhibit significant strain hardening. However, this latter failure mode should be avoided because it can cause kinking of the plate beneath the column weld, increasing the risk of fracture.

In addition, the approach in Design Guide 1 presents several broader limitations, some of which have been addressed in subsequent research and must be considered in its application. First, the approach—particularly its rectangular stress block (RSB) variant—assumes that the bearing capacity of the footing (denoted q_{max}; see Figure 3) is fully mobilized even at relatively low applied moments, as long as the moment-to-axial load ratio indicates "high eccentricity." While this assumption is useful and often necessary for simplified analysis, it can yield unrealistic results when the applied moment is insufficient to mobilize the footing bearing capacity. Such situations are not uncommon and can significantly affect downstream calculations, especially in estimating anchor rod forces and the associated uncertainties. These estimates are particularly sensitive to the assumed bearing stress distribution and its variability; see Song et al. (2020) for further discussion. Second, the approach is limited to a specific configuration: a base plate subjected to uniaxial bending with a single row of anchor rods in tension. It does not extend to cases involving biaxial bending [addressed by Fasaee et al. (2018) and Hassan et al. (2021) and included in the 3rd Edition of Design Guide 1], multiple rows of anchors, circular columns, or nonrectangular base plates. Furthermore, it does not account for effects such as prying action, which may occur when base plates extend significantly beyond the anchor rods.

Recognizing that a single analytical method cannot accommodate all possible configurations, there is growing interest in the use of conventional finite element models and, more recently, the component-based finite element method (CBFEM), for such analyses (Sabatka et al., 2014). These methods offer the potential to overcome many limitations of analytical approaches, especially when they can accurately simulate underlying physical behavior, such as contact interactions and material responses. However, the reliability of their results depends heavily on a range of modeling assumptions, including component geometry idealization, element selection, contact definitions, and material constitutive models. As such, careful application and benchmarking against experimental data are essential. Appendix D of Design Guide 1 outlines several considerations for the effective use of finite element modeling in base connection analysis.

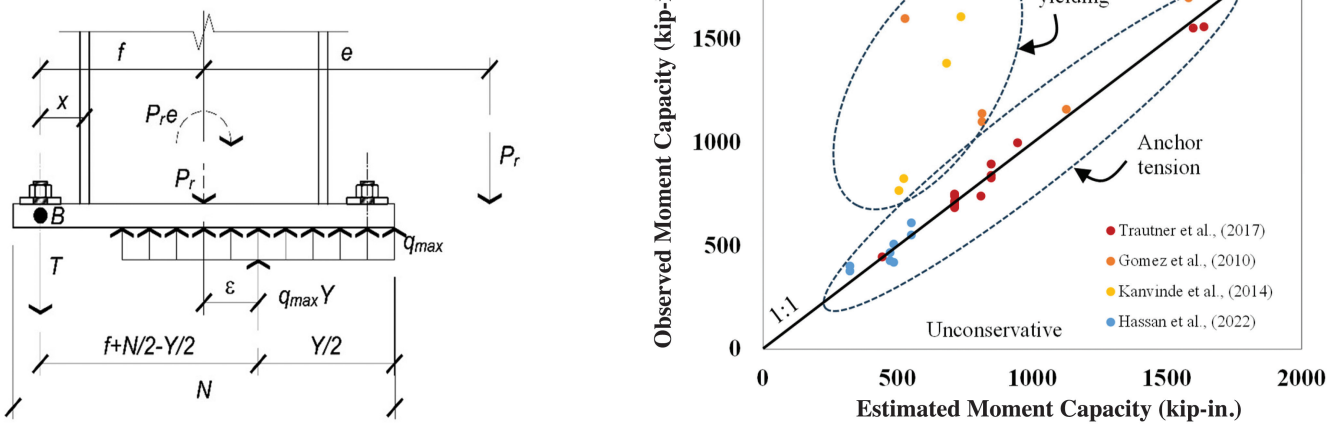

(a) High-eccentricity case

(b) Results applied to test data

Fig. 3. Drake and Elkin method.

Embedded Base Connections

Figure 1(b), shown previously, illustrates embedded base connections. These may be specified in two situations:

1. When the design forces and moments are large enough that transferring them through exposed base plate connections becomes unfeasible or prohibitively expensive. This is typically due to the need for a large number of heavy anchors and a thick base plate. In such cases, embedding the base offers a more practical alternative. However, this approach involves a tradeoff: It requires two separate concreting operations—first to erect the column base and then again to complete the embedment, adding both time and cost. These are referred to as "deeply embedded column bases—DECB" in this paper and are shown in Figure 4.
2. When a slab-on-grade is poured over conventional exposed base plate connections to achieve a smooth finished surface. In this case, the embedment (whose thickness is equal to the slab depth) is incidental rather than intentional and is not specifically designed to provide strength. These are denoted "shallowly embedded column bases—SECB" or "blockout" connections, owing to the diamond-shaped blockout that is placed around the columns during installation of the floor slab to facilitate subsequent column erection and a second concrete pour within this blocked out region, as shown in Figure 5.

In both scenarios, however, the embedment provides additional strength and stiffness. In the first case, this contribution is critical and must be explicitly considered in the design. In the second case, although the added strength is unintentional, it can significantly affect seismic performance assessments. When multiple such incidental embedments are present in a structure (e.g., at the bases of gravity frames), their cumulative effect on overall resistance can be considerable.

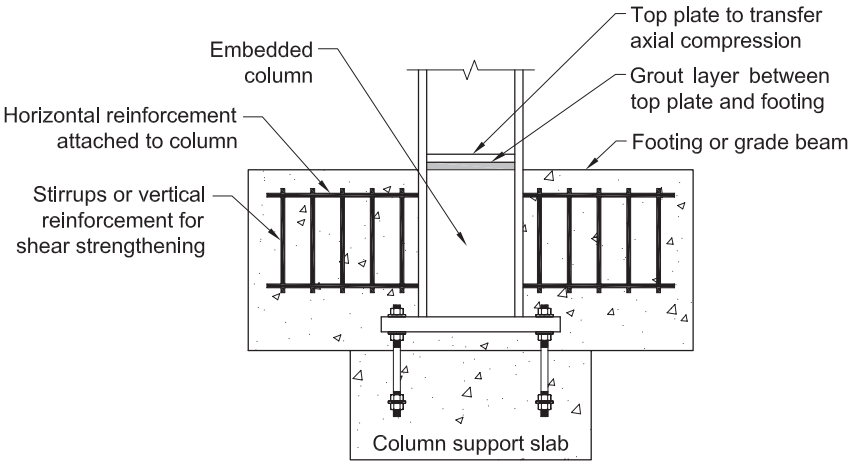

Fig.4. Deeply embedded column base connection.

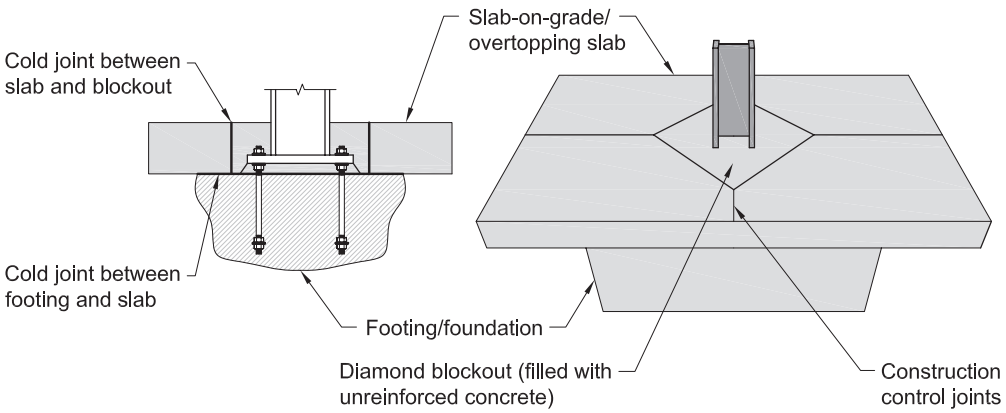

Fig. 5. Blockout connections resulting in shallow embedment of base plate connection.

Research on embedded base connections has been relatively limited, with most studies emerging only in recent years. As a result, formal design guidance has also been lacking. In the absence of definitive research, design guidelines for embedded connections, specifically the AISC *Seismic Design Manual* (AISC, 2018), have largely relied on engineering judgment informed by observed structural behavior and design methodologies developed for steel brackets or coupling beams embedded in concrete shear walls (Mattock and Gaafar, 1982; Shahrooz et al., 1993). However, research including experimental and analytical studies conducted in the United States (e.g., Hassan and Kanvinde, 2023; Grilli et al., 2017; Richards et al., 2018), Japan (Cui et al., 2009), and Europe (Pertold et al., 2000a, 2000b; Inamasu et al., 2020) has significantly advanced the understanding of internal force distributions and contributed to the development of more accurate strength models. The models—specifically their mathematical formulations and other relevant details—are discussed in the references just cited. Figure 6 illustrates the internal force distribution (inferred from physical experiments as well as finite element simulations) in DECB connections.

The main observations are as follows:

1. Compressive axial forces are resisted through a properly designed load path, either via stiffener-type plates provided at the top of the connection [see Figure 6(a)] or a conventional base plate, assuming the foundation below is adequately designed to transfer these forces. Tensile forces are most effectively resisted by the lower base plate bearing upward against the footing.
2. Applied moments are resisted by a combination of horizontal and vertical reactive forces acting on the embedded portion of the column. This is in contrast to assumptions inherent in commonly used approaches that idealize embedded connections as steel coupling beams, in which only the resistance due to the horizontal bearing stresses on the column flanges is active. The moment [M_{HB} in Figure 6(b)] is resisted by horizontal forces—that is, bearing stresses on the column flanges, as well as forces transmitted through any attached reinforcement [see Figure 6(b)]. The moment resisted by vertical stresses (denoted M_{VB}) consists of bearing stresses on the embedded base plate [Figure 6(c)] and the forces carried by anchor rods, if such rods are provided to secure the lower base plate.
3. The proportion of the moment resisted by each mechanism depends on the embedment depth; greater embedment typically results in a larger share of the moment being resisted by horizontal forces. Grilli and Kanvinde (2017) and Hassan and Kanvinde (2023) outline methods for quantitatively estimating these in DECB connections; these stresses are governed by the flexural stiffness of the embedded column relative to the reactive stiffness of the surrounding footing material, particularly the stiffness associated with horizontal bearing stresses. Hassan et al. (2024) provide similar analysis for SECB/blockout connections.
4. Based on the internal force distributions, various limit states may be evaluated to estimate the connection strength. These include (a) mobilization of bearing capacities (for horizontal stresses, this depends on the concrete strength and confinement effects; for vertical stresses, it is often governed by the breakout strength of the concrete above the base plate as it experiences uplift) and (b) resistance of reinforcement or anchors (the contribution of any embedded reinforcement attached to the column flanges or anchors attached to the base plate must also be considered).

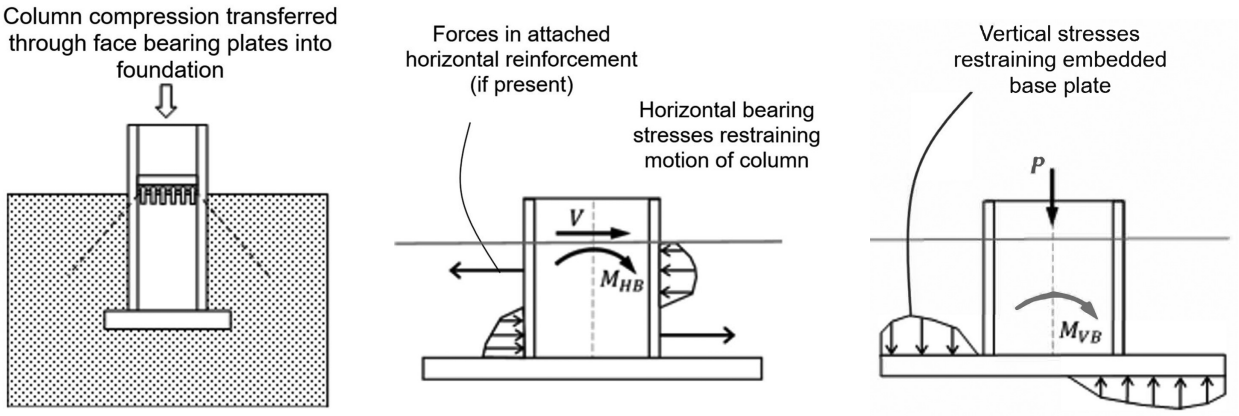

(a) Axial compression *(b) Horizontal bearing* *(c) Vertical bearing*

Fig. 6. Internal force transfer in embedded base connections.

5. Recent experiments (Hassan et al., 2024), reveal some nonintuitive aspects of the connection response that are important to consider in design. Specifically, in configurations where horizontal reinforcement is attached to the column flanges to enhance moment resistance, the reinforcement does increase horizontal strength. However, it also induces a tension field in the footing above the base plate. This creates a tradeoff: while horizontal reinforcement improves moment capacity, it concurrently decreases uplift strength of the underlying base plate due to the development of this tension field. The net effect of this tradeoff depends on the overall connection configuration and the presence of stirrups or shear reinforcement that can mitigate uplift reduction. Given the difficulty in reliably estimating the uplift resistance in such cases, it may be conservative to disregard the contribution from vertical forces altogether when horizontal reinforcement is provided.

These approaches are described in the 3rd Edition of Design Guide 1 along with a demonstrative solved example. Additionally, software tools are provided in the Design Guide 1 bonus materials on the AISC website to assess the strength of DECB connections and facilitate design.

Base Connections with Attached Braces

Research on base connections with attached braces, such as the one shown in Figure 7 (commonly found in braced frames), is virtually nonexistent. Consequently, strength models and design approaches for these connections are typically based on generalizations of behavior and internal force distributions inferred from connections without braces, as discussed in the preceding sections.

While such extrapolations are expedient, it is important to recognize that several key differences between braced and unbraced connections may influence internal force distributions and limit states. First, the presence of a gusset plate required to attach the brace often results in an asymmetric base plate layout and a corresponding asymmetry in stiffness distribution—with a potential for unanticipated internal force distributions. Second, base connections with braces frequently use six- or eight-anchor configurations, placing them outside the scope of the methods outlined in Design Guide 1. Finally, while connections in braced frames are often designed as pinned (and modeled as such in structural analysis), they have significant rotational restraint provided by the anchors, the gusset, and the plate. This unintended stiffness could attract moments to the connection and induce additional forces in the anchors that are not accounted for in current design practices.

SIMULATING BASE CONNECTIONS

Simulation of base connections can be considered in two principal contexts: (1) simulation of the connections themselves to characterize internal force distributions (e.g., for the design of anchors or other subcomponents) when configurations fall outside the scope of Design Guide 1 or other guidance and (2) representation of base connections within frame simulations of the overall structure. This paper focuses on the latter, recognizing that the load–deformation behavior of base connections significantly influences global structural response, with critical implications for seismic design, as discussed in the following section. The former is addressed in detail in Design Guide 1, Appendix D. The moment–rotation response is of primary interest in

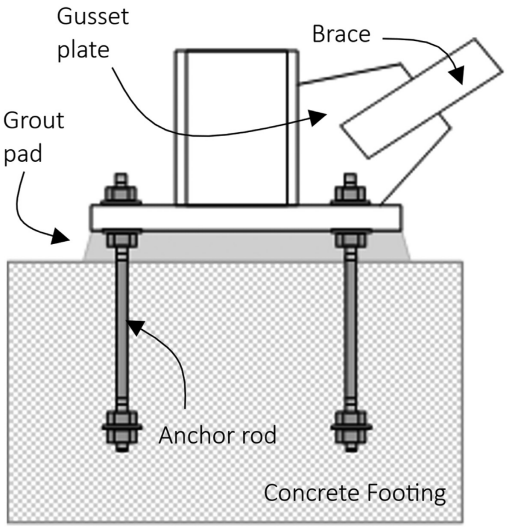

Fig. 7. Column base connection in a braced frame.

structural simulations; however, responses along additional degrees of freedom (e.g., uplift or axial force and deformation) and their interaction with moment–rotation behavior are also relevant. The primary emphasis here is on the elastic response of base connections because they are typically designed to remain elastic under service conditions. Nevertheless, growing interest in leveraging their inherent ductility for seismic applications has increased the need to simulate their inelastic behavior as well. Two classes of models have been used effectively to simulate column base response: (1) rotational hinge models calibrated to reproduce moment–rotation behavior and (2) line element–based models—often termed "hook and gap" models—that simulate individual connection components (e.g., anchors or base plates) using beam–column elements. Each approach (illustrated schematically in Figure 8) is discussed in the following, with emphasis on validated methodologies and best practices.

Rotational Spring Models

Rotational spring models idealize the behavior of column bases as purely rotational, following well-established methodologies similar to those used for modeling plastic hinges in beam-columns (Lignos and Krawinkler, 2011). While the complete load-deformation response, including nonlinear monotonic and hysteretic behavior, is relevant in scenarios where base yielding is anticipated, this study focuses on the elastic rotational stiffness of base connections because this property is frequently of primary interest in design and analysis. A recurring question in structural simulation, whether for elastic design or nonlinear performance assessment, is whether base connections should be idealized as pinned or fixed. It is critical to recognize that base connection stiffness, in absolute terms, cannot be inherently classified as either pinned or fixed. Instead, its role must be evaluated in relation to the global structural response and the specific performance metrics of interest, such as interstory drift or internal forces and moments in the members. Accordingly, it is generally more accurate to model the base connection explicitly as an elastic rotational spring, incorporating an appropriate estimate of stiffness.

Until recently, reliable methods for estimating this stiffness were limited. However, recent advances, drawing from physical testing (including those cited in previous sections) and vibration measurements of instrumented buildings (Falborski et al., 2020a), have led to the development and validation of practical stiffness estimation approaches. The underlying model formulations are presented in Kanvinde et al. (2012), Torres-Rodas et al. (2017), and Richards et al. (2018). These models are mechanistic in nature, based on a rational understanding of internal force distributions under applied loads, combined with the aggregation of estimates of deformations across the various connection components under applied loads. User-friendly tools are now available in the form of downloadable executables on the AISC Design Guide 1 webpage, enabling convenient estimation of base rotational stiffness for a variety of connection types, including exposed base plates, embedded connections, and blockout configurations.

As expected, the rotational stiffness of a base connection is primarily governed by connection configuration along

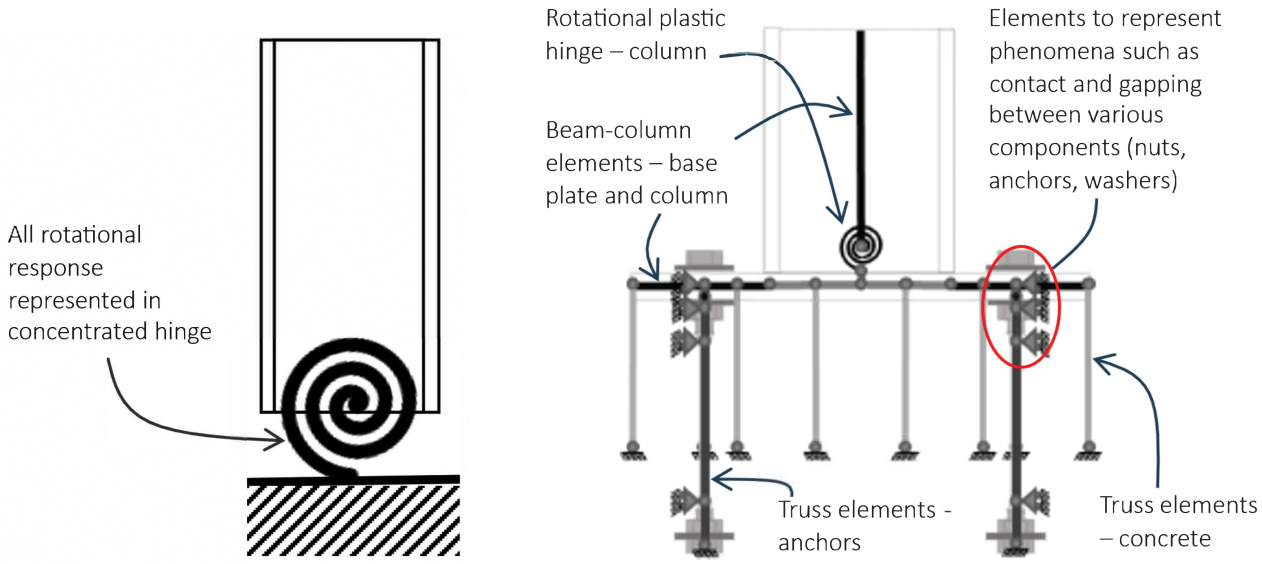

(a) Rotational hinge based *(b) Line-element based*

Fig. 8. Representation of column base connections in frame simulations.

with the dimensions and material properties of key subcomponents such as anchors, base plate, and the footing. In addition, one of the most influential factors is the level of axial compression in the connection. Specifically, high axial compression inhibits uplift of the base plate under rotational loading, thereby significantly increasing the rotational stiffness. However, a purely rotational spring model cannot directly capture the influence of axial force because it is limited to a single rotational degree of freedom. In such cases, a practical approach is to calibrate the effective rotational stiffness of the base connection as a function of the applied axial compression.

The aforementioned computational tools incorporate this dependency. Similar strategies have been employed in the past for modeling plastic hinges in beam-columns. While convenient, these calibrated models assume a constant axial force and therefore cannot account for the effects of varying axial loads—an important limitation, particularly under seismic loading conditions. In reality, the instantaneous behavior of the connection is influenced by the simultaneous variation of axial force and lateral displacement. Furthermore, rotational spring formulations do not account for vertical deformation or stiffness at the base, which can become significant under large axial tension due to overturning demands. These limitations are addressed by the line-element-based (LEB) models, which were illustrated previously in Figure 8(b) and are introduced in the following section.

Line Element Based Models

Line-element-based (LEB) models provide a detailed framework for simulating both the linear and nonlinear behavior of base connections. These models typically idealize the connection region using a series of uniaxial spring elements and elastic beam-column elements [see Figure 8(b)], allowing for the isolated representation of key mechanisms such as bearing, gapping, and plasticity. Unlike simplified rotational spring models discussed in the previous subsection, LEB models are capable of capturing the interaction between axial and lateral (flexural) loads, making them particularly well suited for analyzing complex base behaviors under seismic or cyclic demands. In addition to representing overall load-deformation response, LEB models provide an understanding of response internal to the connection (which is entirely absent from the rotational spring models), allowing for the examination of local quantities such as anchor forces and deformations. While these models are significantly more computationally efficient as compared to continuum finite element models (by a factor of roughly 20), it is important to note that they are slower as compared to rotational spring models. Nonetheless, they have been used with success in suites of nonlinear time history simulations (Song et al., 2023) for probabilistic performance assessment, and their run-time, especially if only elastic response is required, is negligible on modern computers. However, they do require detailed calibration of various properties, including the use of specialized elements such as gap elements. While beyond the scope of this article, Song et al. (2023) and Hassan et al. (2022) provide an overview of best practices in this regard.

SEISMIC DESIGN

Over the past two decades, experimental and analytical studies on base connections have yielded significant insights that enhance the seismic design not only of the connections themselves, but also of the structural frames they are a part of. This section focuses on base connections in moment-resisting frames, consistent with the emphasis of most prior research. According to the AISC *Seismic Provisions for Structural Steel Buildings* (AISC, 2022), seismic design of base connections can follow one of two approaches, illustrated in Figures 9(a) and 9(b): (1) the *strong-base* design, where the base connection is capacity-designed to exceed the strength of the attached column, ensuring that plastic hinging occurs within the column, and (2) the *weak-base* design, which permits inelastic rotations to occur within the base connection.

The strong-base approach typically results in more expensive connections because they must resist the high moments associated with column yielding, often necessitating embedded connections. Despite the higher cost, this method is frequently favored due to the limited design guidance available for detailing base connections to achieve the ductility required by the weak-base approach. The design of strong-base connections is conceptually straightforward because established strength-based design methodologies, such as those previously discussed, can be employed. In this approach, the flexural demand on the base connection is taken as the fully yielded and strain-hardened moment capacity of the connected column. However, it is important to recognize that even when capacity-designed based on column strength, and even when embedded, strong-base connections may exhibit considerable elastic rotational flexibility. In other words, connection strength should not be conflated with stiffness. Assuming these connections to be rigid can lead to unconservative estimates of first-story column moment demands and lateral drift. Accordingly, it is recommended that realistic estimates of connection fixity be incorporated into structural analysis and design, using the modeling approaches summarized in the preceding section.

If a weak-base design approach is adopted, the following questions must be addressed:

1. What loading conditions should the connections be designed for?

2. What level of ductility or deformation demand must they accommodate?
3. How will the required ductility capacity be achieved through practical detailing?

With respect to strength, as discussed earlier, current provisions (AISC *Seismic Provisions*) permit weak-base designs for moments corresponding to the overstrength seismic load (i.e., Ω_0). Additionally, a pinned-base condition (i.e., zero flexural strength at the base) is also allowed, provided that adequate shear strength is maintained. Research indicates that both approaches result in seismic performance (in terms of collapse resistance) comparable to that of strong-base designs. Further, studies (Falborski et al., 2020b) based on a limited set of archetype frames suggest that any base moment strength between fully pinned ($M = 0$) and strong base (i.e., $M_{base} \geq 1.1R_yF_yZ_{column}$) can deliver acceptable performance, provided the following three criteria are satisfied: (1) shear connectivity and resistance are maintained; (2) the moment capacity of the connection is sustained up to a target rotation—typically in the range of 0.04–0.05 rad; and (3) the first-story columns meet strong-column–weak-beam requirements, accounting for the lowered inflection point associated with a weak base.

Ongoing research aims to generalize these findings to support more flexible design provisions, enabling designers to select any base strength that meets these criteria. The ultimate goal is to move away from designing to a prescribed load demand and instead allowing engineers to optimize base strength based on project-specific tradeoffs, balancing the higher connection cost and reduced member demands of a stronger base against the lower connection cost and increased member demands associated with a weaker base.

Arguably the most critical consideration in the design of weak-base connections is ensuring sufficient deformation capacity through appropriate detailing. Encouragingly, experimental evidence indicates that base connections inherently possess substantial ductility, even when not explicitly designed for that purpose. Figure 10 presents the deformation capacities observed in specimens from seven experimental programs conducted over the past five decades. Despite variations in loading protocols among the studies, the overarching finding is consistent: Specimens across all programs demonstrated excellent deformation capacity (well over the 4–5% rotation demand anticipated in weak-base connections), rivaling or even exceeding the ductility typically required of beam-column connections.

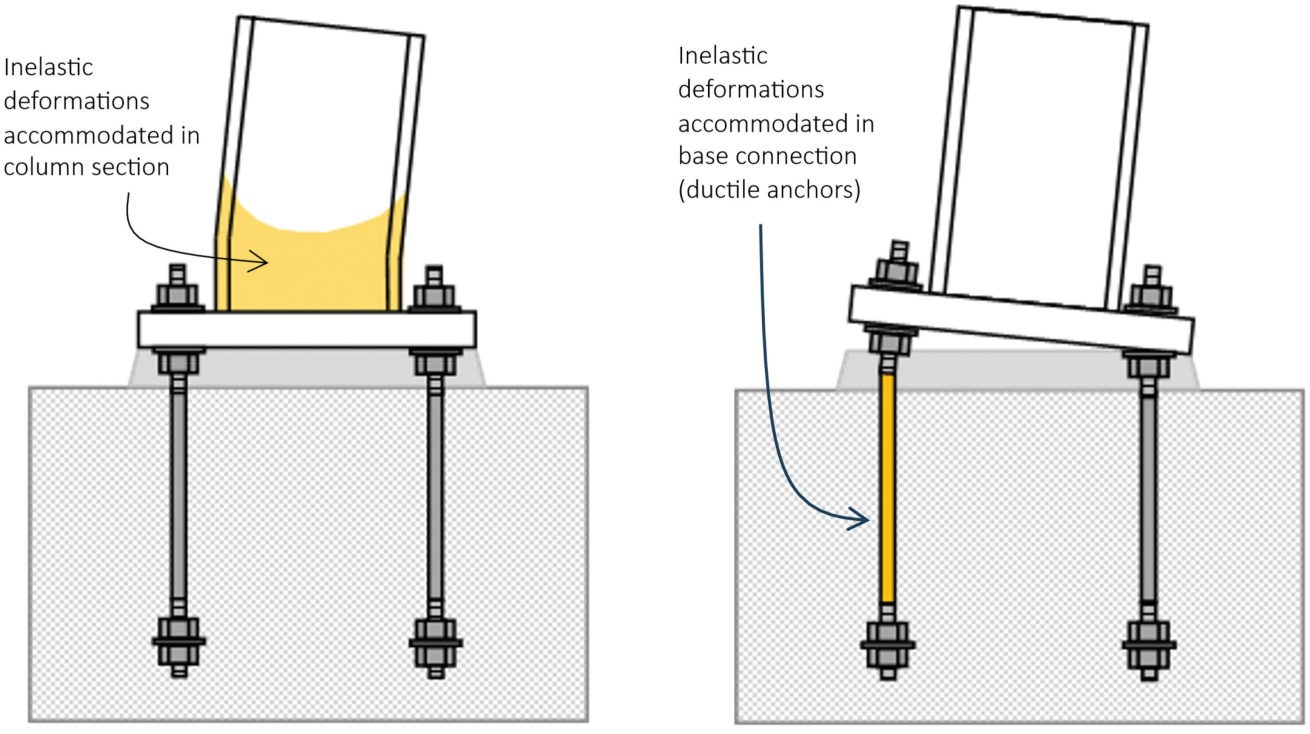

(a) Strong base *(b) Weak base—anchor yielding*

Fig. 9. Seismic column bases.

It is noteworthy that among these programs, only the test series conducted by Hassan et al. (2022) incorporated upset-thread details with a smooth shank, specifically designed to enhance ductility. The 3rd Edition of Design Guide 1 provides detailed recommendations for proportioning and detailing to achieve such high ductility. While this represents one proven approach, the broader experimental data suggest that a variety of alternative detailing strategies may also be engineered to achieve comparable performance. In fact, the other experimental programs shown in Figure 10 did not incorporate details explicitly intended to improve ductility. However, design and detailing considerations in these specimens appear to have incidentally provided sufficient ductility. It is important to recognize these details when interpreting the data shown in Figure 10 for two reasons: (1) to avoid overgeneralizing the results to situations where such details may not be present and (2) to identify and take advantage of beneficial attributes. In this context, the various test programs that demonstrated high ductility incorporated one or more of the following features (see individual program references for details): smooth bars either bonded to or debonded from the concrete, weld details designed to develop the strength of the attached column, and sufficient embedment within the concrete to develop the strength of the anchors. While such details may not always be present in nonseismic bases, they are nevertheless standard and straightforward to incorporate. This is encouraging, suggesting that even without expensive detailing, ductile performance (and weak-base design) is well within reach. Research is needed to definitively establish detailing practices, as well as material and anchor specifications that are able to achieve such ductility.

SUMMARY, CONCLUSIONS, AND REMAINING KNOWLEDGE GAPS

Column base connections are essential to the performance of steel structures, serving as the critical interface between the steel superstructure and the supporting foundation. Despite their ubiquity and structural importance, base connections have historically received limited research attention relative to other structural components. However, the past two decades have seen a significant increase in experimental, analytical, and computational studies, resulting in a more comprehensive understanding of base connection behavior and improved design guidance. This paper has

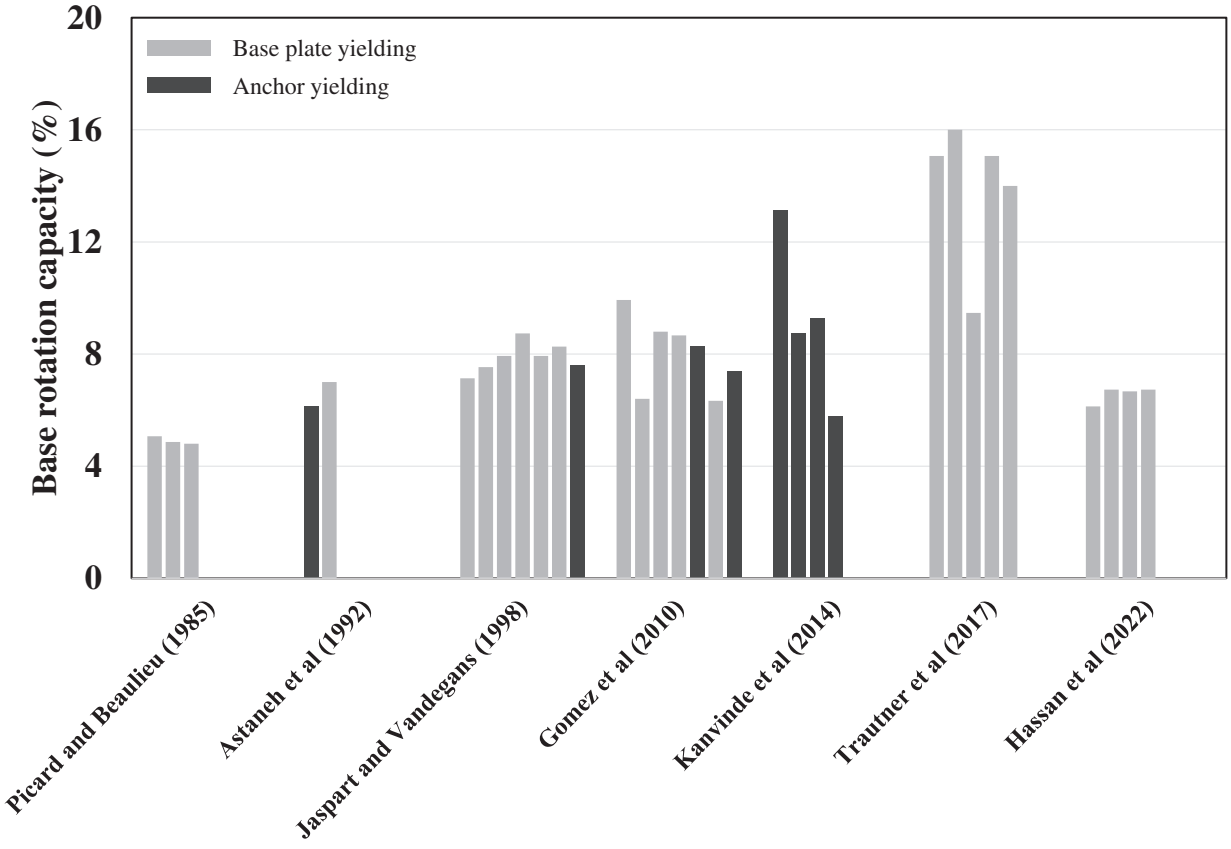

Fig. 10. Base rotation capacity of base connections in various test programs.

reviewed these developments, with emphasis on strength models, seismic performance, modeling approaches, and emerging design philosophies.

Significant advancements have been made in understanding and designing both exposed and embedded base connections, including their internal force distributions and governing limit states. For exposed base plates, widely used strength models such as the Drake and Elkin method continue to perform well, particularly in cases where anchor rod yielding governs. However, limitations in these simplified methods, particularly for complex geometries, have motivated the adoption of more sophisticated tools, such as finite element and component-based models, which can better capture complex response, including multidirectional loading. Embedded base connections, once underexplored, have received increased attention in recent years. New research has yielded reliable strength models and clarified load paths, particularly for deeply embedded configurations. These findings are now reflected in the 3rd Edition of AISC Design Guide 1, which also introduces tools to support practical design. Notably, incidental embedment in shallowly embedded connections has been shown to influence system-level behavior, highlighting the need to consider such effects in performance assessments.

Advances in simulation methods now allow for the accurate representation of base connection stiffness and inelasticity in structural analyses. Rotational spring models provide a simple yet effective approach for elastic design, especially when augmented to account for axial load effects. More detailed line-element-based models can simulate complex behaviors under seismic loading, including axial–moment interaction and uplift effects. The development and dissemination of validated modeling tools—now available through AISC resources—represents a key step toward the broader integration of connection behavior into global frame analyses.

In the context of seismic design, two primary design strategies are prevalent: the *strong-base* approach, which capacity-designs the connection to remain elastic, and the *weak-base* approach, which permits and controls inelastic deformation at the base. Research has shown that both strategies can achieve acceptable seismic performance, provided that specific criteria related to shear resistance, rotational capacity, and column strength are met. Moreover, the ductility demands of weak-base connections are substantial but achievable through rational detailing, evidenced by test programs that demonstrate impressive deformation capacities, even in connections not explicitly designed for ductility.

Despite recent advances, several important knowledge gaps remain. Research on base connections in braced frames is particularly limited, leading to significant uncertainties regarding internal force distributions and deformation capacities. This deficiency hampers the development of robust design methodologies, especially for seismic applications where leveraging the ductility of base connections to implement weak-base strategies remains a priority. In addition, while substantial progress has been made in characterizing the behavior of individual connections, the broader implications of base connection stiffness and strength on system-level seismic performance require further exploration. Another critical area that remains virtually unexplored is the interaction between the base connection, the supporting foundation, and the underlying soil. Key gaps persist in understanding how different foundation types—such as mat foundations, pile caps, individual pedestals, or configurations with grade beams—affect the load path from the column base into the ground. Equally lacking is a unified design methodology that integrates the behavior of the entire base-connection–foundation–soil system. Current practice tends to treat these components in isolation, potentially overlooking important interactions that influence global structural performance. Finally, as design for repairability and functional recovery gains more recognition and adoption in standards, addressing it will be essential for advancing toward more holistic and resilient design approaches.

ACKNOWLEDGMENTS

The author is grateful to the American Institute of Steel Construction for providing sustained funding for this research topic for over a decade and for providing a platform for its dissemination through the T.R. Higgins lecture and to numerous AISC Task and Oversight Committee members for providing feedback during various research projects and standards development efforts. The author also thanks the Charles Pankow Foundation, the National Science Foundation, the Pacific Earthquake Engineering Research Center, and the California Strong Motion Instrumentation Program for providing funding. Finally, the author is grateful to his many doctoral students, postdoctoral scholars, and collaborators who are too many to list and have contributed immensely to various parts of these studies—these are all cited in the references.

REFERENCES

ACI (2019), "Building Code Requirements for Structural Concrete and Commentary," ACI 318-19, Farmington Hills, Mich.

AISC (2018), *Seismic Design Manual*, 3rd Ed., American Institute of Steel Construction, Chicago, Ill.

AISC (2022), *Seismic Provisions for Structural Steel Buildings*, ANSI/AISC 341-22, American Institute of Steel Construction, Chicago, Ill.

Astaneh, A., Bergsma, G., and Shen, J.H. (1992), "Behavior and Design of Base Plates for Gravity, Wind and Seismic Loads," *Proceedings of the National Steel Construction Conference*, AISC, Las Vegas, Nevada.

Barnwell, N. (2015), "Experimental Testing of Shallow Embedded Connections between Steel Columns and Concrete Footings," Master's Thesis, Brigham Young University, Provo, Utah.

Choi, J-H. and Choi, Y. (2013), "An Experimental Study on Inelastic Behavior for Exposed Type Steel Column Bases under Three-Dimensional Loadings," *Journal of Mechanical Science and Technology*, Vol. 27, No. 3, pp. 747–759.

Choi, J-H. and Ohi, K. (2005), "Evaluation on Interaction Surface of Plastic Resistance for Exposed Type Steel Column Based under Biaxial Bending," *Journal of Mechanical Science and Technology* (*KSME International Journal*), Vol. 19, No. 3, pp. 826–835.

Cui, Y., Nagae, T., and Nakashima, M. (2009), "Hysteretic Behavior and Strength Capacity of Shallowly Embedded Steel Column Bases," *Journal of Structural Engineering*, ASCE, Vol. 135, No. 10, pp. 1231–1238.

Di Sarno, L., Pecce, M.R., and Fabbrocina, G. (2007), "Inelastic Response of Composite Steel and Concrete Base Column Connections," *Journal of Constructional Steel Research*, Elsevier, Vol. 63, No. 6, pp. 819–832, http://dx.doi.org/10.1016/j.jcsr.2006.08.007.

Drake, R.M. and Elkin, S.J. (1999), "Beam-Column Base Plate Design—LRFD Method," *Engineering Journal*, AISC, Vol. 36, No. 1, pp. 29–38.

Falborski, T., Hassan, A., and Kanvinde, A.M. (2020a), "Column Base Fixity in Steel Moment Frames: Observations from Instrumented Buildings," *Journal of Constructional Steel Research*, Elsevier, Vol. 168, pp. 105993-1–105993-13, https://doi.org/10.1016/j.jcsr.2020.105993.

Falborski, T. and Kanvinde, A.M. (2022), "Estimation of Nonstructural Stiffness in Instrumented Steel Frames," *Engineering Structures*, Elsevier, Vol. 255, pp. 113947-1–113947-11, 10.1016/j.engstruct.2022.113947.

Falborski, T., Torres-Rodas, P., Zareian, F., and Kanvinde, A.M. (2020b), "The Effect of Base Connection Strength and Ductility on the Seismic Performance of Steel Moment Resisting Frames," *Journal of Structural Engineering*, ASCE, Vol. 146, No. 5, pp. 04020054-1–04020054-15.

Fasaee, M.A.K., Banan, M.R., and Ghazizadeh, S. (2018), "Capacity of Exposed Column Base Connections Subjected to Uniaxial and Biaxial Bending Moments," *Journal of Constructional Steel Research*, Elsevier, Vol. 148, pp. 361–370.

Fisher, J.M. and Kloiber, L.A. (2006), *Base Plate and Anchor Rod Design*, 2nd Ed., Design Guide 1, AISC, Chicago, Ill.

Gomez, I., Deierlein G., and A. Kanvinde (2010), "Exposed Column Base Connections Subjected to Axial Compression and Flexure," Final Report, AISC, Chicago, Ill.

Grauvilardell, J.E., Lee, D., Ajar, J.F., and Dexter R.J. (2005), "Synthesis of Design, Testing and Analysis Research on Steel Column Base Plate Connections in High Seismic Zones," Structural Engineering Report No. ST-04-02, Department of Civil Engineering, University of Minnesota, Minneapolis, Minn.

Gresnigt, N., Romeijn, A., Wald, F., and Steenhuis, M. (2008), "Base Plate in Bending and Anchor Bolts in Tension," *HERON*, Vol. 53, No. 1/2.

Grilli, D.A., Jones, R., and Kanvinde, A.M. (2017), "Seismic Performance of Embedded Column Base Connections Subjected to Axial and Lateral Loads," *Journal of Structural Engineering*, ASCE, Vol. 143, No. 5, pp. 04017010-1–04017010-10.

Grilli, D.A., and Kanvinde, A.M., (2017), "Embedded Column Base Connections Subjected to Seismic Loads: Strength Model," *Journal of Constructional Steel Research*, Vol. 129, pp. 240–249.

Hanks, K.N. and Richards, P.W. (2019), "Experimental Performance of Block-out Connections at the Base of Steel Moment Frames," *Journal of Structural Engineering*, ASCE, Vol. 145, No. 7, p. 04019066.

Hassan, A.S. and Kanvinde, A.M. (2023), "Seismic Performance of Embedded Column Base Connections with Attached Reinforcement: Tests and Strength Models," *Engineering Journal*, AISC, Vol. 60, No. 4, pp. 225–244.

Hassan, A.S., Maity, A., Kanvinde, A.M., and Richards, P.W. (2024), "Seismic Response of Blockout Column Base Plate Connections under Axial Compression and Flexure," *Journal of Structural Engineering*, ASCE, https://doi.org/10.1061/JSENDH.STENG-12349.

Hassan, A., Song, B., Galasso, C., and Kanvinde, A.M. (2022), "Seismic Performance of Exposed Column Base Plate Connections with Ductile Anchor Rods," *Journal of Structural Engineering*, ASCE, Vol. 148, No. 5, pp. 04022028-1–04022028-19, 10.1061/(ASCE)ST.1943-541X.0003298.

Hassan, A., Torres-Rodas, P., Giulietti, L., and Kanvinde, A.M. (2021), "Strength Characterization of Exposed Column Base Plates Subjected to Axial Force and Biaxial Bending," *Engineering Structures*, Elsevier, Vol. 237, pp. 112165-1–112165-13, https://doi.org/10.1016/j.engstruct.2021.112165.

Inamasu, H., Kanvinde, A.M., and Lignos, D., (2020), "Seismic Design of Non-Dissipative Embedded Column Base Connections," *Journal of Constructional Steel Research*, https://doi.org/10.1016/j.jcsr.2020.106417.

Jaspart, J.P. and Vandegans, D. (1998), "Application of the Component Method to Column Bases," *Journal of Constructional Steel Research*, Vol. 48, No. 2–3, pp. 89–106.

Kanvinde, A.M., Grilli, D.A., and Zareian, F. (2012), "Rotational Stiffness of Exposed Column Base Connections—Experiments and Analytical Models," *Journal of Structural Engineering*, ASCE, Vol. 138, No. 5, pp. 549–560.

Kanvinde, A.M., Higgins, P., Cooke, R.J., Perez, J., and Higgins, J. (2014), "Column Base Connections for Hollow Steel Sections: Seismic Performance and Strength Models," *Journal of Structural Engineering*, ASCE, Vol. 141, No. 7, pp. 04014171-1–04014171-13, 10.1061/(ASCE)ST.1943-541X.0001136.

Kanvinde, A.M., Maamouri, M., and Buckholt, J. (2024), *Base Connection Design for Steel Structures*, Design Guide 1, 3rd Ed., AISC, Chicago, Ill.

Lignos, D.G. and Krawinkler, H. (2011), "Deterioration Modeling of Steel Components in Support of Collapse Prediction of Steel Moment Frames under Earthquake Loading," *Journal of Structural Engineering*, ASCE, Vol. 137, No. 11, pp. 1,291–1,302, https://doi.org/10.1061/(ASCE)ST.1943-541X.0000376.

Mattock, A.H. and Gaafar, G.H. (1982), "Strength of Embedded Steel Sections as Brackets," *ACI Journal*, Vol. 79, No. 2, pp. 83–93.

Pertold, J., Xiao, R., and Wald, F. (2000a), "Embedded Steel Column Bases I: Experiments and Numerical Simulation," *Journal of Constructional Steel Research*, Vol. 56, No. 3, pp. 253–270.

Pertold, J., Xiao, R., and Wald, F. (2000b), "Embedded Steel Column Bases II: Design Model Proposal," *Journal of Constructional Steel Research*, Vol. 56, No. 3, pp. 271–286.

Picard, A. and Beaulieu, D. (1985), "Behavior of a Simple Column Base Connection," *Canadian Journal of Civil Engineering*, Vol. 12, pp. 126–136.

Richards, P.W., Barnwell, N.V., Tryon, J.E., and Sadler, A.L. (2018), "Flexural Strength and Stiffness of Block-Out Connections for Steel Columns," *Engineering Structures*, Elsevier, Vol. 173, pp. 404–415.

Sabatka, L., Wald, F., Kabelac, J., Godrich, L., and Navratil, J. (2014), "Component Based Finite Element Model of Structural Connections," 12th International Conference on Steel, Space, and Composite Structures, May 28–30, 2014, Prague, Czech Republic.

Seco, L., Couchaux, M., Hijaj, M., and Costa-Neves, L. (2021), "Column Base Plates under Biaxial Bending Moment and Axial Force," *Engineering Structures*, Elsevier, Vol. 249, pp. 112893-1–112893-29, 10.1016/j.engstruct.2021.112893.

Shahrooz, B.M., Remetter, M.E., and Qin, F. (1993), "Seismic Design and Performance of Composite Coupled Walls," *Journal of Structural Engineering*, ASCE, Vol. 119, No. 11, pp. 3,291–3,309.

Song, B., Galasso, C., and Kanvinde, A.M. (2020), "Reliability Analysis and Design Considerations for Exposed Column Base Plate Connections Subjected to Flexure and Axial Compression," *Journal of Structural Engineering*, ASCE, Vol. 147, No. 2, pp. 04020328-1–04020328-14, 10.1061/(ASCE)ST.1943-541X.0002903.

Song, B., Hassan, A., Kanvinde, A.M., and Galasso, C., (2023), "Probabilistic Seismic Performance Assessment of Steel Moment-Resisting Frames Considering Exposed Column-Base Plate Connections with Ductile Anchor Rods," *Earthquake Engineering and Structural Dynamics*, Wiley, https://doi.org/10.1002/eqe.3949.

Torres-Rodas, P., Zareian, F., and Kanvinde, A.M. (2016), "A Hysteretic Model for Exposed Column Base Connections," *Journal of Structural Engineering*, ASCE, Vol. 142, No. 12, pp. 04016137-1–04016137-14, 10.1061/(ASCE)ST.1943-541X.0001602.

Torres-Rodas, P., Zareian, F., and Kanvinde, A.M. (2017), "Rotational Stiffness of Deeply Embedded Column Base Connections," *Journal of Structural Engineering*, ASCE, Vol. 143, No. 8, pp. 04017064-1–04017064-11.

Torres-Rodas, P., Zareian, F., and Kanvinde, A.M. (2018), "A Hysteretic Model for the Rotational Response of Embedded Column Base Connections," *Soil Dynamics and Earthquake Engineering*, Elsevier, Vol. 115, pp. 55–65.

Trautner, C.A., Hutchinson, T., Grosser, P.R., and Silva, J.F. (2017), "Investigation of Steel Column-Baseplate Connection Details Incorporating Ductile Anchors," *Journal of Structural Engineering*, ASCE, Vol. 143, No. 8, pp. 04017074-1–04017074-10.

Villar-Salinas, S., Kanvinde, A.M., and Lopez-Almansa, F., (2024), "Estimation of Backbone Model Parameters for Simulation of Exposed Column Base Plates," *Journal of Constructional Steel Research*, Elsevier, https://doi.org/10.1016/j.jcsr.2024.109034.

Wald, F., Sokol, Z., and Jaspart, J-P. (2008), "Base Plate in Bending and Anchor Bolts in Tension," *HERON*, Vol. 53, No. 1/2.

Guide for Authors

Scope *Engineering Journal* is dedicated to the improvement and advancement of steel construction. Its pages are open to all who wish to report on new developments or techniques in steel design, research, the design and/or construction of new projects, steel fabrication methods, or new products of significance to the uses of steel in construction. Only original papers should be submitted.

General Go to **aisc.org/ej** for complete submittal instructions.

All papers within the scope outlined above will be reviewed by engineers selected from among AISC, industry, design firms, and universities. The standard review process includes outside review by an average of three reviewers, who are experts in their respective technical area, and volunteers in the program. Published papers become the property of the American Institute of Steel Construction and are protected by appropriate copyrights. No typesetting proofs will be provided to authors.

Manuscripts Manuscripts must be provided in Microsoft Word format. Include a PDF with your submittal so we may verify fonts, equations, and figures. View our complete author guidelines at **aisc.org/ej**.

Archives Search at **aisc.org/ej**. Article downloads are free.

Smarter. Stronger. Steel.

American Institute of Steel Construction
130 E Randolph St, Ste 2000, Chicago, IL 60601
312.670.2400 | aisc.org/ej